

# CHAPTER 1 – Introduction and Background

## 1.1 Trimetallic Nitride Template (TNT) Endohedral Metallofullerenes

### 1.1.1 Introduction of TNT Endohedral Metallofullerenes

The discovery of the first fullerene molecule,<sup>1</sup> C<sub>60</sub>, was rapidly followed by news that metal ions could be encapsulated into the fullerene cages to produce La@C<sub>n</sub> (n = 60, 70, 82), a family of new species that are now called “endohedral metallofullerene”.<sup>2</sup> The “@” symbol is used for naming purposes to indicate atoms to the left are incorporated into the carbon cage on the right.<sup>3</sup> Until now, most of the lanthanide metals and Group I-III metals (Li, Na, K, Cs, Ca, Sr, Ba, Sc, Y, La) have been successfully incorporated into fullerene cages to produce mono-, di-, tri-, or tetra-metallofullerenes.<sup>4</sup> These are all known as “classic” metallofullerenes. However, progress in exploring chemical and physical properties of these endohedral metallofullerenes has been hampered by the difficulty in the production of quantities greater than a few milligrams of materials.

In 1999, Dorn and co-workers reported the preparation of a novel family of endohedral metallofullerenes, Er<sub>x</sub>Sc<sub>3-x</sub>N@C<sub>80</sub> (x = 0-3) which contains the planar tetra-atomic cluster within the fullerene cage.<sup>5</sup> These endohedral metallofullerenes are formed by introducing dinitrogen gas into the Krätschmer-Huffman generator during arc vaporization of composite (metal oxide/graphite) rods. This process, the trimetallic nitride template (TNT) method, produces Sc<sub>3</sub>N@C<sub>80</sub> (Figure 1.1), the most abundant of this family so far, in quantities which exceed that of C<sub>84</sub>, generally the third most abundant fullerene after C<sub>60</sub> and C<sub>70</sub>. Sc<sub>3</sub>N@C<sub>80</sub> was found to have a mass-to-charge ratio (m/z) of 1109 and its <sup>13</sup>C NMR consists of two single lines at chemical shifts of 146.7 ppm and 133.2 ppm with an intensity ratio of 3:1, respectively. The <sup>13</sup>C NMR result suggests the I<sub>h</sub> symmetry of the C<sub>80</sub> cage which contains 60 corannulene-type (intersection of one pentagon and two hexagons) and 20 pyrene-type (intersection of three hexagons) carbon atoms. The <sup>45</sup>Sc NMR results indicate that the Sc<sub>3</sub>N cluster rotates freely with regard to the C<sub>80</sub> cage in solution at room temperature.

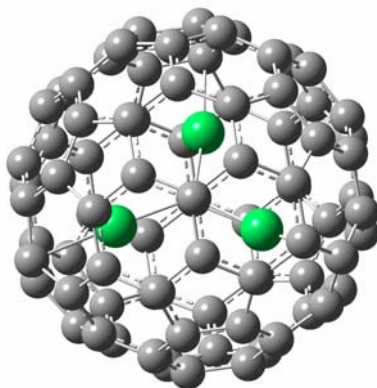


**Figure 1.1** A generic structure of  $\text{Sc}_3\text{N}@C_{80}$

The TNT process with scandium-oxide-doped graphite rods also produces smaller quantities of two other molecules in the TNT family:  $\text{Sc}_3\text{N}@C_{68}$  and  $\text{Sc}_3\text{N}@C_{78}$  (Figure 1.2). As another TNT endohedral metallofullerene,  $\text{Sc}_3\text{N}@C_{68}$  has a  $D_3$  cage symmetry, suggested by the twelve-line  $^{13}\text{C}$  NMR and single-line  $^{45}\text{Sc}$  NMR results.<sup>6</sup>  $\text{Sc}_3\text{N}@C_{78}$  was discovered when a mass of 1085 was observed in the mass spectra of metallofullerene extract. The  $C_{78}$  cage in this species exhibited  $D_{3h}$  symmetry, which was indicated by an eight-line  $^{13}\text{C}$  NMR spectrum and X-ray crystallography.<sup>7,8</sup>

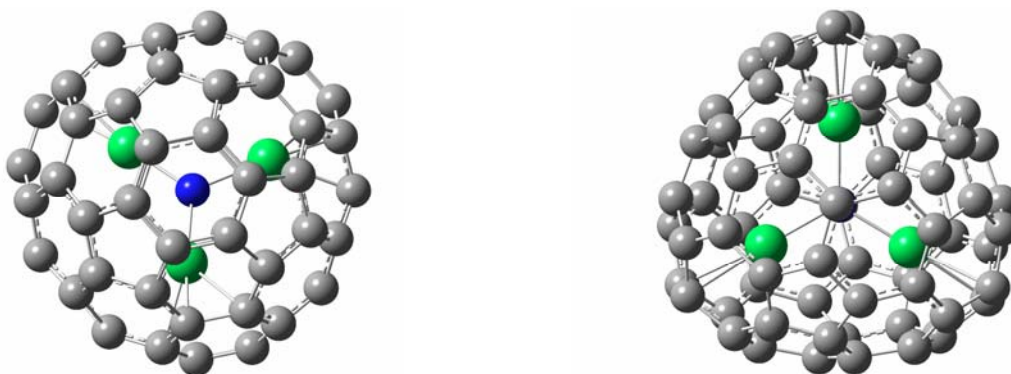


**Figure 1.2** Generic structures of  $\text{Sc}_3\text{N}@C_{78}$  (left) and  $\text{Sc}_3\text{N}@C_{68}$  (right).

## 1.1.2 Structure and cage stability

### 1.1.2.1 Isolated-Pentagon Rule (IPR)

The carbon cages of fullerenes and metallofullerenes have structural isomers with different pentagon and hexagon patterns. The stability of fullerenes can be attributed to a balance between  $\pi$  electronic stability and steric strain. The single most important consequence of steric strain in the fullerenes is the isolated-pentagon rule (IPR), which says that the most stable fullerenes are those in which all the pentagons are isolated. This rule was first proposed by Kroto<sup>9</sup> in 1987 and a more theoretical discussion of the rule was given afterwards by Schmalz et al.<sup>10</sup> Since then, the IPR rule has proved particularly valuable in helping to unravel the experimental structures of higher fullerenes  $C_n$  ( $n > 70$ ).

However, recent discoveries of several IPR-violating cages have provided evidence that not all stable fullerene cages are governed by the isolated pentagon rule. These IPR-violating cages possess different arrangements of fused five-membered rings, which we call the pentalenes pattern. For example, of 6332 possible isomers predicted by the spiral algorithm,  $Sc_3N@C_{68}$  has the rounded  $D_3$ -symmetric cage, which was the most stable isomer and also supported the  $^{13}C$  NMR result.<sup>6</sup>  $Sc_2@C_{66}$  is another case with an IPR-violating cage reported by Shinohara et al.<sup>11</sup> It is believed that charge transfer from the encapsulated clusters to the carbon cage helps stabilize the  $C_{68}$  and  $C_{66}$  cages which otherwise are extremely unstable and can not be isolated as empty-cage species.

### 1.1.2.2 Cage symmetry and charge transfer mode

There are seven isomers ( $D_2$ ,  $D_{5d}$ ,  $C_{2v}$ ,  $C_{2v'}$ ,  $D_3$ ,  $D_{5h}$  and  $I_h$ ) of the empty  $C_{80}$  cage that satisfy the IPR rule. It has been calculated that the most thermodynamically stable isomers of  $C_{80}$  cage are those with  $D_2$  and  $D_{5d}$  symmetries and the  $I_h$  isomer is most unstable by *ca.* 52 kcal/mol.<sup>12</sup> The HOMO-LUMO gaps indicated the  $D_2$  symmetry isomer, eventually verified from successful isolation and analysis of the  $^{13}C$  NMR spectrum, was slightly less reactive and showed greater air stability than the  $D_{5d}$  isomer.<sup>13-14</sup> Furthermore, *ab initio* and semi-empirical calculations have shown that the  $I_h$  isomer can distort to form the more stable  $D_2$  isomer.<sup>15</sup>

However, theoretical calculation of  $\text{La}_2@\text{C}_{80}$  by Kobayashi and co-workers<sup>15</sup> shows that encapsulation of two La atoms inside the  $I_h$  cage is the most favorable because the  $I_h$  cage has only two electrons in its fourfold degenerate HOMO orbitals and can accommodate six more electrons from the cluster encapsulated to form a closed-shell electronic state of  $[(\text{La}^{3+})_2]@\text{C}_{80}]^{6-}$ . In the case of  $\text{Sc}_3\text{N}@\text{C}_{80}$ , it is plausible to assume that the metal-nitride cluster  $[\text{Sc}_3\text{N}]$  will formally donate six electrons to the  $\text{C}_{80}$  cage to stabilize the entire molecule and the resulting electronic state can be described as  $[\text{Sc}_3\text{N}]^{+6}@\text{C}_{80}]^{-6}$ .

Recent density functional theory (DFT) calculations of  $\text{Sc}_3\text{N}@\text{C}_{80}$  have shown that the formal electronic state  $[\text{Sc}_3\text{N}]^{+6}@\text{C}_{80}]^{-6}$  is not an exactly accurate charge transfer description within the molecule.<sup>16-17</sup> Krause et al.<sup>16</sup> reported the charge (q) on the central nitrogen was -0.9 ( $s^{1.7}p^{4.2}$  and each scandium atom donated nearly one s electron to the carbon cage ( $q = +1.2$ ,  $s^{0.2}p^{0.2}d^{1.4}$ ). The X-ray absorption spectroscopy (XAS) results of  $\text{Sc}_3\text{N}@\text{C}_{80}$  showed the scandium atom has a 3d electron count of 0.6 ( $3d^{0.6}$ ) and yields an effective Sc valence count of 2.4. Considering an additional 0.3 electrons transferred from each scandium atom to nitrogen, the total electrons that are transferred to the  $\text{C}_{80}$  cage will be 6.3 to stabilize the  $I_h$  symmetry.<sup>17</sup>

A less abundant isomer of  $\text{Sc}_3\text{N}@\text{C}_{80}$  has recently been reported. The  $^{13}\text{C}$  NMR measurement and single-crystal X-ray diffraction study confirm the  $D_{5h}$  symmetry of  $\text{C}_{80}$  cage (see Chapter 4), which is consistent with theoretical calculation that  $D_{5h}$  cage is the second most stable isomer for  $\text{C}_{80}$ .<sup>18</sup> Interestingly, Dunsch and coworkers reported the isolation of a third isomer of  $\text{Dy}_3\text{N}@\text{C}_{80}$ . The FT-IR and UV-Vis-NIR spectra suggest it might have the  $D_{5d}$  cage symmetry.<sup>19</sup> In similar fashion to  $\text{Sc}_3\text{N}@\text{C}_{80}$ , the  $D_{3h}$  cage of  $\text{Sc}_3\text{N}@\text{C}_{78}$  and the  $D_3$  cage of  $\text{Sc}_3\text{N}@\text{C}_{68}$  are formally stabilized by accommodating six electrons from the encapsulated clusters.<sup>6-8</sup>

### 1.1.2.3 Internal motion of the cluster

In 1997, Akasaka et al.<sup>13</sup> reported that the  $^{139}\text{La}$  spectrum of  $^{13}\text{C}$ -enriched  $\text{La}_2@\text{C}_{80}$  at room temperature exhibited a single line and the  $^{13}\text{C}$  NMR spectrum showed a single broad resonance. These NMR results suggested the two  $\text{La}^{3+}$  ions inside the cage are equivalent at room temperature due to their rapid circular motion inside the negatively charged cage. The theoretical calculations revealed that the rotational barrier of two La atoms inside the  $\text{C}_{80}$  cage is very small (about 5 kcal/mol), which suggests that the motion of two La atoms might stop upon a temperature decrease. The  $^{13}\text{C}$  NMR measurement at 258K showed a thirteen-line  $^{13}\text{C}$  NMR and revealed that the La atoms became localized with the cage, resulting in the  $\text{D}_{2h}$  symmetry of  $\text{La}_2@\text{C}_{80}$ .

Interestingly, the room temperature  $^{13}\text{C}$  NMR spectrum (time-averaged) of the  $\text{Sc}_3\text{N}@\text{C}_{80}$   $\text{I}_h$  isomer showed two peaks in a 3:1 ratio and the  $^{45}\text{Sc}$  NMR at 298K exhibited a single line, which indicated the  $[\text{Sc}_3\text{N}]^{6+}$  cluster is rapidly rotating inside the  $\text{C}_{80}$  cage to preserve the overall  $\text{I}_h$  symmetry of the cage on the NMR timescale.<sup>5</sup> Due to the small rotational barrier of the  $\text{Sc}_3\text{N}$  cluster inside the cage (1.7 kcal/mol, see Chapter 5), it is plausible to assume that the motion of  $[\text{Sc}_3\text{N}]^{6+}$  can be stopped at the most stable positions upon a decrease in temperature.

The eight-line  $^{13}\text{C}$  NMR spectrum<sup>7</sup> and one single-line  $^{45}\text{Sc}$  NMR spectrum (see Chapter 5) of  $\text{Sc}_3\text{N}@\text{C}_{78}$  at room temperature suggested the  $[\text{Sc}_3\text{N}]^{6+}$  cluster is presumably dynamic along the belt of the cage. However, recent DFT calculations predicted that the molecule has the lowest energy when the Sc atoms of the cluster are static and located over the three pyracylene patches ([6,6] ring-junctions).<sup>8</sup> Movement of scandium atoms to other sites within the molecule will generate extremely high energies.

Due to the smaller size of the  $\text{C}_{68}$  cage, the internal cluster is presumed static in  $\text{Sc}_3\text{N}@\text{C}_{68}$ . Experimentally, the twelve-line  $^{13}\text{C}$  NMR and single-line  $^{45}\text{Sc}$  NMR spectra at room temperature were observed. However, NMR studies at lower temperature are needed to verify the hypothesis.

## 1.2 Synthesis, Isolation and Purification of TNT Endohedral Metallofullerenes.

### 1.2.1 Synthesis and formation mechanism

There are only two methods that are currently employed for synthesizing classic Endohedral metallofullerenes: The Krätschmer-Huffman electric-arc method and the laser furnace method. In the Krätschmer-Huffman electric-arc method, a hollowed graphite rod was packed with a metal-oxide/graphite powder mixture and after heat treatment (1000 °C) under a nitrogen gas flow, the composite rod was arc-vaporized by using an alternating or direct current (AC or DC) under a dynamic helium atmosphere at over 3000°C (Figure 1.3). Once a rod is consumed, the resulting carbon soot is collected from the generator.

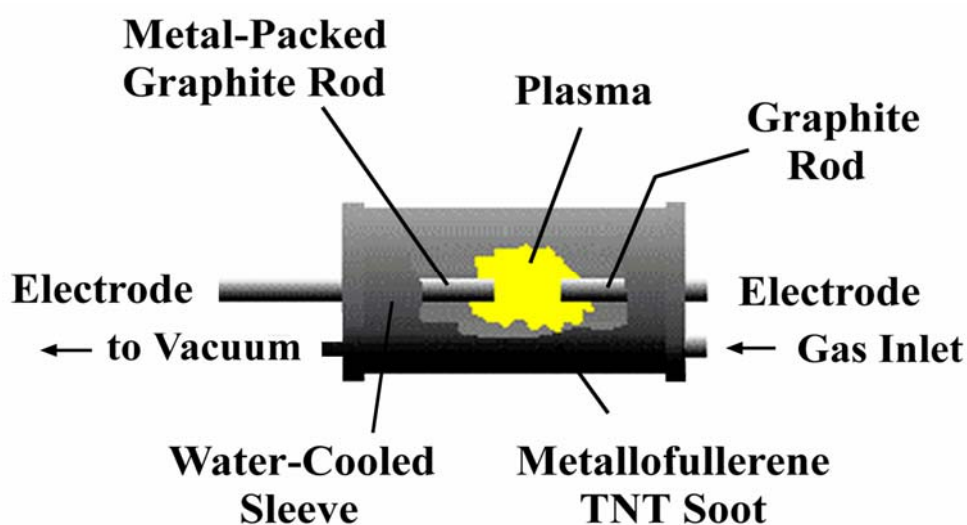


**Figure 1.3** Drawing of a typical Kratschmer-Huffman generator.

The laser furnace method, which is less commonly used, involves a high-temperature laser vaporization of the composite rods. First, a rod is placed in the laser furnace and heated to 1200°C, then a ND:YAG laser doubled into the green (532 nm, 300 mJ per pulse at 10 Hz) is focused onto the target rod. During the burning process, the rod is rotating to ensure a fresh surface (Figure 1.4).

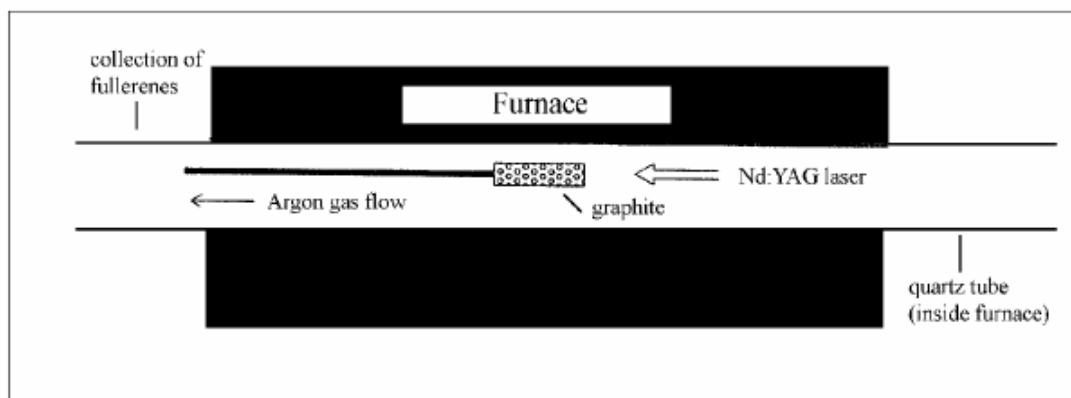


**Figure 1.4** Schematic diagram of laser furnace.

So far, the trimetallic nitride endohedral metallofullerenes have only been synthesized by the Kratschmer-Huffman method. Instead of a helium atmosphere, a dynamic environment of both nitrogen and helium gases is needed during the arc vaporization process since nitrogen gas is the nitrogen source. However the nitrogen gas can also be replaced by ammonia gas.<sup>20</sup>

Although the mechanism of fullerene formation via arc vaporization of graphite rods is believed to involve a stepwise growth process, the formation mechanism of traditional and trimetallic nitride endohedral metallofullerenes is unknown. One possibility is that at sometime during the growth process, the metal atoms/cluster are incorporated to a cationic cluster(s) or hoop, which subsequently grow around them to form the carbon cage.<sup>21</sup> Another possible mechanism is that during the cooling process, the cages open to insert the metal atoms or cluster. The selective formation of an  $A_3N$  cluster in the trimetallic nitride template endohedral metallofullerenes yields a stable carbon cage. Recently, Rubin et al. investigated a series of ring opening reactions with fullerene cages in effort to insert metal atoms and produce endohedral metallofullerenes.<sup>22</sup>

### 1.2.2 Extraction of the soot

The raw product obtained by the evaporation of graphite is soot and slag. Besides soluble fullerenes, the soot and slag contain other kinds of closed carbon structures, such as giant fullerenes and nanotubes. The fullerenes can be isolated from the soot either by sublimation or

by extraction. The most commonly used method is Soxhlet extraction utilizing a porous cellulose thimble with organic solvents. In general, toluene is used as solvent since it provides a sufficient solubility and is less toxic than benzene or carbon disulfide. It has been shown that longer extraction times lead to higher yields of fullerenes.

### 1.2.3 Purification of TNT endohedral metallofullerenes

High-Pressure Liquid Chromatography (HPLC) is the standard technique for separating metallofullerenes, empty-cage fullerenes and structural isomers of both species. Generally a two- or three-phase sequence of HPLC columns with different absorption mechanisms needs to be utilized due to the presence of multiple isomers of both the fullerenes and metallofullerenes. In the purification process of TNT endohedral metallofullerenes, the commonly used columns are 5-PBB (5  $\mu\text{m}$ , pentabromobenzyl) column, Buckyprep (3-(1-pyrenyl)propylsilyl) column, Trident-Tri-DNP (Buckyclutcher) column and 5PYE (5 $\mu\text{m}$ , 2-(1-pyrenyl)ethylsilyl ) column (Figure 1.5). Carbon disulfide and toluene are commonly used as the eluent.

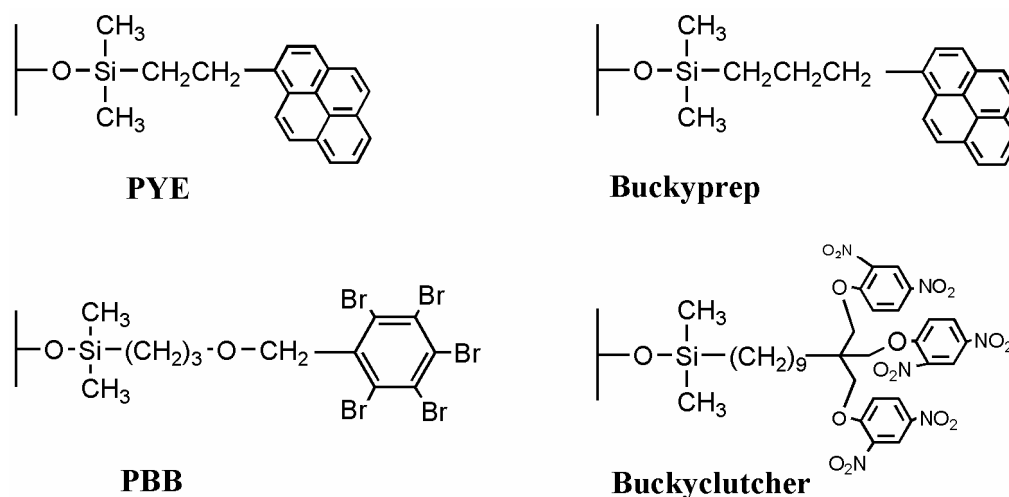


**Figure 1.5** Generic stationary phase structures of four commonly used HPLC columns.

Recently, Dorn et al.<sup>23</sup> reported a new purification protocol in which pure TNT endohedral metallofullerenes can be obtained from crude soots in a single, facile step. This purification protocol is based on the kinetic stability of the trimetallic nitride endohedral metallofullerenes relative to empty-cage fullerenes and classical endohedral metallofullerenes, such as  $A_x@C_{2y}$

(A = lanthanide atom, x = 1-3, y = 30-50). A cyclopentadiene-functionalized styrene-divinylbenzene resin was synthesized from the chloromethylated (Merrifield) resin and packed in a glass column in toluene. Then the soot extract was applied to this column and toluene was flushed through by gravity feed, the more reactive empty-cage fullerenes and classic endohedral metallofullerenes were trapped by the functionalized Merrifield resin and trimetallic nitride endohedral metallofullerenes could be obtained from the resultant solution. Furthermore, it was demonstrated that the bound empty-cage fullerenes and classical endohedral metallofullerenes can be recovered by displacement with maleic anhydride. This new purification protocol avoids the extensive and time-consuming chromatographic procedures and makes the yields of trimetallic nitride endohedral metallofullerenes higher by about 2-fold.

#### 1.2.4 Characterization methods

Due to limited sample quantities, most characterization studies of trimetallic nitride endohedral metallofullerenes involve X-ray diffraction, mass spectrometry, electron paramagnetic resonance, FT-IR (Fourier transform infrared) spectrometry, UV-Vis-NIR (Ultraviolet-visible-near infrared) spectroscopy and x-ray photoelectron spectroscopy. Among these methods, the X-ray diffraction technique has been employed to determine the cage structures, the location of the encapsulated atoms and the nature of the metal-cage interactions in several trimetallic nitride endohedral metallofullerenes. Since trimetallic nitride endohedral metallofullerenes themselves do not appear to form X-ray diffraction quality crystals, cocrystallization with  $M^{II}(\text{OEP})$  ( $M = \text{Co}, \text{Ni}$ ) was utilized. For example, a single-crystal X-ray diffraction study of  $(\text{ErSc}_2\text{N}@C_{80}) \cdot \text{Co}^{II}(\text{OEP}) \cdot 0.3(\text{CHCl}_3) \cdot 1.5\text{benzene}$  confirmed a planar  $\text{ErSc}_2\text{N}$  cluster incorporated into the icosahedral  $C_{80}$  cage. As expected, the measured Sc-N distance (0.1968 nm) is shorter than the Er-N distance (0.2089 nm) due to the larger size of the erbium atom. The crystal data also shows the metal ions make close contact with individual carbon atoms of the cage with the shortest Sc-C distances of 0.203-0.212 nm and shortest Er-C distances of 0.220-0.222 nm.

Significant progress has also been achieved by high field NMR studies of  $\text{Sc}_3\text{N}@C_{80}$ ,

$\text{Sc}_3\text{N}@C_{78}$  and  $\text{Sc}_3\text{N}@C_{68}$ . The  $^{13}\text{C}$  NMR spectrum, together with  $^{45}\text{Sc}$  NMR results, revealed important information about cage symmetry and internal motion of the  $\text{Sc}_3\text{N}$  cluster. For example, the  $D_{3h}$  symmetry of the  $C_{78}$  cage in  $\text{Sc}_3\text{N}@C_{78}$  suggested by the eight-line  $^{13}\text{C}$  NMR and single-line  $^{45}\text{Sc}$  NMR spectra at room temperature is in agreement with x-ray diffraction data.

## 1.3 Functionalization of Trimetallic nitride endohedral metallofullerenes

### 1.3.1 Reactivity of $\text{A}_3\text{N}@C_{80}$

The reactivity of  $C_{60}$  is governed mainly by a combination of factors including steric effects, electron withdrawal by the cage, a drive to increase aromaticity of the cage, and electron-deficient polyalkene structure with rather delocalized double bonds.<sup>24,25</sup> The  $C_{60}$  molecule can react with radicals, carbenes and nucleophiles and participate as the electron-deficient dienophile in a large variety of cycloadditions to form monoadducts or multiadducts.<sup>26</sup> The introduction of halogen,<sup>27</sup> hydrogen<sup>28</sup> and organometallic compounds<sup>29</sup> onto fullerene cages has also been reported. It is worth noting that once the fullerene carbon atoms become functionalized, the hybridization is changed from a strained trigonal-planar to a less strained tetrahedral state.

Endohedral metallofullerenes are less reactive than empty-cage  $C_{60}$  because the encapsulation of metal species helps stabilize the carbon cage. The first exohedral derivative of an endohedral metallofullerene,  $\text{La}@C_{82}(\text{Mes}_2\text{Si})_2$  was reported by Akasaka et al. in 1995.<sup>30</sup> Since then, organic functionalization of endohedral metallofullerenes have attracted wide interest over the past decade due to the extraordinary chemical and physical properties of endohedral metallofullerenes and the potential applications of their derivatives. However, the difficulty in preparing and isolating macroscopic quantities of endohedral metallofullerenes has limited the organic functionalization of the carbon cages.

The derivatization of trimetallic nitride endohedral metallofullerenes is of great importance not only because  $\text{Sc}_3\text{N}@C_{80}$  is the third most abundant fullerene, following  $C_{60}$  and  $C_{70}$ , but their functionalization is crucial in the development of new materials with potential

applications in material and medical science which will be discussed below. Compared to empty-cage fullerenes, such as  $C_{60}$ , the reactivity of trimetallic nitride endohedral metallofullerenes will be altered due to the encapsulation of metal atoms and charge transfer from the cluster to the carbon cage. Furthermore, the reaction sites on the cage might also be changed. For example, although both  $C_{60}$  and the  $C_{80}$  cage in  $Sc_3N@C_{80}$  exhibit icosahedral symmetry ( $I_h$ ),  $C_{60}$  cage is composed of a single pyracycene-type carbon and undoubtedly the reaction site will be at so-called [6,6] ring junctures, whereas the  $Sc_3N@C_{80}$  consists of two types of carbon atoms: a pyrene-type carbon and a corannulene-type carbon and other reactive sites than pyracycene-type carbons must be present.

### 1.3.1.1 Diels-Alder Cycloaddition

In 2001, Dorn and coworkers<sup>31</sup> reported the first derivative of trimetallic nitride endohedral metallofullerenes, by reacting  $Sc_3N@C_{80}$  with a Diels-Alder cycloaddition precursor. The precursor 6,7-dimethoxyisochroman-3-one was synthesized and  $^{13}C$ -labeled formaldehyde was used to label the precursor at the 1-position. A 1,2,4-trichlorobenzene solution containing  $Sc_3N@C_{80}$  was refluxed for 24 hours with an excess of the precursor to achieve the novel monoadduct (Figure 1.6). The matrix assisted laser desorption ionization time-of-flight mass spectrum (MALDI-TOF MS) showed peaks at  $m/z$  1274 and 1109, which correspond to the  $^{13}C$  labeled monoadduct and the parent  $Sc_3N@C_{80}$ , respectively. Adducts of higher mass were not observed within the spectrum.  $^{13}C$  NMR spectrum of the derivative displays a single narrow peak at 41.25 ppm for the equivalent methylene carbons, whereas the  $^1H$  NMR spectrum shows two non-equivalent geminal hydrogens attached to the methylene carbon. These NMR results, together with 2D COSY (Correlation Spectroscopy) and HMQC (Heteronuclear Multiple Quantum Coherence) suggested that the reaction occurs at a [5,6] ring juncture, which was confirmed by the single-crystal X-ray diffraction study.

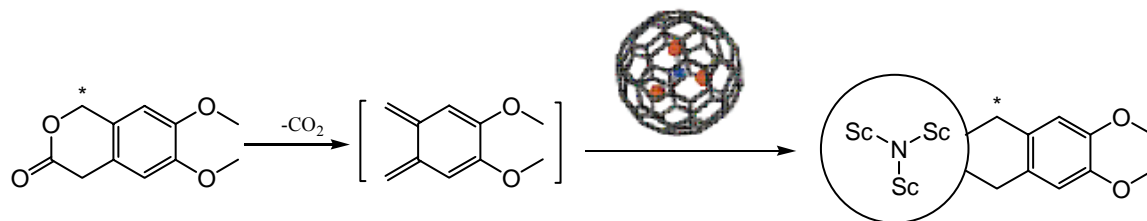


**Figure 1.6** Diels-Alder cycloaddition of  $\text{Sc}_3\text{N}@C_{80}$

More recently, Stevenson et al.<sup>32</sup> reported a similar [4+2] Diels-Alder reaction of  $\text{Gd}_3\text{N}@C_{80}$  with o-quinodimethane intermediate (Figure 1.7). Different from the reaction of  $\text{Sc}_3\text{N}@C_{80}$  shown above, both the monoadduct and bisadduct of  $\text{Gd}_3\text{N}@C_{80}$  were observed in the MALDI-TOF mass spectrum, suggesting  $\text{Gd}_3\text{N}@C_{80}$  might be more reactive toward the o-quinodimethane intermediate than  $\text{Sc}_3\text{N}@C_{80}$ . The locations of the two isochromanone bonding attachment sites to the cage have not yet been determined due to the limited amount of the bisadduct available.

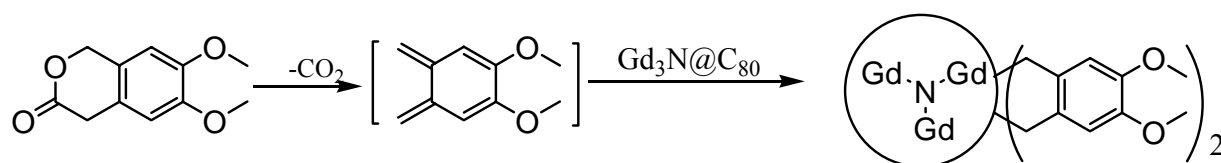


**Figure 1.7** Diels-Alder cycloaddition of  $\text{Gd}_3\text{N}@C_{80}$

### 1.3.1.2 Hydroxylation of $\text{Sc}_3\text{N}@C_{80}$

Water-soluble endohedral metallofullerols have been extensively studied over the last decade for the potential application of endohedral metallofullerene derivatives in biological systems. Generally, the endohedral metallofullerols can be synthesized from procedures that are similar to those used for  $C_{60}$  hydroxylations. In 2000, Kato et al.<sup>33</sup> reported the synthesis of a multi-hydroxylated fullerene,  $\text{Gd}@C_{82}(\text{OH})_n$  ( $n = 30-40$ ), using TBAOH (tetrabutylammonium hydroxide) as a transfer agent. Another example,  $\text{Pr}@C_{82}(\text{OH})_m(\text{O})_n$  ( $m \approx 10$  and  $n \approx 10$ ) was synthesized by Sun and coworkers, using  $\text{NO}_2$  under an oxygen atmosphere.<sup>34</sup>

In 2001, Iezzi et al.<sup>35</sup> reported the first water-soluble TNT endohedral metallofullerene

derivative,  $\text{Sc}_3\text{N}@C_{80}(\text{O})_{\sim 10}(\text{OH})_{\sim 10}$ . As shown in Figure 1.8, water-soluble  $\text{Sc}_3\text{N}@C_{80}$  metallofullerols has been made in a two-step reaction. Firstly, a toluene solution of  $\text{Sc}_3\text{N}@C_{80}$  was refluxed with sodium metal under an argon environment to form a black polyanionic species that precipitated from solution, then the mixture was exposed to water and air and precipitates was oxidized to produce a golden-colored aqueous solution of  $\text{Sc}_3\text{N}@C_{80}(\text{O})_{\sim 10}(\text{OH})_{\sim 10}$ . Although the mechanism of hydroxyl group formation is not clear yet, the addition of oxygen has been found to be critical to the formation of metallofullerols.

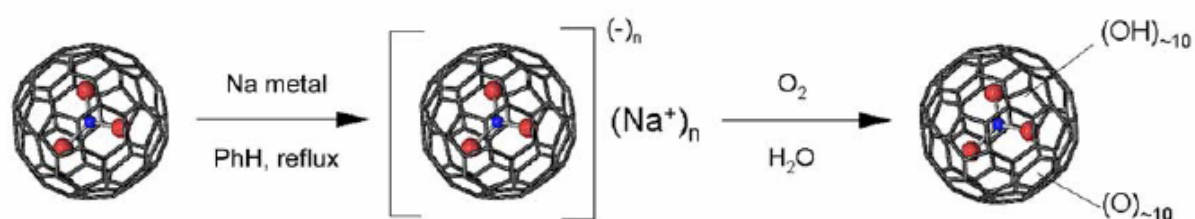


**Figure 1.8** Hydroxylation of  $\text{Sc}_3\text{N}@C_{80}$ .

The synthesized  $\text{Sc}_3\text{N}@C_{80}(\text{OH})_{\sim 10}(\text{O})_{\sim 10}$  had been characterized by FT-IR spectroscopy, LD-TOF (laser-desorption time-of-flight) mass spectrometry and XPS (X-ray photoelectron spectroscopy) spectroscopy. The FT-IR spectrum confirmed the attachment of hydroxyl groups to the carbon cage. The C1s region in the XPS spectrum demonstrates the different types of functionalized carbon atoms on the water-soluble cage, which suggests a metallofullerol with the formula of  $\text{Sc}_3\text{N}@C_{80}(\text{O})_{\sim 10}(\text{OH})_{\sim 10}$ . The LD-TOF mass spectrum shows a single peak at  $m/z$  1109, corresponding to the parent endohedral metallofullerene  $\text{Sc}_3\text{N}@C_{80}$ . There is no peak corresponding to water-soluble adducts because metallofullerols decompose to the unsubstituted metallofullerenes upon heating or laser desorption process.

### 1.3.1.3 1,3-dipolar cycloaddition

In 1993, Prato et al.<sup>36</sup> discovered the 1,3-dipolar cycloaddition of azomethine ylides to fullerenes, which was named the Prato reaction. Since then, the Prato reaction has been one of the most useful methods among the wide variety of functionalizations of fullerenes, due to

the formation of various pyrrolidino fullerene derivatives from aldehydes and N-substituted glycines.

Recently, Dorn et al.<sup>37</sup> successfully synthesized and characterized the first trimetallic nitride endohedral pyrrolidinometallofullerenes,  $A_3N@C_{80}[(CH_2)_2NCH_3]$  ( $A = Sc, Er$ ) through 1,3-dipolar cycloaddition of azomethine ylides to the  $C_{80}$  cage. The Prato reaction on trimetallic nitride endohedral metallofullerenes is of great importance because it allows access to various derivatives which have potential applications for medical and material science.

As shown in Figure 1.9,  $A_3N@C_{80}$  ( $A = Sc, Er$ ) was allowed to react with 12 equivalents of  $^{13}C$  labeled formaldehyde and 4 equivalents of N-methylglycine in o-dichlorobenzene at  $110^\circ C$  for 10 hours.<sup>37</sup> The endohedral monoadducts are dominant in the products in yields of 30-40%. The NMR analysis of the monoadduct revealed that the reaction site is the 5,6-ring juncture on the  $I_h$  cage of  $C_{80}$ , which is consistent with the Diels-Alder reaction of  $Sc_3N@C_{80}$  discussed above. At the same time, Cardona and co-workers<sup>38</sup> also reported 1,3-dipolar cycloaddition of the N-ethyl azomethine to  $Sc_3N@C_{80}$  and  $Y_3N@C_{80}$ .

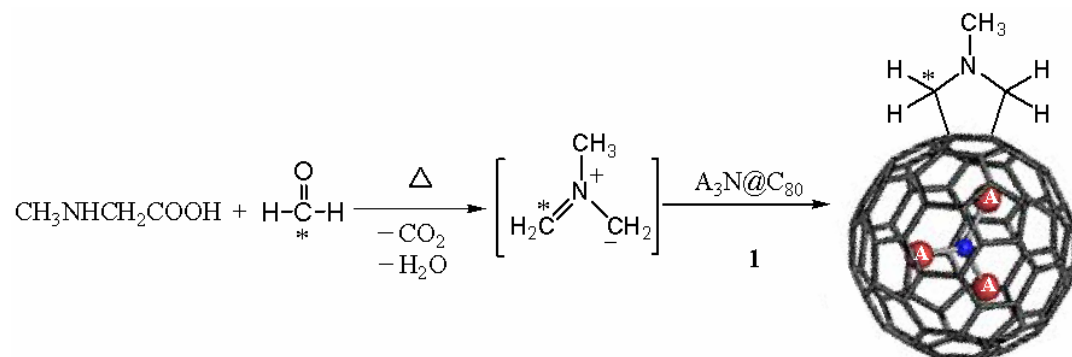


**Figure 1.9** 1,3-dipolar cycloaddition of  $A_3N@C_{80}$  ( $A = Sc, Er$ ).

#### 1.3.1.4 Bingel-Hirsch Reaction

The Bingel-Hirsch reaction, which is the reaction of  $C_{60}$  with halogenated active methylene compounds in the presence of 1,8-diazabicyclo[5,4,0]undec-7-ene (DBU), is one of the most widely applied reactions in fullerene chemistry due to the formation of various cyclopropanated derivatives of fullerenes.<sup>39</sup> In 2005, Cardona et al.<sup>40</sup> explored the Bingel-Hirsch reaction on  $Sc_3N@C_{80}$  and  $Y_3N@C_{80}$  and demonstrated the remarkable

difference in reactivity between these two trimetallic nitride endohedral metallofullerenes. As presented in Figure 1.10, the diethyl malonate monoadduct of  $Y_3N@C_{80}$  was produced via cyclopropanation with excess diethyl bromomalonate and DBU in a reasonable yield after 10 minutes of reaction at room temperature. However, the reaction failed completely when conducted with  $Sc_3N@C_{80}$ .

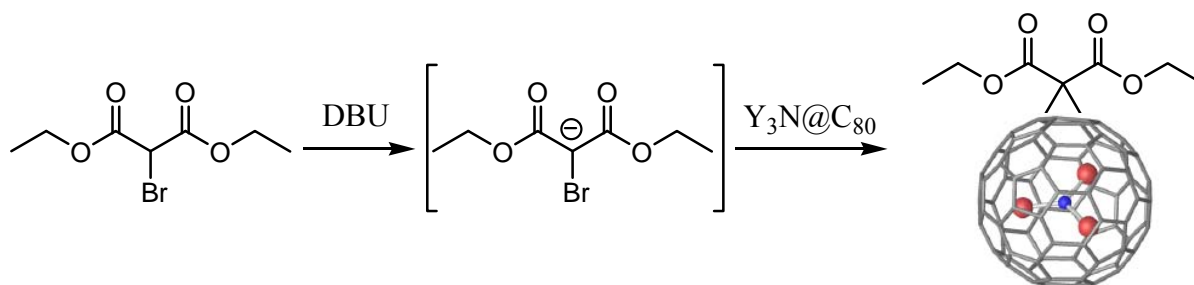


**Figure 1.10** Bingel-Hirsch Reaction of  $Y_3N@C_{80}$ .

Interestingly, the NMR studies showed both ethyl groups are equivalent, indicating the cyclopropanation occurred on the 6,6-double bond of the  $I_h$  cage of  $Y_3N@C_{80}$ . The reaction site of  $Y_3N@C_{80}$  in the Bingel-Hirsch reaction is different from that in the Diels-Alder addition to  $Sc_3N@C_{80}$  which has been shown to be a 5,6-double bond. It was proposed that the  $C_{80}$  cage of  $Y_3N@C_{80}$  may be distorted due to the different clusters.

### 1.3.2 Reactivity of $A_3N@C_{78}$

Most functionalization reactions of trimetallic nitride endohedral metallofullerenes focus on the  $A_3N@C_{80}$  species due to the relative higher yields of  $A_3N@C_{80}$  than  $A_3N@C_{78}$  and  $A_3N@C_{68}$ . For example,  $Sc_3N@C_{78}$  is eight times less abundant than  $Sc_3N@C_{80}$  in fullerene soot and  $Sc_3N@C_{68}$  is even less than  $Sc_3N@C_{78}$ .

The  $C_{78}$  cage in  $A_3N@C_{78}$  has a  $D_{3h}$  symmetry and is composed of eight different carbon atoms, which was confirmed by both the  $^{13}\text{C}$  NMR and single-crystal X-ray diffraction studies. It contains three pyracylene-type units (two hexagon with one pentagons), which was proved to be reactive units on  $C_{60}$  and lead to a functionalization of the cage across the 6,6-bond

junctures. However, the reaction site remains unknown due to the lack of experimental data.

Erick Iezzi<sup>41</sup> first explored the reactivity of  $\text{Sc}_3\text{N}@C_{78}$  by reacting  $^{13}\text{C}$  labeled 6,7-dimethoxyisochroman-3-one with  $\text{Sc}_3\text{N}@C_{78}$  in 1,2,4-trichlorobenzene solution at  $214^\circ\text{C}$  (Figure 1.11). The HPLC analysis and MALDI-TOF mass spectrum revealed the formation of a monoadduct with a single structural isomer, di- and tri-adducts with several structural isomers. However, these isomers have not been characterized due to the difficulty in isolation and purification.

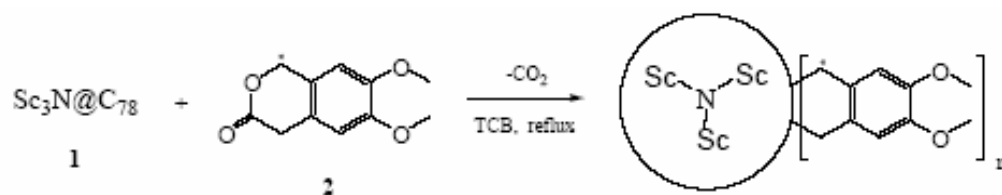


**Figure 1.11** Diels-Alder reaction of  $\text{Sc}_3\text{N}@C_{78}$ .

## 1.4 Mechanochemical Reactions of Fullerenes

### 1.4.1 Background of mechanochemistry

The term mechanochemistry was proposed by Ostwald as early as 1919 as an energy source for chemical reactions.<sup>42</sup> It involves the transformation of mechanical energy into the driving force for the chemical reactions of solid reagents. Mechanochemistry is generally done without any solvent. The external dynamic force generated from the mechanical agitation can induce the solid to its vibrationally and electronically excited structures, thus destabilizing the electronic structure of the bonding and making the solid prone to chemical reaction. “The activation of the local reaction sites by the mechanical energy caused by the stress, friction, shear deformation etc, together with the high concentration and closest contact of the reacting species due to the lack of solvation, would be particularly advantageous for the chemical reaction in the solid state.”<sup>43</sup>

Mechanochemistry was mainly applied to processes which are related to inorganic materials, such as alloys, ceramics, ferrites, semiconductors and superconductors, ferroelectrics, mineral fertilizers, catalysts, ceramic construction materials, etc. Fewer examples of

mechanochemical reactions by ball milling involving organic compounds have been reported.<sup>44,45,46,47,48,49</sup> Different types of mechanochemical devices used to provide mechanical activation energy differ in capacity and efficiency. Generally they can be classified into two categories: grind devices and milling devices. Shaker mills such as SPEX<sup>TM</sup> are most commonly used in laboratory investigations. A shaker mill contains a vial, which consists of the sample and grinding balls and is secured in the clamp and swung energetically back and forth several thousand cycles per minute. SPEX<sup>TM</sup> mills are manufactured by SPEX CertPrep, Metuchen, NJ and can process about a 10-20g sample at a time.

Most of the mechanochemical reactions described below were done with the so-called “High-Speed Vibration Mill”, which has almost the same working mechanism as the SPEX mills. It consists of a capsule and a milling ball, which are made of stainless steel (Fe-Cr-Ni with a composition of 74:18:8 wt %). The capsule containing the sample and milling ball was fixed in a Wig-L-Bug vibrating machine so that the capsule was shaken along its axis horizontally with a slight fluctuation at a speed of 3500 cycles per minute (Figure 1.12).<sup>50</sup> Limited by the small size of the capsule, the high-speed vibration mill can only handle a small amount of sample, no more than 250 mg

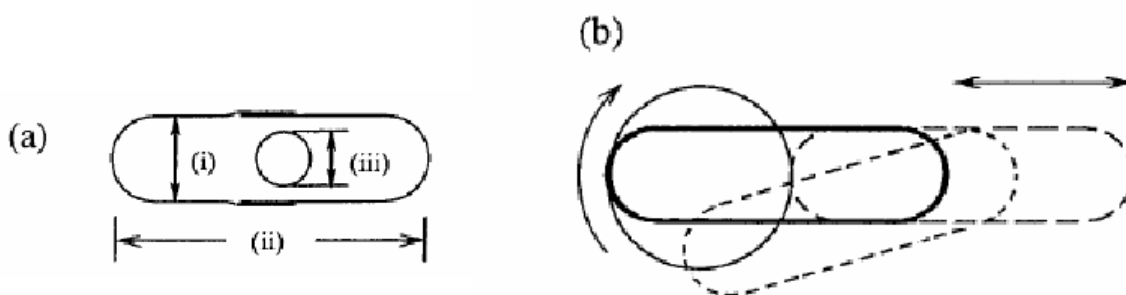


**Figure 1.12** (a) A mixing capsule with a milling ball: (i) inner diameter, 9.0 mm; (ii) inner length, 22 mm; (iii) diameter, 3 mm; (b) Schematic representation of the movement of the capsule: one end moves around a circle while the other end moves horizontally.

## 1.4.2 Functionalization of Fullerenes under the HSVM condition

The solubility of fullerenes in common organic solvents is so low that a large amount of solvent is used in their solution reactions. “The reactions of fullerenes in the absence of any solvent have advantages over their solution reactions from the viewpoint of the solubility problem of fullerenes and environmentally benign concern by eliminating the usage of harmful organic solvent.”<sup>51</sup> Therefore the use of solvent-free reactions on fullerenes to synthesize fullerene derivatives is attractive and appealing. Since 1997, much work on various solvent-free reactions of fullerenes has been done.<sup>51</sup>

The simplest method of methanochemistry is using mortar and pestle while ball milling is suitable when a pro-longed reaction time is required. Various organic reactions have been shown to take place in the solid state when a mortar and pestle is used in the absence of solvents.<sup>52-53</sup> In these examples, essentially the same reactions are reported to occur regardless of the presence or absence of solvents. For most of the reactions shown below, the so-called “High-Speed Vibration Milling” (HSVM) technique is utilized. The stainless-steel capsule is vigorously shaken at a frequency of 3500 cycles per minute. The effective maximum local pressure in the stainless-steel capsule is no less than 15000 bars during the high-speed milling process.<sup>54</sup> It has been observed that some solid-state reactions of fullerenes are totally different from those in the liquid phase while some novel solid-state reactions of fullerenes occur only under HSVM conditions.

### 1.4.2.1 Nucleophilic Addition of Organozinc Reagents to C<sub>60</sub>

The nucleophilic addition of amines, organolithiums and Grignard reagents to C<sub>60</sub> is one of the most widely used reactions to functionalize C<sub>60</sub>. These reactions were always done in organic solvents such as benzene and toluene.<sup>39</sup> The HSVM technique was first applied to fullerene chemistry through the Reformatsky-type reaction of C<sub>60</sub>.<sup>55</sup> The addition of organozinc reagents to C<sub>60</sub>, which had not ever been attempted in solution, was investigated under solvent-free HSVM conditions. A mixture of C<sub>60</sub>, zinc powder and ethyl bromoacetate with a molar ratio of 1:20:5, along with a stainless-steel milling ball, was put into a

stainless-steel capsule. The capsule was shaken at the speed of 3500 cycles per minute by using a high-speed vibration mill. Then the reaction mixture was acidified and separated to give mainly the expected product **1** in a yield of 17.2% and some minor by-products **2**, **3**, **4** along with 72.5% recovered C<sub>60</sub> (Figure 1.13). Longer reaction times increased the yield of compound **3** but decreased that of the main product **1**.

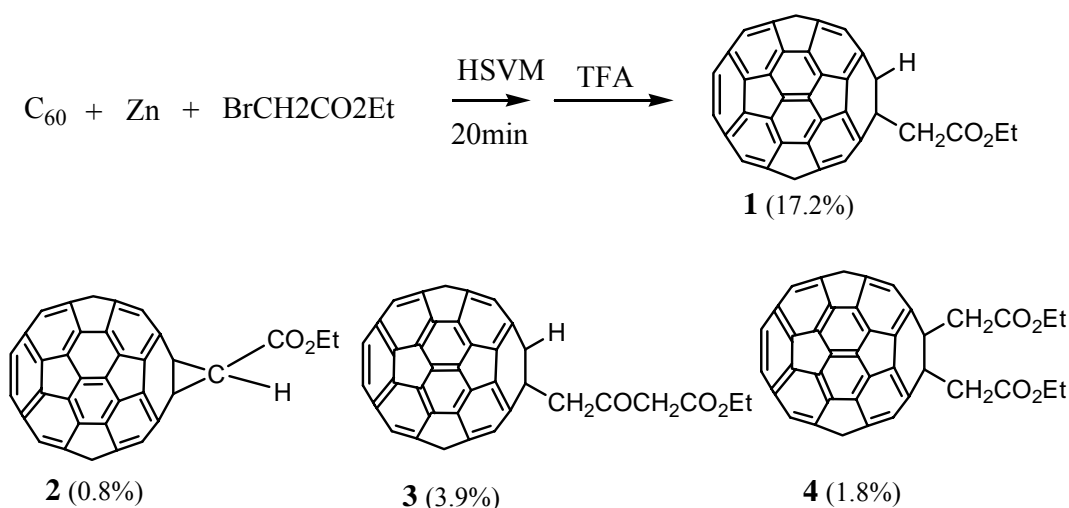


**Figure 1.13** Reaction of C<sub>60</sub> with zinc and diethyl bromoacetate under the HSVM condition.

#### 1.4.2.2 Synthesis of Fullerene Dimers

The formation, structure, and characteristics of all-carbon fullerene oligomers and polymers are particularly interesting due to their potential application in molecular devices, optoelectronics and nanotechnology. It has been suggested that, fullerene dimer with [2+2] structure is the essential subunit in the fullerene oligomers and polymers.<sup>56,57</sup> Thus, the preparation and characterization of fullerene dimers are of importance for understanding the structures, properties and applications of the fullerene oligomers and polymers.

C<sub>60</sub> reacts with cyanide in a solution of o-dichlorobenzene (ODCB)-DMF to produce a stable anion (CN)C<sub>60</sub><sup>-</sup> and the anion can be quenched with different electrophiles to afford cyanated C<sub>60</sub> derivatives.<sup>58</sup> Compared with the reaction in the liquid phase, the solid-state reaction of C<sub>60</sub> with KCN under the HSVM condition for 30 minutes afforded the formal [2+2] dimer C<sub>120</sub> in a yield of 18% unexpectedly along with 70% of recovered C<sub>60</sub> (Figure 1.14).<sup>59</sup> Furthermore, no cyanated product **5** was isolated and the high selectivity of the C<sub>120</sub> synthesis

is ascribed to a reaction mechanism which is totally different from that in the liquid phase. It has been shown by X-ray crystal structure that the dumb-bell shaped  $C_{120}$  is connected by a cyclobutane and this four-membered ring is square rather than rectangular as predicted theoretically.<sup>59</sup>

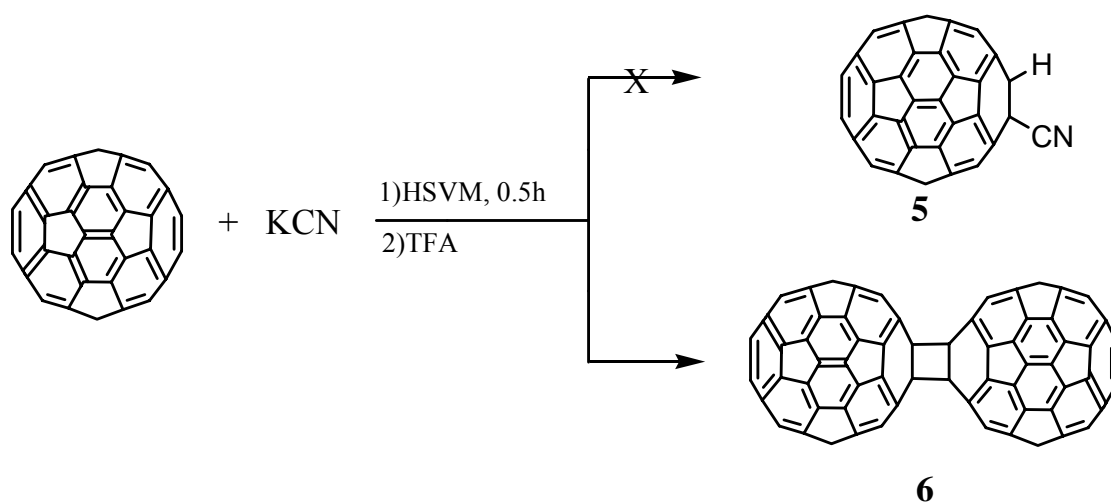


**Figure 1.14** Synthesis of  $C_{120}$  from  $C_{60}$  and KCN under the HSV condition.

The [2+2] structure of  $C_{120}$  is stable and does not rearrange to other peanut shaped structure isomers. However, it was found to dissociate quantitatively into  $C_{60}$  by heating its o-dichlorobenzene (ODCB) solution at  $175^{\circ}\text{C}$  for 15 minutes.<sup>59</sup> The amount of KCN does not need to be molar equivalent to that of  $C_{60}$ . Other salts such as  $\text{K}_2\text{CO}_3$  and  $\text{CH}_3\text{CO}_2\text{K}$ , which contain nucleophilic anions, were found to be as effective as KCN. Alkali metals and other metals, such as Mg, Al and Zn, are also found to work well in the dimerization of  $C_{60}$ . The reaction of  $C_{60}$  with these salts appears to reach an equilibrium state, giving a mixture of  $C_{60}$  and  $C_{120}$  in a weight ratio of 7:3 either starting from a mixture of  $C_{60}$  and chosen salt or from the pure  $C_{120}$ .<sup>59</sup>

Other dimers, such as  $C_{130}$  and  $C_{140}$  can be synthesized in the similar way as shown above.<sup>60,61,62</sup> Interestingly, even the trimer of  $C_{60}$ ,  $C_{180}$ , could be formed in the HSV process in a yield of 4%.<sup>63</sup>

### 1.4.2.3 [4+2] Cycloaddition Reactions

The [4+2] cycloaddition of  $C_{60}$  with anthracene is a well investigated reaction in solution.<sup>64,65</sup> The yield of the 1:1 adduct does not exceed 39% in the conventional thermal conditions. When the solid-state reaction was conducted under the present HSVM conditions for a 1:1.2 mixture of  $C_{60}$  and anthracene for 1h, the yield of the monoadduct was found to increase to 55%, with a yield of 19% isomeric mixture of biadduct (Figure 1.15).<sup>66</sup> The reaction appeared to reach an equilibrium state between reactants and products after 30 min. A time dependence of the reverse reaction was also investigated starting from the monoadduct and it was found that a mixture with a similar component ratio was obtained, which demonstrated that a chemical equilibrium was established under the present solid-state reaction system in spite of the heterogeneous reaction conditions.

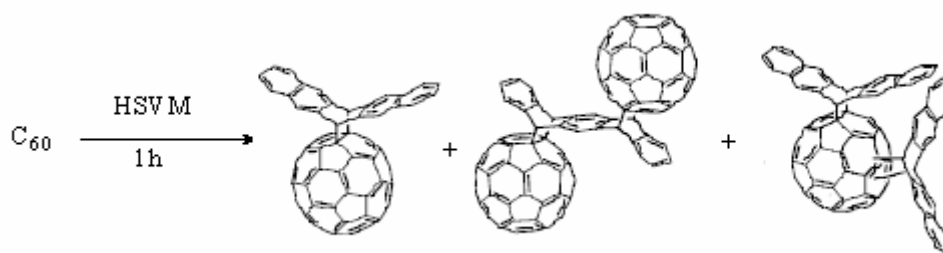


**Figure 1.15** Reaction of  $C_{60}$  with pentacene under the HSVM condition.

Other Diels-Alder reactions, such as the reaction of  $C_{60}$  with pentacene<sup>67</sup> and reaction of  $C_{60}$  with Phthalazine,<sup>68</sup> were also reported.

### 1.4.2.4 [3+2] Cycloaddition Reactions

For the thermal reaction of organic azides and  $C_{60}$  in solution, it was reported that triazoline derivatives were formed only at low temperatures and the triazolines were converted to 5,6-open and 6,6-closed azafullerenes by heating the solution to 100°C.<sup>69</sup> The HSVM reaction of  $C_{60}$  and azides was carried out for 30 min to afford triazoline derivative **7** in 62-76% yield (Figure 1.16). The 5,6-open and 6,6-closed azofullerenes **8** and **9** were formed in higher yields

than in solution when compound **7** was heated in the solid state at 120°C for 2h (Figure 1.16).

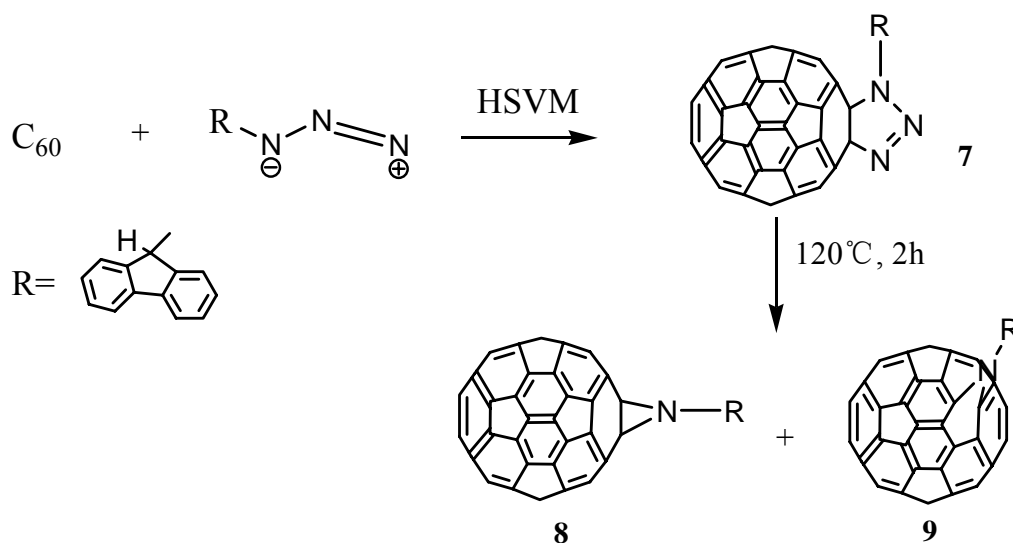


**Figure 1.16** Reaction of  $C_{60}$  with azides under HSVM conditions followed by thermal solid-state reaction.

The Prato reaction can also be performed on  $C_{60}$  under solvent-free conditions. The HSVM reaction of  $C_{60}$  with one equivalent of N-methylglycine and one equivalent of an aldehyde afforded the expected fulleropyrrolidines **10a-e** in moderate yields (Figure 1.17).<sup>70</sup>

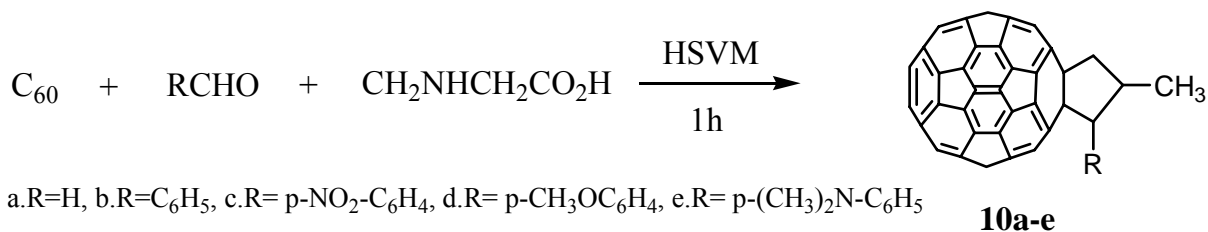


**Figure 1.17** Prato reaction of  $C_{60}$  under the HSVM condition.

#### 1.4.2.5 Reaction of Organic Bromides and Alkali Metals with $C_{60}$

In the early stage of fullerene chemistry, the reactions of  $C_{60}$  with organolithiums and Grignard reagents in solution that afforded alkyl, aryl or alkynyl  $C_{60}$  derivatives were reported.<sup>71,72</sup> The HSVM technique was applied to such a reaction. The reaction of  $C_{60}$  with aryl or alkyl bromide and metal (Li, Na, K, Mg) in a molar ratio of 1: (2-3): (4-6) was conducted under HSVM conditions for 30 min. This was followed by acidification of the

reaction mixture to afford the corresponding aryl or alkyl C<sub>60</sub> derivatives in moderate yield and a small amount of C<sub>120</sub> (Figure 1.18).<sup>73</sup>

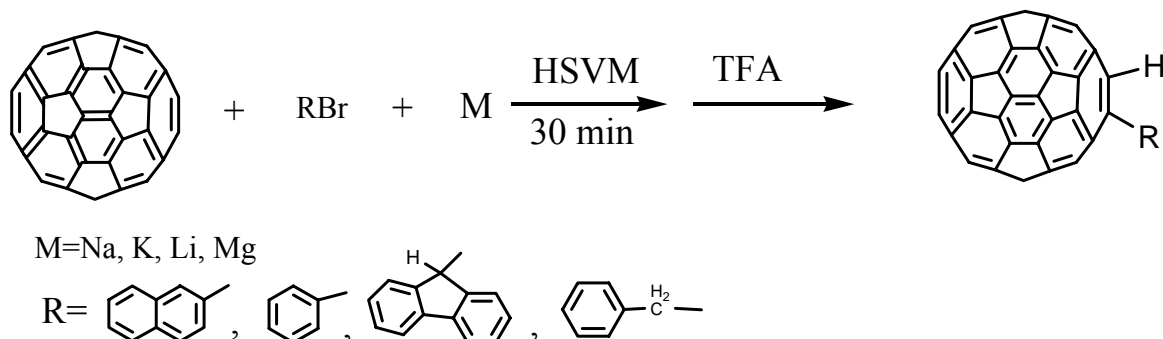


**Figure 1.18** Reactions of C<sub>60</sub> with alkali metals and bromides under the HSVM condition.

#### 1.4.2.6 Reaction of Dichlorodiphenylsilane and Lithium with C<sub>60</sub>

The HSVM reaction of C<sub>60</sub> with a silicon species such as silylene,<sup>74</sup> disilirane and silyllithium,<sup>75,76</sup> has been noted to give mono- or disilyl derivatives of C<sub>60</sub>. As shown in Figure 1.19, the HSVM reaction of C<sub>60</sub> with dichlorodiphenylsilane and lithium powder for 30 min afforded adduct **11** (7.5%) and recovered C<sub>60</sub> (67.4%) while the HSVM reaction of C<sub>60</sub> with alkyl bromide and lithium powder for 30 min yielded the alkyl C<sub>60</sub> derivatives.<sup>77</sup> It was assumed that the C<sub>60</sub> radical anion formed via single-electron transfer mechanism played an important role in the reaction although the detailed mechanism is not quite clear.

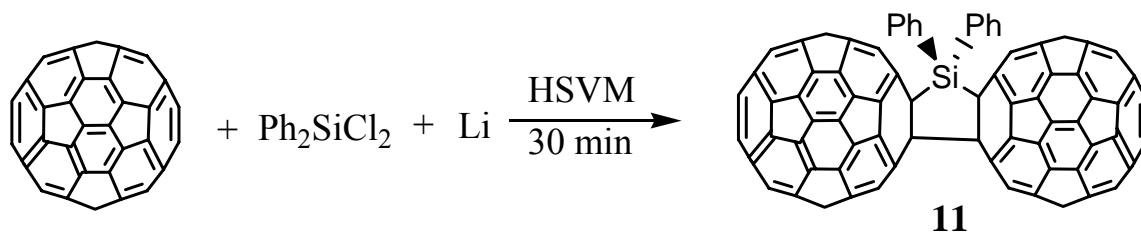


**Figure 1.19** Reactions of C<sub>60</sub> with dichlorodiphenylsilane and lithium under the HSVM condition.

## 1.5 Medical Application of Endohedral metallofullerene derivatives.

Although available only in small quantities now, endohedral metallofullerene derivatives have demonstrated potential applications in medical science, such as novel diagnostic and therapeutic radiopharmaceuticals<sup>78,79</sup> and new proton magnetic resonance imaging (MRI) contrast agents. Their unique properties (all-carbon shell with a large surface, a hollow core capable of accommodating up to three lanthanide ions, a cage structure protecting metal ions from releasing into biologic system and a proven chemical reactivity of surface carbon atoms for functionalization purposes) distinguish endohedral metallofullerenes from all others contrast agents for delivering metal ions *in vivo* for medical purposes.

### 1.5.1 MRI contrast agents

Magnetic resonance imaging (MRI) is one of the main diagnostic tools used in the medical field. MRI contrast agents are administered to change the relaxation of radio-frequency irradiated water protons to provide an image with sharper contrast results. The most commonly used MRI contrast agents are Magnevist<sup>TM</sup> (Gd-DTPA) and Omniscan<sup>TM</sup> (Gd(DTPA-BMA)) (Figure 1.20). These two agents are highly water-soluble and contain Gd<sup>3+</sup> (S = 7/2), which is paramagnetic due to 7 unpaired electrons on 4f orbital. It was found that the formation of a direct Gd<sup>3+</sup>-H<sub>2</sub>O bond is responsible for the relaxation and the faster of the exchange with nearby water molecules, the brighter the resulting image will be. However, there are several problems with the use of this agent. It may dissociate and release toxic Gd<sup>3+</sup> ions to the surrounding tissue. Furthermore, [Gd(DTPA)(H<sub>2</sub>O)]<sup>-2</sup> is unstable to acidic conditions.<sup>80</sup> These problems prompted the need for a new class of MRI contrast agents. The new contrast agents must meet these requirements: (1) enhance the proton relaxation rate significantly; (2) localize in the target tissue for a period of time and (3) Possess good stability and non-toxicity. Also, the new contrast agents must be water-soluble to enhance the proton relaxation of water.

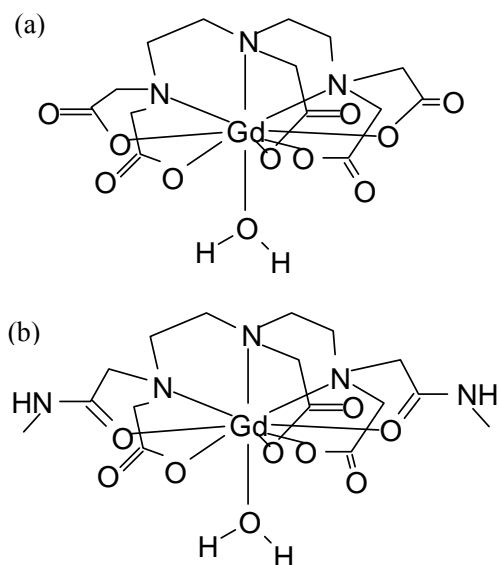


**Figure 1.20** Structures of commercial MRI agents (a) Magnevist™ and (b) Ominiscan™.

Water-soluble Gd-based endohedral metallofullerenes can be the next generation MRI contrast agents. Several groups reported that  $\text{Gd}@C_{82}(\text{OH})_x$ , a new metallofullerol, demonstrated a proton magnetic relaxivity rate ( $T_1$ ) much higher than the commercial compound's rate.<sup>57,81,82</sup> Since the surrounding water molecules cannot directly interact with the  $\text{Gd}^{3+}$  ion inside the cage, the higher relaxation rate is proposed to occur from an electronic interaction between the water molecules and paramagnetic ( $S = 1/2$ ) cage of the metallofullerenol. Due to the large surface area of the paramagnetic cage, it can interact with numerous water molecules simultaneously via hydrogen bonding.

Recently, Shinohara et al. synthesized water-soluble polyhydroxylated  $\text{M}@C_{82}$  ( $M = \text{La}, \text{Ce}, \text{Dy}, \text{Gd}$  and  $\text{Er}$ ). The relaxivity measurement showed the relaxation rates ranged from 0.8 to 73  $\text{sec}^{-1}\text{mM}^{-1}$  at 0.47 T.<sup>65</sup> More recently, two water-soluble endohedral gadofullerene derivative,  $\text{Gd}@C_{60}(\text{OH})_x$  and  $\text{Gd}@C_{60}[\text{C}(\text{COOH})_2]_{10}$  were synthesized and characterized with regard to their MRI contrast agent properties.<sup>83,84,85</sup> Relaxivities were measured as the functions of temperature (278-335K) and magnetic field ( $5 \times 10^{-4}$  to 9.4 T). The nanoscale aggregation studies of these two metallofullerene MRI contrast agents revealed that both of these two species aggregate in aqueous solution with sizes ranging from 30 to 90 nm at  $\text{pH} = 9$ .<sup>84</sup>

### 1.5.2 X-ray Contrast agents

X-ray contrast agents are a class of pharmaceuticals that, when administered to a patient, enter and pass through anatomic regions of interest to provide enhanced X-ray imaging. Most X-ray contrast agents contain large  $Z$  (atomic number) elements and there are two types of X-ray contrast agents currently approved for human use: barium sulfate suspensions and water-soluble aromatic iodinated contrast agents. Recently, research efforts have been made to develop a completely different category of X-ray contrast agents based on the electron-dense heavy metals. For a heavy-metal X-ray contrast agent, it must possess these attributes: (1) high water solubility; (2) stable in physiological pH at room temperature; (3) similar pharmacokinetic profile to that of currently used agents and (4) Extremely safe, causing minimal patient discomfort.<sup>86</sup>

In 2002, Dorn et al. reported the synthesis and characterization of another TNT endohedral metallofullerene,  $\text{Lu}_3\text{N}@C_{80}$ .<sup>87</sup> They also showed the ability of  $\text{Lu}_3\text{N}@C_{80}$  to provide X-ray contrast, which is attributed to the large atom number ( $Z$ ) of the lutetium atoms. In their experiment,  $\text{Lu}_3\text{N}@C_{80}$  was distributed onto a non-absorbing Teflon block and irradiated with X-rays. As shown in Figure 1.21,  $\text{Lu}_3\text{N}@C_{80}$  demonstrated X-ray contrast while two controls (one is a Teflon block that lacks the lutetium species, the other is a Teflon block containing  $C_{60}$ ) did not exhibit contrast.

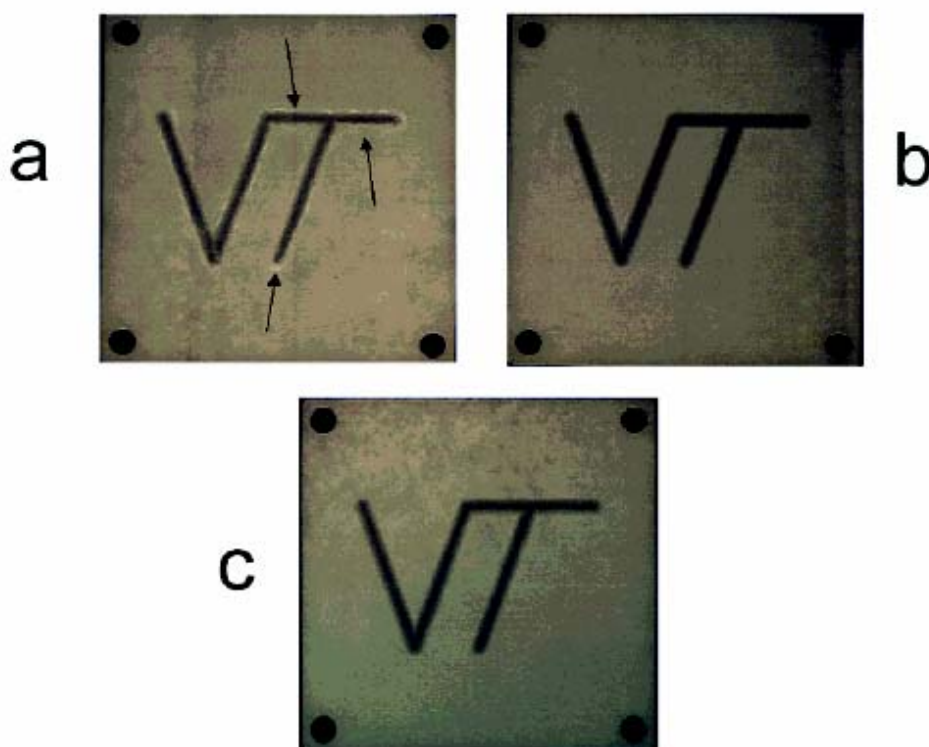


**Figure 1.21** X-ray photograph of (a) contrast provided by  $\text{Lu}_3\text{N}@C_{80}$  on a Teflon block, (b)  $C_{60}$  fullerene on a Teflon block, and (c) a blank Teflon block. The sample was exposed for 3.5 min at 30 kV.

### 1.5.3 Fluorescence

The photophysical properties (such as fluorescence) of fullerenes, especially  $C_{60}$  and  $C_{70}$ , have been extensively studied since the discovery of fullerenes.<sup>88,89,90,91</sup> Experimental data have shown the fluorescence quantum yield of  $C_{60}$  is very low, due to the intersystem crossing from singular state to the excited triplet state and the forbidden electronic transitions between the excited singlet states and ground state.

In 1998, a series of terbium-based endohedral metallofullerenes,  $\text{Tb}_2@C_{2n}$  were synthesized and characterized. Interestingly, the solid-state fluorescent emission spectra showed that these Tb-based metallofullerenes had good fluorescent emission properties.<sup>92</sup> Recently the fluorescence spectra of the yttrium-based metallofullerene,  $\text{Y}@C_{82}$  in different polar solvents (such as DMF, DMSO) were reported and it was shown that the fluorescence of  $\text{Y}@C_{82}$  is much stronger than that of  $C_{60}$ , due to aggregation of  $\text{Y}@C_{82}$  in polar solvents.<sup>93</sup>

#### 1.5.4 Radiolabelling agents

Holmium metallofullerenes have been studied as potential radio-tracers in nuclear medicine. In 1999, Wilson et al. studied the neutron-bombardment of the water-soluble holmium metallofullerenols,  $^{165}\text{Ho}@C_{82}(\text{OH})_x$  ( $x = 24-26$ ) using a highly thermal neutron source.<sup>78</sup> When neutron activated,  $^{165}\text{Ho}@C_{82}(\text{OH})_x$  was converted to  $^{166}\text{Ho}@C_{82}(\text{OH})_x$ . Biodistribution studies of this radioactive species were conducted using BALB/c mice. The results showed that the radiotracer is localized primarily in the liver with slow clearance over 48 hours. However, localization in bone had gradually increased over the 48-hour time period. These results demonstrate the feasibility of using endohedral metallofullerene derivatives as radiotracers for *in vivo* studies.

## CHAPTER 2 - Project Overview

My research work concerns the functionalization of trimetallic nitride endohedral metallofullerenes under the HSVM condition. As discussed in Chapter 1, several functionalizations have been performed with trimetallic nitride endohedral metallofullerenes ( $\text{Sc}_3\text{N}@C_{80}$ ,  $\text{Y}_3\text{N}@C_{80}$  and  $\text{Gd}_3\text{N}@C_{80}$ ). However, until now the reactivity has not been intensively studied, not only because trimetallic nitride endohedral metallofullerenes are less reactive than  $C_{60}$ , but only small amounts of material (ca. 1-10 mgs) are available to perform chemical reactions.

The HSVM technique has been shown to be effective in the functionalization of empty-cage fullerenes, such as  $C_{60}$  and  $C_{70}$ . The HSVM reactions of fullerenes have advantages over the solution reactions due to the solubility problem of fullerenes and environmental concerns by alleviating the usage of organic solvent. However, the HSVM technique has not yet been applied to functionalizing endohedral metallofullerenes.

The majority of the functionalization work in this project was performed under the HSVM condition. The initial motivation of this project is to synthesize the bisadduct of  $\text{Sc}_3\text{N}@C_{80}$  malonate derivative by using the HSVM technique since the similar functionalization under the HSVM condition has been proved effective on  $C_{60}$ . However, the HPLC trace and MALDI-TOF mass spectrum did not show any evidence of the formation of the bisadduct of metallofullerene derivative. Other functionalizations, such as the Prato reaction, were also attempted with  $\text{Sc}_3\text{N}@C_{80}$  under the HSVM condition and none of these methods were successful.

Finally I discovered the hydroxylation of  $\text{Sc}_3\text{N}@C_{80}$  under the HSVM condition unexpectedly. After the mixture of  $\text{Sc}_3\text{N}@C_{80}$ ,  $^{13}\text{CH}_2(\text{COOEt})_2$  and  $\text{Na}_2\text{CO}_3$  was vigorously shaken under the HSVM reaction for 14 hours, the reaction mixture was dissolved in toluene. However, there was some precipitate in the toluene solution. The precipitate was separated by centrifuging the mixture and was dissolved into deionized water to produce a golden-colored aqueous solution. After further purification, it was characterized by FT-IR, XPS and MALDI-TOF mass spectrum. This characterization confirmed the structure of

polyhydroxylated product,  $\text{Sc}_3\text{N}@C_{80}(\text{OH})_m(\text{O})_n$ . In further studies, it was discovered that the HSVM reaction could occur even without the existence of diethyl malonate. Other bases, such as NaOH and KOH could be used, but resulted in lower yields.

This HSVM reaction was also performed with other trimetallic nitride endohedral metallofullerenes to yield  $\text{A}_3\text{N}@C_{80}(\text{OH})_m(\text{O})_n$  ( $\text{A} = \text{Gd}, \text{Ho}$ ). The relaxivities of these trimetallic nitride endohedral metallofullerols were studied at three different magnetic fields, 0.35 T, 2.4 T and 9.4 T. It was shown that  $\text{Gd}_3\text{N}@C_{80}(\text{OH})_m(\text{O})_n$  has an enhanced  $r_1$  proton relaxivity, which is similar or even better than other reported gadofullerols and possesses the potential to be the next generation MRI contrast agents. Interestingly,  $\text{Ho}_3\text{N}@C_{80}(\text{OH})_m(\text{O})_n$  was shown to have a large  $r_2/r_1$  ratio, which indicates it may be used as a  $T_2$  contrast agent.

Mixed-metal endohedral metallofullerenes species are of great importance in the application of trimetallic nitride endohedral metallofullerenes. With this in mind,  $\text{Ce}_x\text{Sc}_{3-x}\text{N}@C_{80}$  ( $x = 1-2$ ) was synthesized and the more abundant one,  $\text{CeSc}_2\text{N}@C_{80}$  was isolated and characterized by DCI mass, UV-Vis,  $^{13}\text{C}$  and  $^{45}\text{Sc}$  NMR, XPS and single-crystal X-ray diffraction study. The Ce ion was confirmed to have a +3 charge and the crystal data showed the planar  $\text{CeSc}_2\text{N}$  cluster was encapsulated into an  $I_h C_{80}$  cage.

The motions of the cage and the cluster in trimetallic nitride endohedral metallofullerenes are of interest due to the unique structure of these endohedral metallofullerenes. In the last section of this thesis, the  $^{45}\text{Sc}$  NMR studies of three trimetallic nitride endohedral metallofullerenes,  $\text{Sc}_3\text{N}@C_{2n}$  ( $2n = 68, 78, 80$ ), were performed and the dynamic behavior of the cage and the cluster was demonstrated.

# CHAPTER 3 - New MRI Contrast Agents: Face Preparations of Water-soluble TNT metallofullerols

## 3.1 Introduction

The study of water-soluble derivatives of endohedral metallofullerenes has attracted wide attention in recent years. The fullerene cage protects the encapsulated metal from external chemical attack and ensures against the release of toxic metal ions into the body. Thus, water-soluble metallofullerenes possess a unique potential for medical applications, such as magnetic resonance imaging (MRI) contrast agents,<sup>81-85,94</sup> x-ray contrast agents<sup>95</sup> and nuclear medicine.<sup>78-79</sup> For example, gadofullerols (such as  $\text{Gd}@C_{82}(\text{OH})_m$  and  $\text{Gd}@C_{60}(\text{OH})_n$ ) are being studied as prime candidates for next generation MRI contrast agents. Recent studies<sup>81-85,94,96</sup> have indicated that water-soluble Gd-containing metallofullerenes show enhanced relaxivities and are potential next generation MRI contrast agents. Biodistribution studies of  $^{166}\text{Ho}_x@C_{82}(\text{OH})_y$  ( $x = 1, 2$ ) by Cagle et al.<sup>78</sup> have demonstrated the feasibility of using endohedral metallofullerene compounds as radiotracers for *in vivo* studies.

We have previously reported the synthesis of very stable trimetallic nitride template (TNT) endohedral metallofullerenes,  $A_xB_{3-x}N@C_{80}$  ( $A, B = \text{metal}, x = 0-3$ ) in high yields by introducing nitrogen gas into the Krätschmer-Huffman (K-H) generator during vaporization of packed graphite rods containing various metal oxides.<sup>5</sup> The TNT endohedral metallofullerenes have inherent advantages over mono-metallofullerenes, such as  $M@C_{60}$  and  $M@C_{82}$ , because of the encapsulation of up to three Gd or Ho atoms inside the carbon cage as in the recently reported  $\text{Gd}_3\text{N}@C_{80}$ <sup>97,98</sup> and  $\text{Ho}_3\text{N}@C_{80}$ .<sup>99</sup> Furthermore, the incorporation of different metal clusters,  $A_xB_{3-x}N$  ( $x=1-2$ ),<sup>87</sup> would enable multimodal diagnostic applications (e.g. X-ray, fluorescence, radiolabelling and MRI). The previous study showed the pegylated hydroxylated  $\text{Gd}_3\text{N}@C_{80}$  derivative,  $\text{Gd}_3\text{N}@C_{80}[\text{DiPEG5000}(\text{OH})_x]$  exhibited strong proton relaxivities and improved *in vivo* imaging in animal study.<sup>96</sup>

As discussed in chapter 1, high-speed vibration milling (HSVM) has been used in the chemical modification of fullerenes,<sup>51</sup> because it can alleviate the problem of low fullerene solubility in common organic solvents. It is worth noting that recently Zhang et al.<sup>100</sup> applied

the HSVM technique to the synthesis of [60]fullerols by converting the hydrophobic starting material  $C_{60}$  into a hydrophilic product  $C_{60}(OH)_x$  in one step with a moderately high yield (84%). Compared with the synthesis of fullerols in the solvents, this HSVM reaction not only shortens the reaction time from around two days to several hours, but also has significantly higher yields.

Recently, efforts have been made to obtain purified EMFs by methods that alleviate time-consuming high performance liquid chromatography (HPLC) purification. Gu and coworkers<sup>101</sup> have developed a new chemical reduction method for the selective isolation of endohedral metallofullerenes from the Krätschmer-Huffman raw soot. For example,  $Gd@C_{82}$  and  $Gd_2@C_{80}$  were selectively reduced and extracted with high purity and yield. More recently, Dorn et al. reported that pure TNT EMFs,  $A_3N@C_{80}$  ( $A =$  lanthanide atom, e.g., Gd, Ho, Lu), can be obtained from crude soots in a single, facile step based on selective chemical reactivity.<sup>23</sup> More details of this protocol will be discussed in chapter 4.

In this chapter, the facile preparations of three water-soluble TNT endohedral metallo-fullerols  $A_3N@C_{80}(OH)_m(O)_n$  ( $A =$  Sc, Gd, Ho) will be reported. By utilizing the new purification protocol and the HSVM technique, the TNT endohedral metallofullerols can be synthesized from Krätschmer-Huffman raw soot in an overall time of only two days. This time savings is a very important consideration for ultimate applications involving preparation of radiopharmaceutical agents with short half-lives (e.g.  $^{166}Ho$  and  $^{177}Lu$ ,  $t_{1/2}=1.1$  days<sup>78</sup> and 6.61 days,<sup>102</sup> respectively). Furthermore, the synthesized gadofullerols possess significantly enhanced  $r_1$  relaxivity, while the holmium-based metallofullerols show potential as the  $T_2$  contrast agents.

## 3.2 Results and Discussions

### 3.2.1 Synthesis of TNT Endohedral Metallofullerols Under the HSVM Condition

As previously reported,  $A_3N@C_{80}$  ( $A = Gd, Ho, Sc$ ) was obtained from raw soot by applying the extract toluene solution to a column packed with cyclopentadiene-functionalized Merrifield resin in toluene and flushing with toluene.<sup>23</sup> The purity of the effluent,  $A_3N@C_{80}$ , was confirmed by HPLC traces. The solvent was removed in vacuo and the resultant  $A_3N@C_{80}$  was allowed to react with sodium carbonate under the HSVM condition for 14 hours to yield water-soluble TNT endohedral metallo-fullerols,  $A_3N@C_{80}(OH)_m(O)_n$  (Figure 3.1).

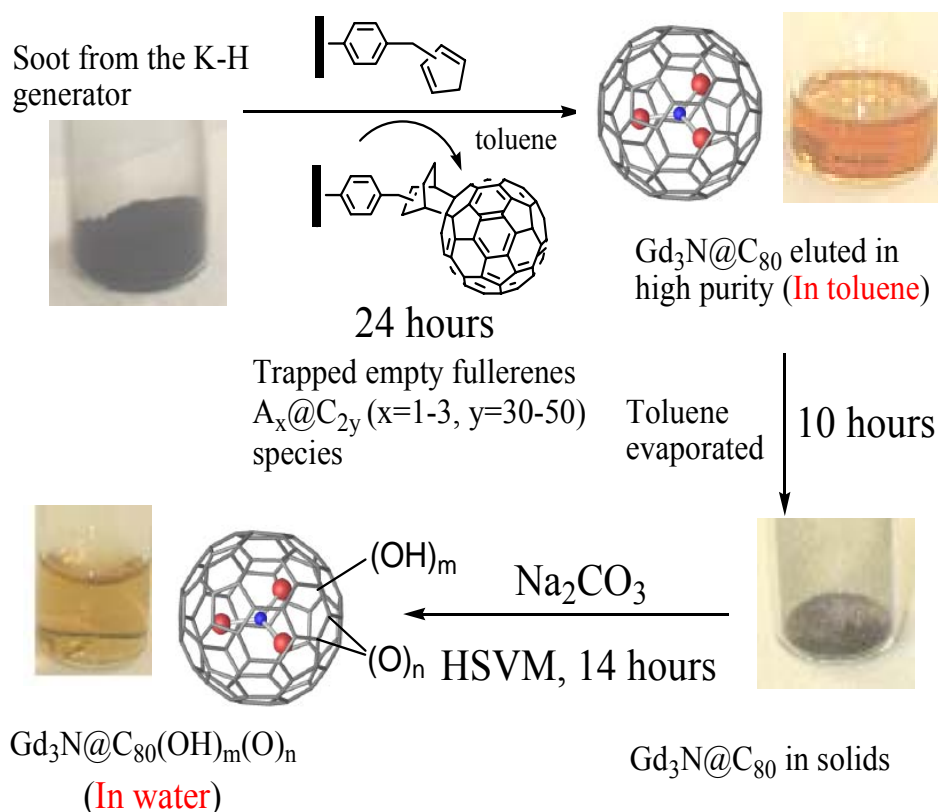


**Figure 3.1** Facile preparations of TNT endohedral metallofullerols  $A_3N@C_{80}(OH)_m(O)_n$  ( $A = Sc, Gd, Ho$ ).

$Gd_3N@C_{80}(OH)_m(O)_n$  was illuminated as an example.

### 3.2.2 Characterization of TNT metallofullerols

The synthesized TNT endohedral gadofullerols were characterized by FT-IR, XPS (X-ray photoelectron spectroscopy) and MALDI-TOF (matrix-assisted laser desorption time-of-flight) mass spectrum. As shown in Figure 3.2, The FT-IR spectrum shows a broad peak at  $3363.99\text{ cm}^{-1}$  for the hydroxyl groups attached to the carbon cage. A strong peak at  $1606.35\text{ cm}^{-1}$  corresponds to the remaining  $\pi$ -bonded carbons (C=C), while both the OH deformation stretching peak,  $1326.1\text{ cm}^{-1}$ , and C-O stretching absorption peak,  $1107.70\text{ cm}^{-1}$ , appear strong and broad.

The XPS spectrum (Figure 3.3) of  $\text{Gd}_3\text{N}@C_{80}(\text{OH})_m(\text{O})_n$  film on gold surface indicates the different types of functionalized carbon atoms on the carbon cage. The asymmetric spectrum for the core level region of carbon (C 1s) demonstrates that oxidation of the cage has occurred, and a curve fitting of the region presents four distinct peaks as illustrated in Figure 3.3. The largest peak,  $285.12\text{ eV}$  (68.0%), corresponds to the remaining  $\pi$ -bonded carbons of the cage, which is consistent with  $\text{sp}^2$  non-functionalized carbon atoms, while the peaks at  $286.81\text{ eV}$  (13.9%) and  $288.51\text{ eV}$  (11.4%) contribute from the hydroxylated (-C-OH) and highly oxygenated carbon atoms (ether linkages or peroxides), respectively. The corresponding areas of the oxygenated carbon (hydroxylated and highly oxygenated) peaks suggest metallofullerols with the formula  $\text{Gd}_3\text{N}@C_{80}(\text{OH})_{\sim 15}(\text{O})_{\sim 8}$ . These results agree very well with previously reported FT-IR spectra of endohedral metallofullerols.<sup>35,103</sup>

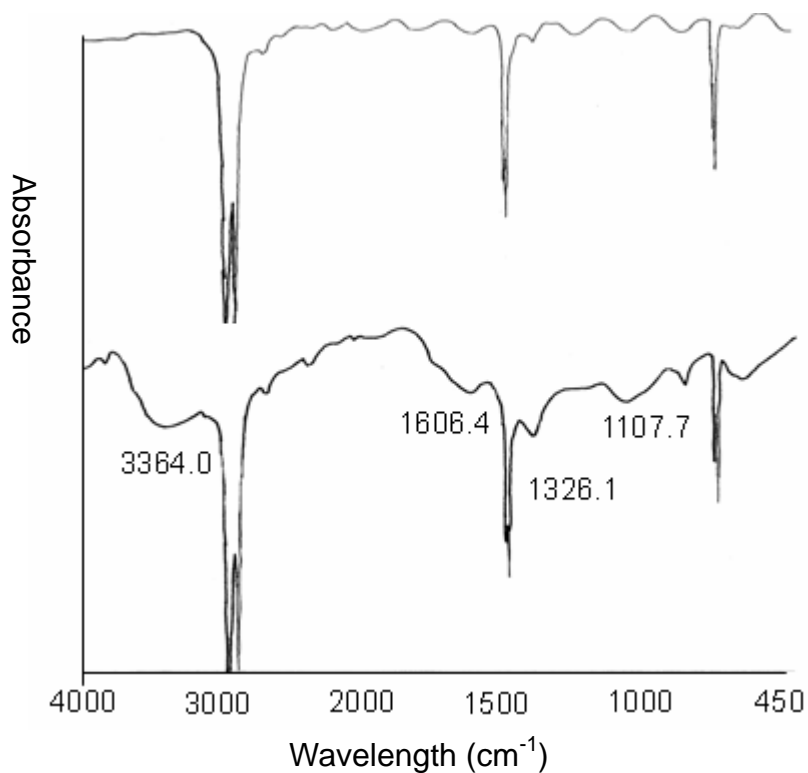


**Figure 3.2** The FT-IR spectra of blank polyethylene card (above) and Gd<sub>3</sub>N@C<sub>30</sub>(OH)<sub>m</sub>(O)<sub>n</sub> on a polyethylene card (bottom).

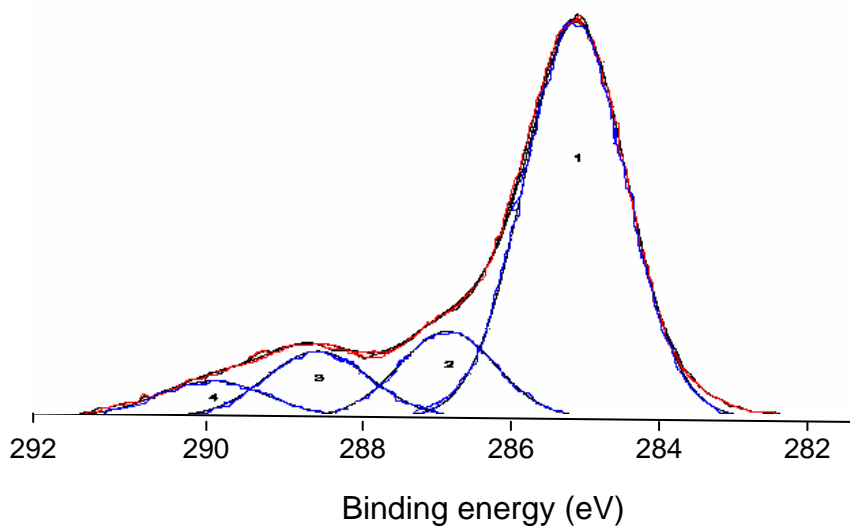


**Figure 3.3** C1s XPS spectrum of TNT endohedral gadofullerols on a gold foil ( the original curve is red while the fitting curve is blue).

MALDI-TOF MS shows a strong peak at  $m/z=1446.6$ , which corresponds to the parent endohedral metallofullerenes, Gd<sub>3</sub>N@C<sub>80</sub> (Figure 3.4). However, in contrast to MS spectra of hydroxylated metallofullerenes which showed just a single peak of parent metallofullerenes in

previous reported cases,<sup>35,103</sup> several moderate peaks at  $m/z=1462.7$ ,  $1479.6$ ,  $1495.5$ ,  $1511.6$ ,  $1527.4$  yield the evidence of existence of hydroxyl groups and linkage oxygens or peroxides outside the carbon cage.

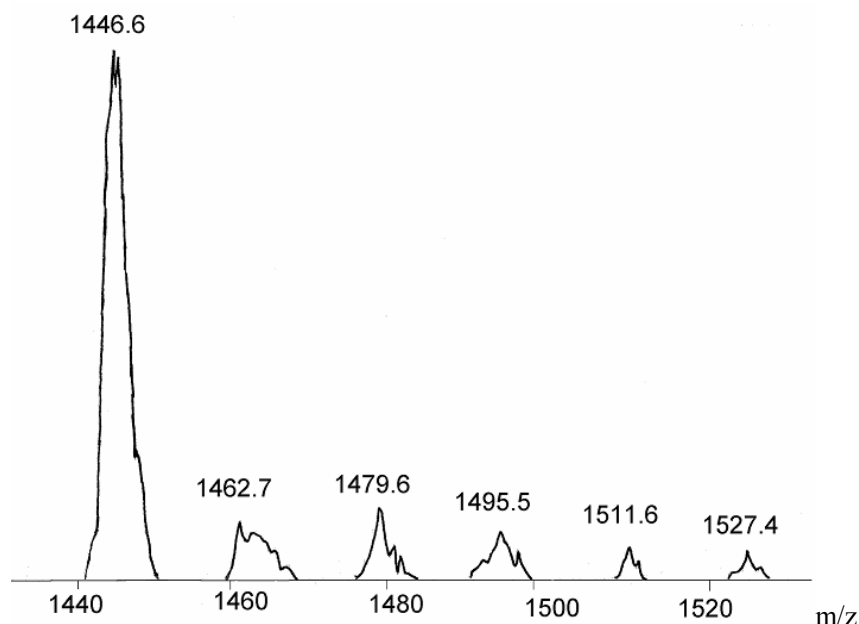


**Figure 3.4** MALDI-TOF mass spectrum of partially decomposed TNT endohedral gadofullerols (Positive mode, a saturated sulfur solution in carbon disulfide as a matrix).

### 3.2.3 Relaxivity studies of TNT metallofullerols

Several groups have recently reported relaxivity results for water-soluble gadofullerols which are potential next generation MRI contrast agents. For example, Zhang et al.<sup>104</sup> reported an  $r_1$  value of  $47 \text{ mM}^{-1}\text{s}^{-1}$  (at 9.4 T) for a mixed sample of empty fullerene and polyhydroxyl gadofullerene compounds. Wilson and coworkers<sup>105</sup> presented  $r_1 = 20 \text{ mM}^{-1}\text{s}^{-1}$  for  $\text{Gd@C}_{82}(\text{OH})_x$  (at 0.47 T and  $40^\circ\text{C}$ ) while Shinohara et al.<sup>81</sup> reported a somewhat higher value  $r_1 = 67 \text{ mM}^{-1}\text{s}^{-1}$  for  $\text{Gd@C}_{82}(\text{OH})_x$  ( $x \approx 40$ ) (at 0.47 T and  $25^\circ\text{C}$ ) and  $r_1 = 81 \text{ mM}^{-1}\text{s}^{-1}$  (at 1.0 T and  $25^\circ\text{C}$ ). More recently, Tóth et al.<sup>85</sup> has measured  $r_1$  relaxivities of  $\text{Gd@C}_{60}(\text{OH})_x$  and  $\text{Gd@C}_{60}[\text{C}(\text{COOH})_2]_{10}$  as a function of magnetic field ( $5 \times 10^{-4}$  to 9.4 T) at variable temperature (278-335K). These  $r_1$  values are significantly higher than the relaxivities of most commercially used contrast agents, e.g.,  $\text{Gd}^{\text{III}}$  (DTPA).

As shown in Table 3.1, the measured  $r_1$  water relaxivity values obtained in the current study

for  $\text{Gd}_3\text{N}@C_{80}(\text{OH})_m(\text{O})_n$  prepared under the HSVM condition at both low (0.35 T) and high (9.4 T) fields are consistent with the studies noted above. The Gd-content of the samples was measured by Inductive Coupled Plasma (ICP) (see Experimental section). Under similar conditions (magnetic field strength and temperature), the  $r_1$  relaxivities of  $\text{Gd}_3\text{N}@C_{80}(\text{OH})_m(\text{O})_n$  are approximately three times larger than  $\text{Gd}@C_{60}(\text{OH})_x$ <sup>85</sup> (29 vs ~8  $\text{mM}^{-1}\text{s}^{-1}$  at 9.4 T; 72 vs ~25  $\text{mM}^{-1}\text{s}^{-1}$  at 0.35 T), although the relaxivities per gadolinium atom for these two gadofullerols are nearly the same. It should be noted that the  $\text{Sc}_3\text{N}@C_{80}(\text{OH})_m(\text{O})_n$  sample serves as a reasonable diamagnetic control. The difference of relaxivities between  $\text{Gd}_3\text{N}@C_{80}(\text{OH})_m(\text{O})_n$  and  $\text{Sc}_3\text{N}@C_{80}(\text{OH})_m(\text{O})_n$  indicates the paramagnetism originates from the cluster encapsulated. However, the slightly enhanced  $r_2$  value is suggestive of some unpaired spin density on the fullerol cage surface, as also suggested for a similar sample by Shinohara.<sup>82</sup>

**Table 3.1** Relaxivities ( $r_1$  and  $r_2$ ) of  $\text{A}_3\text{N}@C_{80}(\text{OH})_m(\text{O})_n$  (A = Gd, Ho, Sc) at low and high concentrations at high (9.4 T) and low (0.35 T) magnetic fields

Contrast Agents (conc.)	$r_1(\text{mM}^{-1}\text{s}^{-1})$		$r_2(\text{mM}^{-1}\text{s}^{-1})$	
	0.35T	9.4T	0.35T	9.4T
$\text{Gd}_3\text{N}@C_{80}(\text{OH})_m(\text{O})_n$ (low) a]	72	29	143	111
$\text{Gd}_3\text{N}@C_{80}(\text{OH})_m(\text{O})_n$ (high) <sup>b]</sup>	29	17	52	45
$\text{Ho}_3\text{N}@C_{80}(\text{OH})_m(\text{O})_n$ (low) c]	1	7	22	62
$\text{Ho}_3\text{N}@C_{80}(\text{OH})_m(\text{O})_n$ (high) <sup>d]</sup>	0.3	2	12	51
$\text{Sc}_3\text{N}@C_{80}(\text{OH})_m(\text{O})_n$ <sup>e]</sup>	1	1	5	5

[a] concentration range is 0.5-8.0  $\mu\text{M}$  [b] concentration range is 15-120  $\mu\text{M}$  [c] concentration range is 0.5-8.0  $\mu\text{M}$  [d] concentration range is 16-254  $\mu\text{M}$  [e] concentration range is 10-157  $\mu\text{M}$

Interestingly, it was found that the relaxivities of the TNT gadofullerols are concentration dependent and increase with dilution. As shown in Figure 3.5, for two concentration ranges (high: 15-120  $\mu\text{M}$  and low: 0.5-8.0  $\mu\text{M}$ ) at both 9.4 T and 0.35 T, the  $r_1$  and  $r_2$  relaxivities of

gadofullerols at low concentration are much larger than those at high concentration. These results are consistent with earlier studies on  $\text{Gd}_3\text{N}@C_{80}[\text{DiPEG5000}(\text{OH})_x]$ .<sup>96</sup> The high relaxivity at low concentrations is especially beneficial in practical use because less contrast agent would need to be injected into the patients' body. The reason for this concentration dependency is not fully understood; however, it may be due to the formation of micelles of the TNT metallofullerols at higher concentrations. When the concentration is lower, there is less or even no aggregates formed and more water exchange can take place with the metallofullerols. To confirm the aggregation phenomenon, the critical micelle concentration needs to be determined in future work. The relaxivities of holmium-based metallofullerols also showed this concentration dependency at the same concentration range.

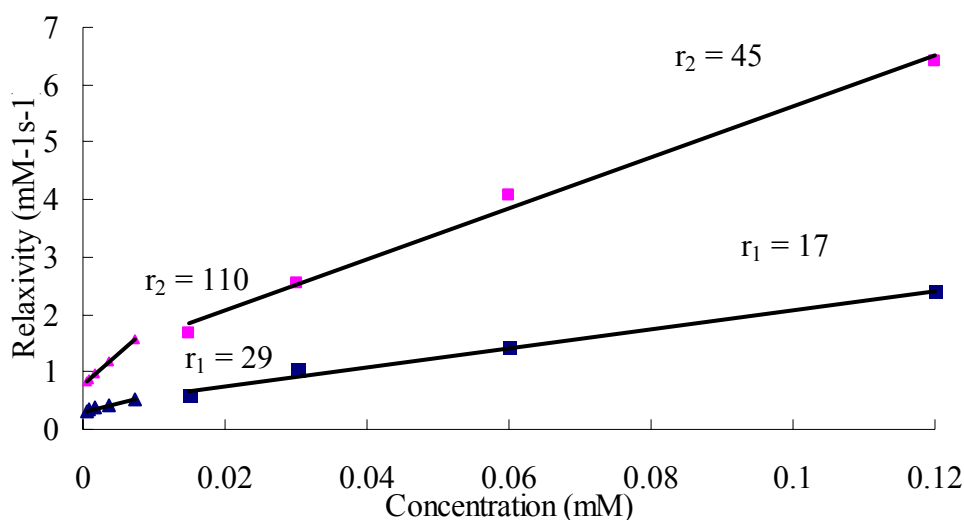


**Figure 3.5** Relaxivities of  $\text{Gd}_3\text{N}@C_{80}(\text{OH})_m(\text{O})_n$  at high field (9.4 T). The pink symbols represent the relaxivities data at low concentrations and the deep blue ones represent the relaxivities at high concentrations.

Due to the increasing demand for the pH-responsive MRI contrast agents in clinical applications, the relaxivities of  $\text{Gd}_3\text{N}@C_{80}(\text{OH})_m(\text{O})_n$  were also studied as a function of pH over a range of 2-12 at 9.4 T (Figure 3.6). The relaxivities increase significantly with decreasing pH values by a factor of 3.6 until  $\text{pH} \approx 3$  where precipitation begins. The relaxivity change with pH is totally reversible in the range 2-12. This pH dependence of the  $r_1$  relaxivities was also observed in the case of previously reported  $\text{Gd}@C_{60}(\text{OH})_x$ .<sup>85</sup> The origin of the change

in relaxivity of  $\text{Gd}_3\text{N}@C_{80}(\text{OH})_m(\text{O})_n$  may be the pH-dependent aggregation state of the molecules, as proposed in the case of  $\text{Gd}@C_{60}(\text{OH})_x$ .<sup>85</sup> At low pH values, the size of the Gd particle will become larger and give rise to the higher relaxivity, which is exclusively outer sphere in origin.

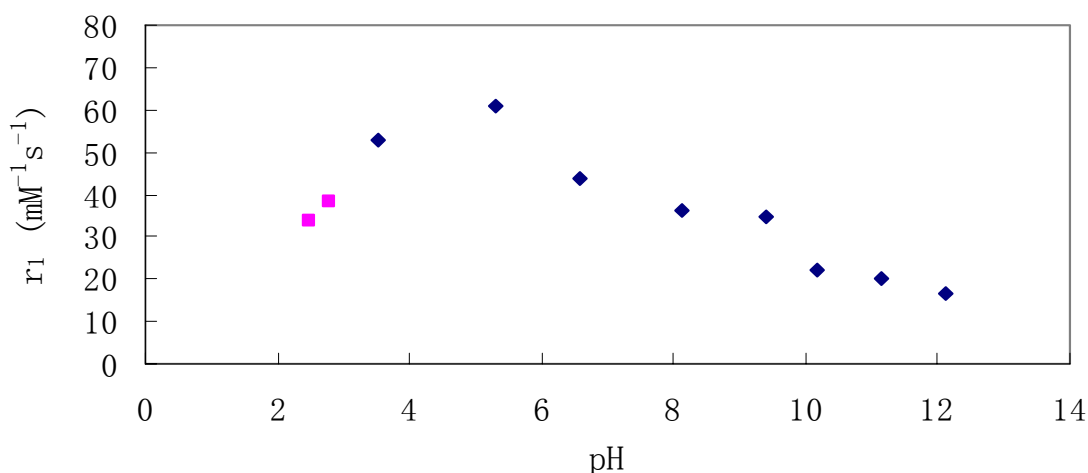


**Figure 3.6** pH dependence of the  $r_1$  relaxivities for  $\text{Gd}_3\text{N}@C_{80}(\text{OH})_m(\text{O})_n$  (0.004 mM) at 9.4 T and 23°C. All data were obtained by acidifying a basic solution. The pink symbols represent solutions with precipitation.

The  $r_2/r_1$  ratios for different contrast agents (Ominiscan,  $\text{GdCl}_3$  and  $\text{HoCl}_3$  were used as controls) were shown in Table 3.2. The  $r_2/r_1$  values of for  $\text{Ho}_3\text{N}@C_{80}(\text{OH})_m(\text{O})_n$  at both high and low concentration ranges are significantly higher than those for other agents. These results indicate the potential of holmium-based metallofullerols as the  $T_2$  contrast agents.

*In Vivo* and *In Vitro* imaging studies on  $\text{Gd}_3\text{N}@C_{80}(\text{OH})_m(\text{O})_n$  are needed to determine the possibility of being the next generation MRI contrast agent. Also the  $T_{1w}$  and  $T_{2w}$  contrast studies will be performed on  $\text{Ho}_3\text{N}@C_{80}(\text{OH})_m(\text{O})_n$  to explore its potential to be a  $T_2$  contrast agent.

**Table 3.2** Relaxivities ratio ( $r_2/r_1$ ) of  $A_3N@C_{80}(OH)_m(O)_n$  ( $A = Gd, Ho, Sc$ ) at low and high concentrations at high (9.4 T) and low (0.35 T) magnetic fields.

Contrast Agents (conc.)	$r_2/r_1$	
	0.35T	9.4T
$Gd_3N@C_{80}(OH)_m(O)_n$ (low) <sup>a]</sup>	2.6	1.8
$Gd_3N@C_{80}(OH)_m(O)_n$ (high) <sup>b]</sup>	3.8	2.0
Ominiscan <sup>c]</sup>	1.0	1.3
$GdCl_3$ <sup>d]</sup>	1.4	1.2
$Ho_3N@C_{80}(OH)_m(O)_n$ (low) <sup>e]</sup>	28.5	41.1
$Ho_3N@C_{80}(OH)_m(O)_n$ (high) <sup>f]</sup>	9.1	20.0
$HoCl_3$ <sup>g]</sup>	1.1	4.3
$Sc_3N@C_{80}(OH)_m(O)_n$ <sup>h]</sup>	4.9	3.7

[a,b,e,f,h] concentration ranges are the same as those in Table 1. [c] concentration range is 0.25-5 mM [d] concentration range is 23-360  $\mu$ M [g] concentration range is 48-762  $\mu$ M.

### 3.3 Experimental

#### 3.3.1 Materials and purification

Graphite rods (99.9995%C, 6.15 mm x 152 mm) and graphite powder (99.9995%C) were obtained from Alfa Aesar. Scandium (III) oxide ( $Sc_2O_3$ , 99.999%), gadolinium (III) oxide ( $Gd_2O_3$ , 99.995%) were purchased from Stanford Materials Corporation. Iron nitride (99.9%,  $Fe_xN$ ,  $x = 2-4$ ) was obtained from Cerac Specialty Inorganic Chemicals. Merrifield's resin (chloromethylated styrene-1% divinylbenzene copolymer, 3.5-4.5 meq of Cl/g) and sodium cyclopentadienylide (2.0 M solution in tetrahydrofuran) were obtained from Sigma-Aldrich. Sodium carbonate ( $Na_2CO_3$ , 99.9%) was purchased from Sigma-Aldrich. Solvents for extraction and chromatography were HPLC grade unless otherwise specified.

#### 3.3.2 Analytical methods

Mass spectra of endohedral metallofullerols were obtained with MALDI-TOF mass spectrometry (Shimadzu Kompact, Japan). FT-IR spectra were measured on a Perkin Elmer

Spectrum One FT-IR spectrometer using polyethylene cards (3M, USA). The XPS spectrum was recorded on a Perkin-Elmer physical electronics model 5400 spectrometer. HPLC separations were performed with an Acuflo Series III pump and Applied Biosystems 757 Absorbance Detector (detection wavelength set at 390 nm). Data was recorded on a Hitachi D-2500 Chromato-Integrator. ICP analysis was performed on a Perkin Elmer Optima 5300DV. pH measurement was performed on a Fisher scientific accument model 10 PH meter.

The relaxivities were measured at 9.4 T on a Varian Inova 400 and at 0.35 T on a TEACH SPIN PS1-B instrument.

### **3.3.3 Synthesis of TNT endohedral metallofullerols.**

#### **3.3.3.1 Synthesis of $Gd_3N@C_{80}(OH)_m(O)_n$**

The soot was prepared by arc-vaporization of graphite rods (99.9995% C, 6.15 mm x 152 mm) packed with  $Gd_2O_3$  (2.35 g, 6.5 mmol), copper powder (1.42 g, 22.4 mmol) and graphite powder (1.23 g) in a K-H generator under a dynamic  $N_2$  (20 ml/min)/ He (600ml/min) atmosphere (at 300 Torr total pressure). The graphite rods were typically baked at 1100 °C under  $N_2$  for 18 h prior to arc-vaporization. A potential difference of 32 V was applied between the ends of the rods and maintained via electronic control. After each rod had been consumed (approximately 35 min), the resultant soot was collected.

The raw soot from twelve graphite rods was collected and extracted in a Soxhlet device with toluene for 12 h. The extract solution (HPLC trace, see Figure 3.7) was applied to a glass column (40 mm x 22 cm, d x h) packed with approximately 40 g of cyclopentadiene-functionalized Merrifield resin (the synthesis of the resin will be discussed in chapter 4) in toluene. Toluene was flushed through the column at a rate of 6 mL/h during 24 h. Solid  $Gd_3N@C_{80}$  was obtained after removing the solvent from the effluent. From 12 rods, approximately 2.0 mg  $Gd_3N@C_{80}$  was obtained and the purity of  $Gd_3N@C_{80}$  was confirmed by HPLC trace (Figure 3.7).

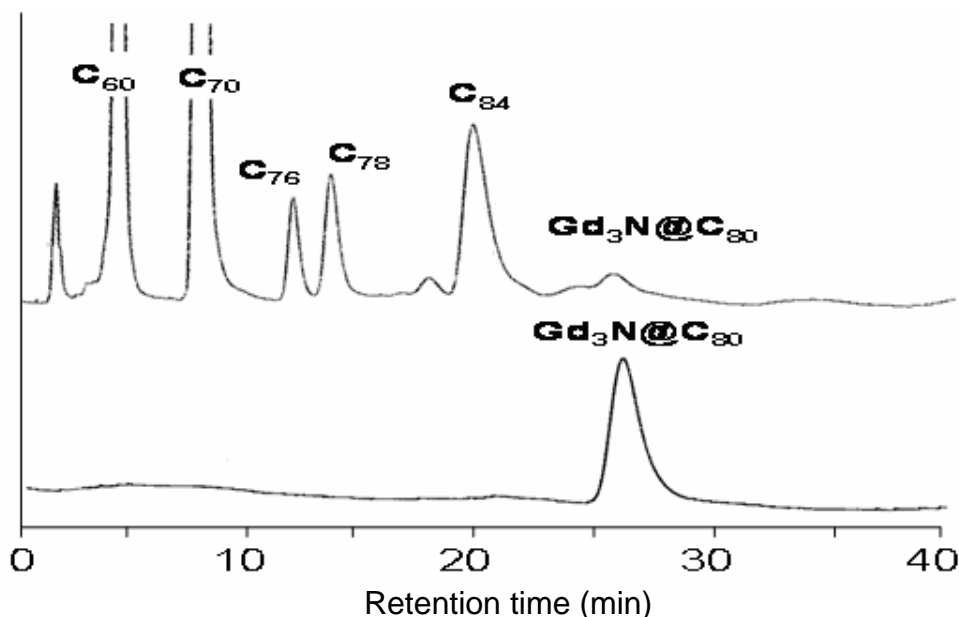


**Figure 3.7** HPLC traces of soot extract (top) and purified  $\text{Gd}_3\text{N}@C_{80}$  (bottom). HPLC conditions: pentabromobenzyloxypropyl silica (PBB) column (4.6 mm x 25 cm, Alltech Associates), toluene, 2.0 ml/min, detection at 390 nm.

A mixture of  $\text{Gd}_3\text{N}@C_{80}$  (2.0 mg, 1.38  $\mu\text{-mol}$ ) and  $\text{Na}_2\text{CO}_3$  (5.6 mg, 52  $\mu\text{-mol}$ ) was vigorously shaken in a stainless capsule with a stainless milling ball on a milling machine (SPEX mixer/mill 8000) for 14 hours. The reaction mixture was added into 30 mL toluene and the resultant solution was centrifuged to isolate the precipitate. The precipitate was dissolved in 30 mL deionized water to form a golden-colored solution. Following the previously reported procedure,<sup>82</sup> the aqueous solution was purified to produce  $\text{Gd}_3\text{N}@C_{80}(\text{OH})_m(\text{O})_n$  in a yield of approximately 35%.

### 3.3.3.2 Synthesis of $\text{Sc}_3\text{N}@C_{80}(\text{OH})_m(\text{O})_n$ and $\text{Ho}_3\text{N}@C_{80}(\text{OH})_m(\text{O})_n$

$\text{Sc}_3\text{N}@C_{80}$  was prepared from graphite rods (99.9995% C, 6.15 mm x 152 mm) packed with  $\text{Sc}_2\text{O}_3$  (0.73 g, 5.3 mmol),  $\text{Fe}_x\text{N}$  (0.40 g) and graphite powder (1.00g) and isolated from the extract as outlined above for the Gd analogue. In the similar procedure,  $\text{Sc}_3\text{N}@C_{80}(\text{OH})_m(\text{O})_n$  was synthesized under the HSVM condition in a yield of approximately 25%.  $\text{Ho}_3\text{N}@C_{80}(\text{OH})_m(\text{O})_n$  was synthesized in a yield of approximately 37% as outlined above for the Gd and Sc analogues.

### 3.3.4 Relaxivity study

#### 3.3.4.1 ICP analysis

The Gd-content of the TNT endohedral gadofullerols was measured by ICP (Perkin Elmer Optima 5300DV). The gadofullerols sample was prepared following the previously reported procedure.<sup>85</sup> First, it was treated with HNO<sub>3</sub> and carefully heated until a solid residue was obtained. This solid was dissolved in 2% HNO<sub>3</sub> and analyzed by ICP analysis. The Sc-content of Sc<sub>3</sub>N@C<sub>80</sub>(OH)<sub>m</sub>(O)<sub>n</sub> and Ho-content of Ho<sub>3</sub>N@C<sub>80</sub>(OH)<sub>m</sub>(O)<sub>n</sub> were analyzed as outline above for the Gd analogue. The metal-content in ScCl<sub>3</sub>, HoCl<sub>3</sub>, GdCl<sub>3</sub> and Ominiscan were measured directly by ICP methods without the treatment by 2% HNO<sub>3</sub>.

#### 3.3.4.2 Relaxivity measurement

The relaxivity was measured at 9.4 T on a Varian Inova 400 and at 0.35 T on a TEACH SPIN PS1-B instrument. The standard spectroscopic technique, inversion recovery, was used and relaxivities were extracted from graphs of relaxation rates versus concentration. All the data at 0.35 T was measured by Dr. Jennifer Russ.

##### 3.3.4.2.1 Gd<sub>3</sub>N@C<sub>80</sub>(OH)<sub>m</sub>(O)<sub>n</sub>

The concentration of the Gd<sub>3</sub>N@C<sub>80</sub>(OH)<sub>m</sub>(O)<sub>n</sub> in the stock solution is 0.120 mM based on ICP measurements. From the stock solution, a series of samples were prepared (solutions 1-9). Table 3.3 lists relaxivity data at high field (9.4T). As shown in Figure 3.8, the relaxivities of Gd<sub>3</sub>N@C<sub>80</sub>(OH)<sub>m</sub>(O)<sub>n</sub> are concentration dependent: there is a break in the middle between the highest four concentrations and the lowest five concentrations. The lower concentration set (0.0072 – 0.00045 mM) clearly has steeper slopes for both  $r_1$  and  $r_2$ . The  $r_1$  for the low concentration set is 29 mM<sup>-1</sup>s<sup>-1</sup>, which is approximately twice that for high concentration set. The  $r_2$  values for low and high concentrations are 110 and 45 mM<sup>-1</sup>s<sup>-1</sup>, respectively, with the low concentration value again at least twice as high.

**Table 3.3** Relaxivity data of  $\text{Gd}_3\text{N}@C_{80}(\text{OH})_m(\text{O})_n$  at high field (9.4 T).

Solution	Concentration(mM)	$r_1(\text{s}^{-1})$	$r_2(\text{s}^{-1})$
Gd-1	0.12	2.401	10.4078
Gd-2	0.06	1.4176	8.069
Gd-3	0.03	1.0277	6.5574
Gd-4	0.015	0.5907	5.6574
Gd-5	0.0072	0.5284	1.5728
Gd-6	0.0036	0.4216	1.1766
Gd-7	0.0018	0.368	0.9718
Gd-8	0.0009	0.3444	0.8834
Gd-9	0.00045	0.3304	0.8237

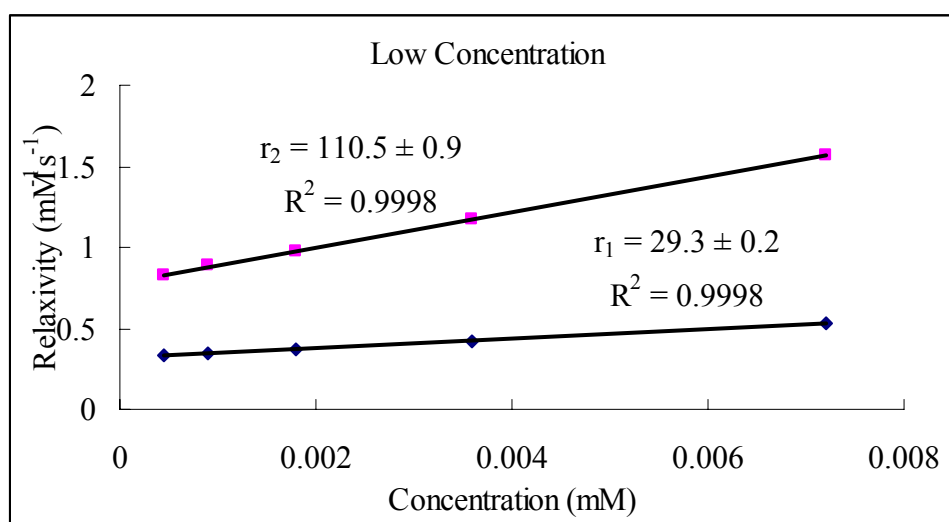
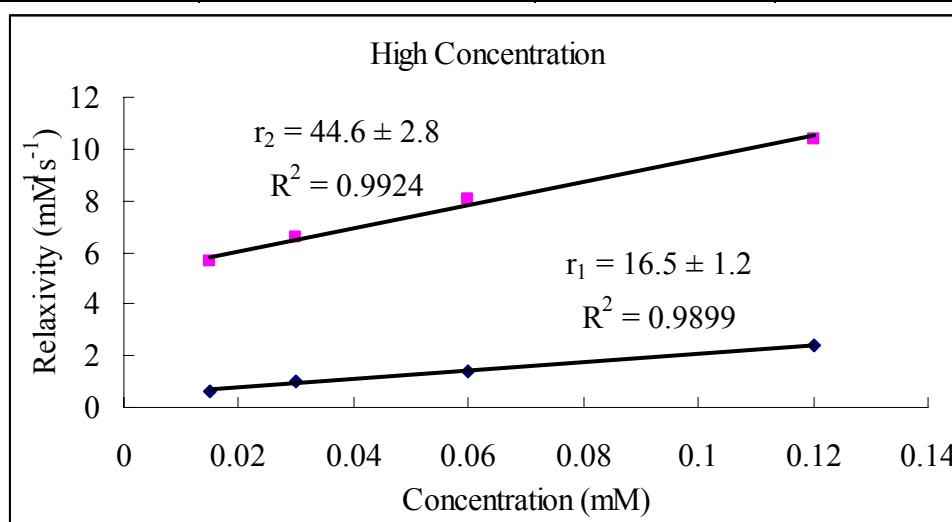


**Figure 3.8** The  $r_1$  and  $r_2$  relaxivities of  $\text{Gd}_3\text{N}@C_{80}(\text{OH})_m(\text{O})_n$  at both high (top) and low (bottom) concentration ranges at high field (9.4 T). The deep blue symbols represent  $r_1$  data while the pink ones represent  $r_2$  data.

For the pH-dependent relaxometric studies, HCl or NaOH solutions were used to adjust the pH. The pH range is 2.5-12. The relaxivities at different pH values were calculated by the equation shown below:

$$r_1 = \frac{\frac{1}{T_1} - 0.33}{C} \quad (1)$$

In the equation 1,  $T_1$  is spin-lattice relaxation time and  $C$  is the concentration of  $\text{Gd}_3\text{N}@C_{80}(\text{OH})_m(\text{O})_n$  in mM. It is assumed that the spin-lattice time of pure water is 3 seconds.

**Table 3.4** pH dependency of the  $r_1$  relaxivities for  $\text{Gd}_3\text{N}@C_{80}(\text{OH})_m(\text{O})_n$  (0.004mM) at 9.4T and room temperature.

pH	$r_1$ ( $\text{mM}^{-1}\text{s}^{-1}$ )
12.12	16.73
11.16	20.22
10.16	22.19
9.39	34.8
8.13	35.98
6.57	43.57
5.3	60.73
3.54	52.64
2.78	38.11
2.5	33.8

### 3.3.4.2.2 $\text{Ho}_3\text{N}@C_{80}(\text{OH})_m(\text{O})_n$

The ICP measurements show the concentration of the  $\text{Ho}_3\text{N}@C_{80}(\text{OH})_m(\text{O})_n$  stock solution is 0.254 mM. From the stock solution, a series of samples were prepared (solutions 1-10) (Table 3.5). Similar to gadofullerols shown above, the Ho-based TNT metallofullerols also show the concentration dependence. The  $r_1$  values at low and high concentrations are 6.8 and 1.8  $\text{mM}^{-1}\text{s}^{-1}$ , respectively, while the  $r_2$  values at low and high concentrations have smaller difference (61.9 vs 51.3  $\text{mM}^{-1}\text{s}^{-1}$ ) (Figure 3.9 and 3.10). It is worth noting that the  $r_2/r_1$  ratios of Ho-based metallofullerols at both low and high concentrations are comparatively high and will be discussed further later.

**Table 3.5** Relaxivity data of  $\text{Ho}_3\text{N}@C_{80}(\text{OH})_m(\text{O})_n$  at high field (9.4 T).

Solution	Concentration (mM)	$1/T_1$	$1/T_2$
1	0.25408	0.8403	13.22
2	0.12704	0.5692	6.5963
3	0.06352	0.4394	3.3523
4	0.03176	0.4243	1.8129
5	0.01588	0.4198	1.0043
6	0.00794	0.411	0.947
7	0.00397	0.3355	0.8272
8	0.001985	0.3556	0.597
9	0.0009925	0.3662	0.5302
10	0.00049625	0.3481	0.5112

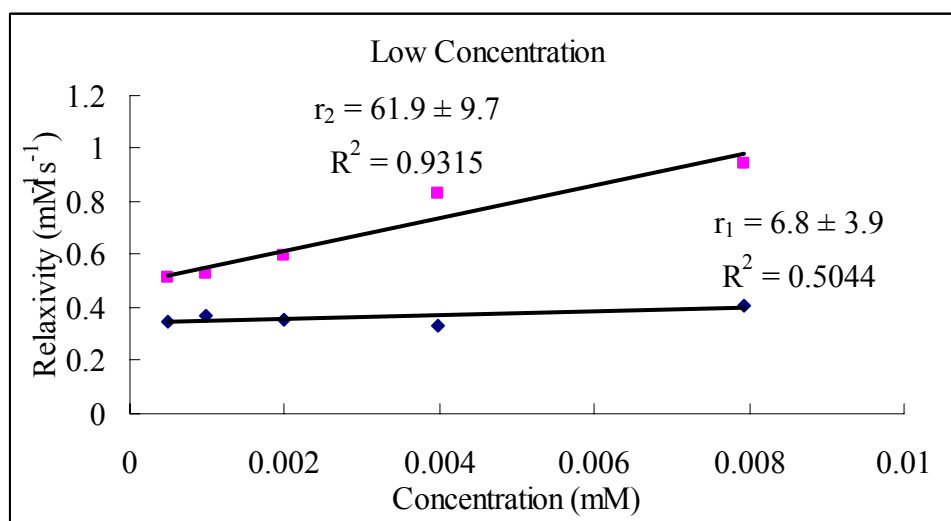


**Figure 3.9** The  $r_1$  and  $r_2$  relaxivities of  $\text{Ho}_3\text{N}@C_{80}(\text{OH})_m(\text{O})_n$  at low concentration range at high field (9.4 T). The deep blue symbols represent the  $r_1$  relaxivity data while the pink ones represent  $r_2$  relaxivity data.

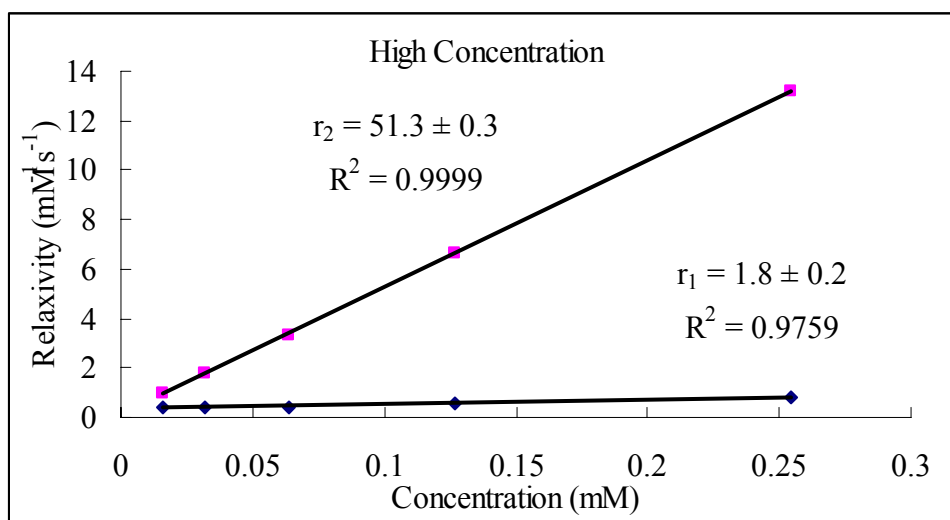


**Figure 3.10** The  $r_1$  and  $r_2$  relaxivity of  $\text{Ho}_3\text{N}@C_{80}(\text{OH})_m(\text{O})_n$  at high concentration range at high field (9.4 T). The deep blue symbols represent the  $r_1$  relaxivity data while the pink ones represent the  $r_2$  relaxivity data.

### 3.3.4.2.3 $\text{Sc}_3\text{N}@C_{80}(\text{OH})_m(\text{O})_n$

The ICP measurements show the concentration of the  $\text{Sc}_3\text{N}@C_{80}(\text{OH})_m(\text{O})_n$  stock solution is 0.1572 mM. From the stock solution, a series of samples are prepared (solutions 1-5) (Table 3.6). As shown in Figure 3.11, the  $r_1$  and  $r_2$  values for  $\text{Sc}_3\text{N}@C_{80}(\text{OH})_m(\text{O})_n$  are  $0.8 \text{ mM}^{-1}\text{s}^{-1}$  and  $3.6 \text{ mM}^{-1}\text{s}^{-1}$ , respectively at a concentration range of 0.0098-0.1572 mM. These relaxivity values are very small compared to the Gd data shown above, which proves that Sc species is a good diamagnetic control.

**Table 3.6** Relaxivity data of  $\text{Sc}_3\text{N}@C_{80}(\text{OH})_m(\text{O})_n$  at high field (9.4 T)

Solution	Concentration (mM)	$1/T_1$	$1/T_2$
Sc-1	0.1572	0.417	1.2146
Sc-2	0.0786	0.4036	1.007
Sc-3	0.0393	0.3238	0.9009
Sc-4	0.0197	0.3174	0.7246
Sc-5	0.0098	0.3052	0.6545

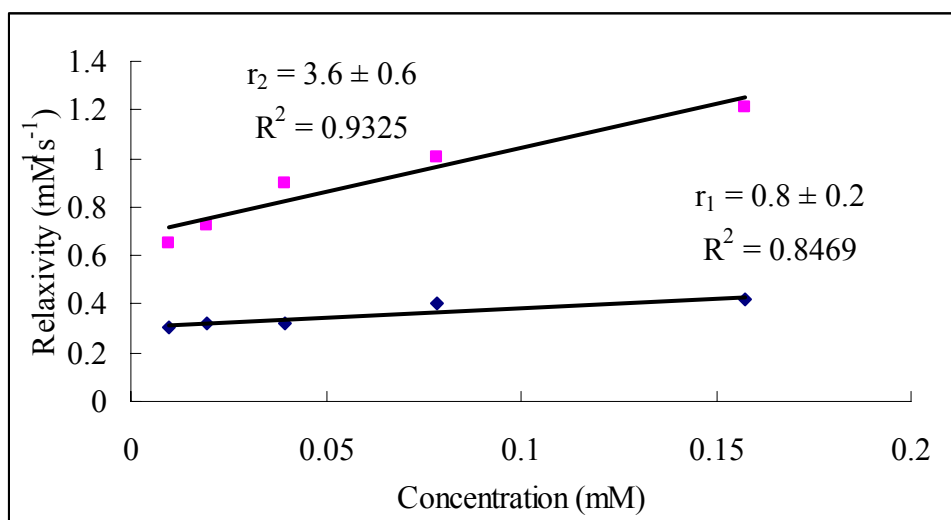


**Figure 3.11** The  $r_1$  and  $r_2$  relaxivities of  $\text{Sc}_3\text{N}@C_{80}(\text{OH})_m(\text{O})_n$  at high field (9.4 T). The deep blue symbols represent  $r_1$  data while the pink ones represent  $r_2$  data

#### 3.3.4.2.4 $\text{GdCl}_3$

The ICP measurements show the concentration of the  $\text{GdCl}_3$  stock solution is 1.08 mM. From the stock solution, a series of samples were prepared (solutions 1-5) (Table 3.7). The  $r_1$  and  $r_2$  relaxivities of  $\text{GdCl}_3$  are 3.5 and 4.8  $\text{mM}^{-1}\text{s}^{-1}$ , respectively. These relaxivities are much smaller than those of the TNT gadofullerols.

**Table 3.7** Relaxivity data of  $\text{GdCl}_3$  at high field (9.4 T)

Solution	Concentration (mM)	$1/T_1$ (s <sup>-1</sup> )	$1/T_2$ (s <sup>-1</sup> )
$\text{GdCl}_3$ -1	1.08	3.8506	5.2938
$\text{GdCl}_3$ -2	0.54	1.431	2.292
$\text{GdCl}_3$ -3	0.27	0.4531	0.9337
$\text{GdCl}_3$ -4	0.135	0.4558	1.0024
$\text{GdCl}_3$ -5	0.0675	0.4212	/

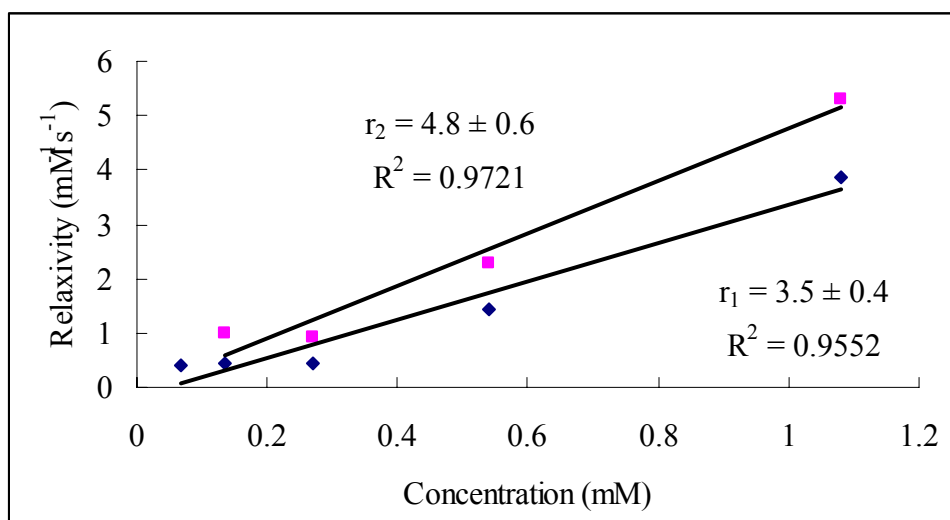


**Figure 3.12** The  $r_1$  and  $r_2$  relaxivities of  $\text{GdCl}_3$  at high field (9.4 T). The deep blue symbols represent  $r_1$  data while the pink ones represent  $r_2$  data.

### 3.3.4.2.5 $\text{HoCl}_3$

The ICP measurement shows the concentration of the  $\text{HoCl}_3$  stock solution is 0.7623 mM. From the stock solution, a series of samples were prepared (solutions 1-5) (Table 3.8). The  $r_1$  and  $r_2$  relaxivities of  $\text{HoCl}_3$  are 0.9 and 1.0  $\text{mM}^{-1}\text{s}^{-1}$ , respectively. These relaxivities are much smaller than those of the TNT Ho-based metallofullerols. It is also worth noting that the  $r_2/r_1$  ratio of  $\text{HoCl}_3$  is approximately 1.1, which is significantly smaller than that of Ho-based metallofullerols.

**Table 3.8** Relaxivity data of  $\text{HoCl}_3$  at high field (9.4 T)

solution	Concentration (mM)	$1/T_1$	$1/T_2$
$\text{HoCl}_3$ -1	0.7623	1.1079	0.9737
$\text{HoCl}_3$ -2	0.3811	0.5362	0.5066
$\text{HoCl}_3$ -3	0.1906	0.5043	0.3967
$\text{HoCl}_3$ -4	0.0953	0.3861	0.3365
$\text{HoCl}_3$ -5	0.0476	0.3123	0.3333

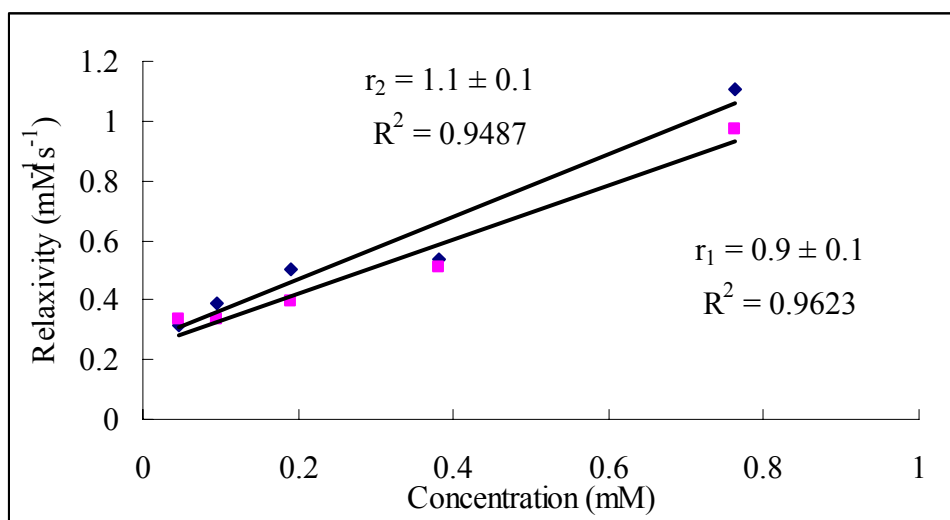


**Figure 3.13** The  $r_1$  and  $r_2$  relaxivities of  $\text{HoCl}_3$  at high field (9.4 T). The deep blue symbols represent  $r_1$  data while the pink ones represent  $r_2$  data.

### 3.3.4.2.6 Ominiscan

The ICP measurements show the concentration of the Ominiscan stock solution is 5.00 mM. From the stock solution, a series of samples were prepared (solutions 1-5) (Table 3.9). The  $r_1$  and  $r_2$  relaxivities of Ominiscan are 4.0 and 4.2  $\text{mM}^{-1}\text{s}^{-1}$ , respectively. These relaxivities are much smaller than those of the TNT gadofullerols.

**Table 3.9** Relaxivity data of Ominiscan at high field (9.4 T)

Solution	Concentration (mM)	$1/T_1$ (9.4T)	$1/T_2$ (9.4T)
Omniscan 1	5.00	21.4915	19.8926
Omniscan 2	2.50	12.0613	10.9745
Omniscan 3	1.00	5.2301	4.2717
Omniscan 4	0.50	2.6511	2.1492
Omniscan 5	0.25	1.4067	1.0757

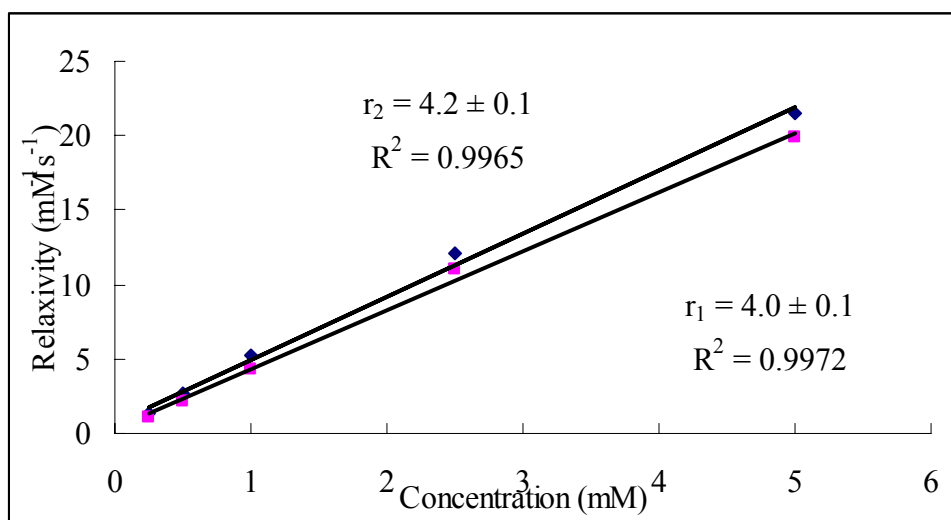


**Figure 3.13** The  $r_1$  and  $r_2$  relaxivities of Ominiscan at high field (9.4 T). The deep blue symbols represent  $r_1$  data while the pink ones represent  $r_2$  data.

### 3.3.4.2.7 Summary of relaxivity data

$Gd_3N@C_{80}(OH)_m(O)_n$				
	High Field (9.4T)		Low Field (0.35T)	
	$r_1$	$r_2$	$r_1$	$r_2$
High Concentration range	$16.5 \pm 1.2$	$44.6 \pm 2.8$	$29 \pm 1$	$52 \pm 4$
	$r_2/r_1 = 2.6$		$r_2/r_1 = 1.8$	
Low Concentration range	$29.3 \pm 0.2$	$110.5 \pm 0.9$	$72 \pm 1$	$143 \pm 15$
	$r_2/r_1 = 3.8$		$r_2/r_1 = 2.0$	
Ominiscan				
High Concentration range	$4.0 \pm 0.1$	$4.2 \pm 0.1$	$5.7 \pm 0.1$	$4.3 \pm 0.1$
	$r_2/r_1 = 1.0$		$r_2/r_1 = 1.3$	
Low Concentration range	N/A	N/A	N/A	N/A
$GdCl_3$				
High Concentration range	$3.5 \pm 0.4$	$4.8 \pm 0.6$	$4.7 \pm 0.4$	$5.4 \pm 0.9$
	$r_2/r_1 = 1.4$		$r_2/r_1 = 1.2$	
Low Concentration range	N/A	N/A	N/A	N/A
$Ho_3N@C_{80}(OH)_m(O)_n$				
	High Field (9.4T)		Low Field (0.35T)	
	$r_1$	$r_2$	$r_1$	$r_2$
High Concentration range	$1.8 \pm 0.2$	$51.3 \pm 0.3$	$0.3 \pm 0.1$	$12.3 \pm 0.1$
	$r_2/r_1 = 28.5$		$r_2/r_1 = 41$	
Low Concentration range	$6.8 \pm 3.9$	$61.9 \pm 9.7$	$1.1 \pm 2.3$	$22 \pm 4$
	$r_2/r_1 = 9.1$		$r_2/r_1 = 20$	
$HoCl_3$				
High Concentration range	$0.9 \pm 0.1$	$1.1 \pm 0.1$	$0.39 \pm 0.05$	$1.7 \pm 0.1$
	$r_2/r_1 = 1.1$		$r_2/r_1 = 4.3$	
Low Concentration range	N/A	N/A	N/A	N/A
$Sc_3N@C_{80}(OH)_m(O)_n$				
	High Field (9.4T)		Low Field (0.35T)	
	$r_1$	$r_2$	$r_1$	$r_2$
High Concentration range	$0.8 \pm 0.2$	$3.6 \pm 0.6$	$1.4 \pm 0.2$	$5.2 \pm 0.2$
	$r_2/r_1 = 5.0$		$r_2/r_1 = 3.7$	
Low Concentration range	N/A	N/A	N/A	N/A

# Chapter 4 - Synthesis, Isolation and Characterization of CeSc<sub>2</sub>N@C<sub>80</sub> and Crystallographic Study of the D<sub>5h</sub> Isomer of Sc<sub>3</sub>N@C<sub>80</sub>

## 4.1 Introduction

Since the beginning of fullerene chemistry, metal-containing endohedral fullerenes have attracted particular interest since the encapsulated metal atoms can impart unusual physical and chemical properties.<sup>20, 82,106,107,108,109</sup> Also, the metal can readily donate charge to the cage which in certain cases stabilizes reactive empty cage fullerenes, such as the IPR-obeying C<sub>74</sub> (IPR = isolated pentagon rule) and the non-IPR obeying C<sub>66</sub> and C<sub>68</sub> cages.<sup>6,11,110</sup> However, progress in exploring the structures and properties of endohedral metallofullerenes (EMFs) has been hampered by their low production yields and purification difficulties. Nevertheless, in the past two decades, scandium, cerium, praseodymium, terbium, gadolinium, neodymium, lanthanum, erbium, holmium, dysprosium, lutetium, thulium, samarium, europium and ytterbium have been encapsulated to yield a mono- or dimetallofullerene species via the Krätschmer-Huffman electric-arc process.<sup>110,111,112,113,114,115,116,117,118,119</sup> In 1996, the cerium mono-metallofullerene and di-metallofullerene, Ce@C<sub>82</sub> and Ce<sub>2</sub>@C<sub>80</sub>, were synthesized by Yang and co-workers.<sup>117</sup> Recently, the magnetic properties of Ce@C<sub>82</sub> have been investigated by examining the magnetic field-induced changes in the magnetic susceptibility of Ce@C<sub>82</sub>.<sup>120</sup> The magnetic anisotropy of cerium endohedral metallofullerenes is believed to be associated with the off-center geometry of the Ce<sup>3+</sup> ion in the cage.<sup>121</sup>

In 1999, Dorn et al.<sup>5</sup> reported the synthesis and characterization of novel trimetallic nitride template (TNT) endohedral metallofullerenes in the high yields, by introducing nitrogen gas into the Krätschmer-Huffman generator. Since this discovery, many new members of this interesting family, e.g., A<sub>3</sub>N@C<sub>80</sub> (A = Er,<sup>5</sup> Gd,<sup>97-98</sup> Ho,<sup>122</sup> Tb,<sup>123</sup> Dy,<sup>124</sup> Tm,<sup>125</sup> Lu,<sup>87</sup> Y<sup>20</sup>), have been reported with the nitrogen atom located at the geometric center of the molecule. For example, the most common trimetallic nitride, Sc<sub>3</sub>N@C<sub>80</sub>, can be formally viewed as a

positively charged planar tetra-atom cluster inside a negatively charged icosahedral ( $I_h$ ) carbon cage,  $[\text{Sc}_3\text{N}]^{+6}@\text{C}_{80}^{-6}$ .<sup>126-127</sup> Each scandium atom transfers one electron to the nitrogen atom and two electrons to the carbon cage which forms a stabilized closed-shell electronic structure  $[\text{C}_{80}]^{-6}$ . In contrast to the homonuclear  $\text{A}_3\text{N}$  cluster, there is a paucity of mixed metal cluster cases ( $\text{AB}_2\text{N}$ ) reported to date. A notable exception is  $\text{ErSc}_2\text{N}@\text{C}_{80}$  which has been characterized by a single-crystal X-ray diffraction study.<sup>128</sup> Another series of mixed-metal species of TNT-EMFs,  $\text{Lu}_{3-x}\text{A}_x\text{N}@\text{C}_{80}$  ( $x = 1, 2$ ;  $\text{A} = \text{Ho}, \text{Gd}$ ) were prepared in 2002,<sup>87</sup> but these have not been isolated and characterized. With the exceptions noted above, most mixed-metal ( $\text{AB}_2\text{N}$ ) based TNT-EMF have not been isolated in pure form because of difficulties in the separation and purification process.

In an earlier  $^{13}\text{C}$  NMR study, the existence of a second isomer of  $\text{Sc}_3\text{N}@\text{C}_{80}$  ( $\text{D}_{5h}$ ) was established in the mixture of  $I_h$  and  $\text{D}_{5h}$  isomers.<sup>18</sup> Recently, Dunsch et al.<sup>129</sup> successfully isolated the  $\text{Sc}_3\text{N}@\text{C}_{80}$   $\text{D}_{5h}$  isomer from the  $I_h$  isomer and characterized the  $\text{D}_{5h}$  isomer with FT-IR, UV-Vis-NIR spectra. Other examples of  $\text{D}_{5h}$  isomers have been reported for  $\text{Dy}_3\text{N}@\text{C}_{80}$ <sup>124</sup> and  $\text{Tm}_3\text{N}@\text{C}_{80}$ <sup>125</sup> and a third isomer of  $\text{Dy}_3\text{N}@\text{C}_{80}$  has been observed.<sup>130</sup> However, the  $\text{D}_{5h}$  cage symmetry has not been confirmed yet. The X-ray crystallographic study is of great importance to determine the cage structure and explore the reactivity of these  $\text{D}_{5h}$  isomers.

In this chapter, the synthesis, structure, and characterization of  $\text{CeSc}_2\text{N}@\text{C}_{80}$  will be reported. Also the  $\text{D}_{5h}$  isomer of  $\text{Sc}_3\text{N}@\text{C}_{80}$  was isolated and characterized with X-ray single-crystal diffraction study.

## 4.2 Results and discussions

### 4.2.1 CeSc<sub>2</sub>N@C<sub>80</sub>

#### 4.2.1.1 Synthesis of the Ce<sub>x</sub>Sc<sub>3-x</sub>N@C<sub>80</sub> (x=0, 1) Family and Isolation of CeSc<sub>2</sub>N@C<sub>80</sub>

The vaporization of graphite rods packed with a mixture of Sc<sub>2</sub>O<sub>3</sub>, CeO<sub>2</sub>, Fe<sub>x</sub>N (x = 2-4) and graphite powder was conducted in a Krätschmer-Huffman fullerene generator under a dynamic flow of helium and nitrogen gas, producing a black soot as shown in Figure 4.1 and described in the Experimental Section. In contrast with the earlier reported Er<sub>x</sub>Sc<sub>3-x</sub>N@C<sub>80</sub> (x=0-3) family, no significant peaks corresponding to Ce<sub>2</sub>ScN@C<sub>80</sub> and Ce<sub>3</sub>N@C<sub>80</sub> were observed in the NI-DCI mass spectrum (see Experimental section). This is uprobably related to the greater lanthanide ion contraction for an erbium ion relative to a cerium ion (ionic radii: Er<sup>3+</sup>, 103 pm vs Ce<sup>3+</sup>, 115 pm).<sup>131</sup> Recently, we reported a new purification protocol to obtain pure TNT EMFs, A<sub>3</sub>N@C<sub>80</sub> (A = lanthanide atom) directly from crude soots in a single, facile step based on the greater kinetic stability of the TNT EMFs relative to empty-cage fullerenes and classic EMFs, such as A<sub>x</sub>@C<sub>2y</sub> (x=1-3, y=30-50).<sup>23</sup> Utilizing this method, the CeSc<sub>2</sub>N@C<sub>80</sub> sample was isolated from the mixture. Final purification involved a two stage, high-performance liquid chromatographic (HPLC) separation with the final HPLC trace and NI-DCI mass spectrum shown in Figure 4.2a.

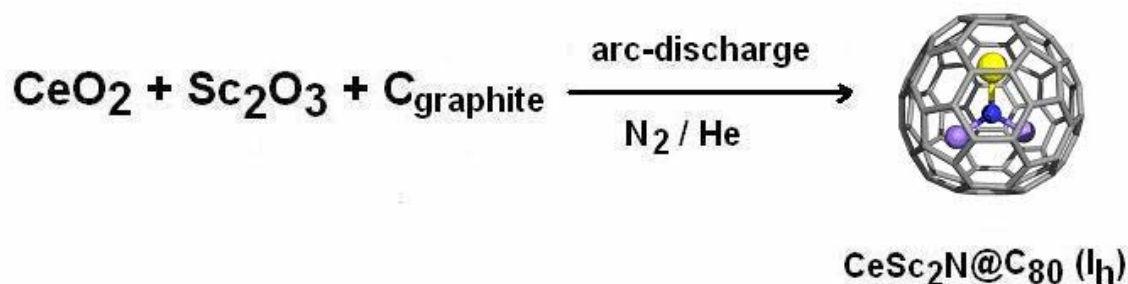


**Figure 4.1** Preparation of CeSc<sub>2</sub>N@C<sub>80</sub>.

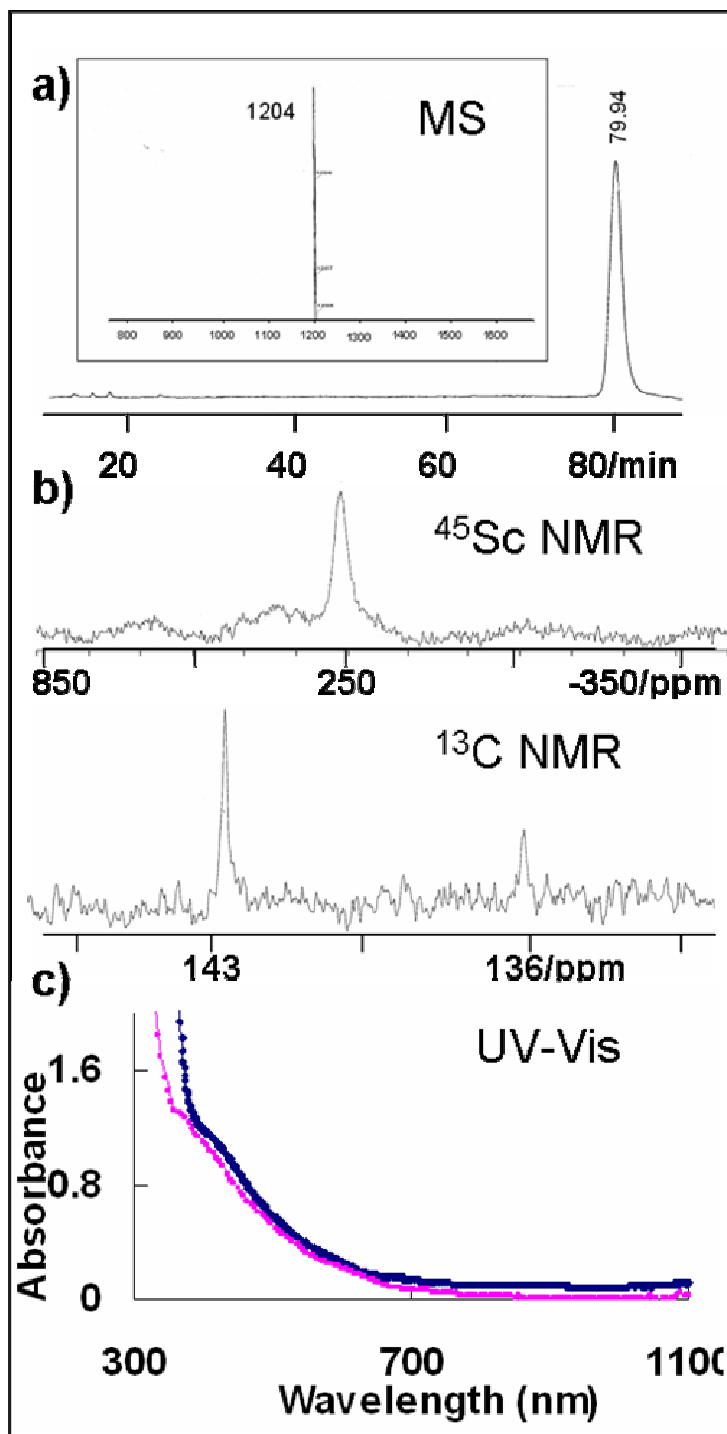


**Figure 4.2a.** The HPLC chromatogram for the purified sample of  $\text{CeSc}_2\text{N}@C_{80}$  (5PYE column 10 x 250 mm, toluene as eluent at a flow rate of 1.0 mL/min) and the inserted NI-DCI mass spectrum of this sample. **2b.** 121.5 MHz  $^{45}\text{Sc}$  NMR spectrum of  $\text{CeSc}_2\text{N}@C_{80}$  in 1,2-dichlorobenzene (25°C, 140,000 scans) and 125 MHz  $^{13}\text{C}$  NMR spectrum of  $\text{CeSc}_2\text{N}@C_{80}$  in  $\text{CS}_2/\text{acetone-d}_6$  (v/v 9:1) (25°C,  $\text{Cr}(\text{acac})_3$  added, 21,000 scans). **2c.** Comparison of the UV-VIS absorption spectra of  $\text{CeSc}_2\text{N}@C_{80}$  (deep blue) and  $\text{Sc}_3\text{N}@C_{80}(\text{I}_h)$  (pink) in toluene.

#### 4.2.1.2 Electronic Structure of CeSc<sub>2</sub>N@C<sub>80</sub>

A comparison of the UV-Visible absorption spectra for CeSc<sub>2</sub>N@C<sub>80</sub> and Sc<sub>3</sub>N@C<sub>80</sub> metallofullerenes is illustrated in Figure 4.2c. Both molecules show similar absorption spectra. The CeSc<sub>2</sub>N@C<sub>80</sub> UV-Visible spectrum is similar to Ce<sub>2</sub>@C<sub>80</sub>,<sup>117b</sup> which also exhibits a monotonically decreasing absorption coefficient with increasing wavelength without well-defined sharp spectral features. Generally, the UV-Vis spectrum of a metallofullerene depends on the cage structure (size and symmetry) as well as the charge on the cage. The similarities of these UV-vis spectra suggest that Sc<sub>3</sub>N@C<sub>80</sub> and CeSc<sub>2</sub>N@C<sub>80</sub> possess the same cluster charge transfer and I<sub>h</sub> cage structure. These results, together with the <sup>13</sup>C NMR and XPS data described below suggest that CeSc<sub>2</sub>N@C<sub>80</sub> can be formally represented by [CeSc<sub>2</sub>N]<sup>+6</sup>@[C<sub>80</sub>]<sup>-6</sup> which is similar to the formal charges found for Sc<sub>3</sub>N@C<sub>80</sub><sup>5</sup> and Ce<sub>2</sub>@C<sub>80</sub>.<sup>117b</sup>

The XPS binding energies for the Ce 3d core levels of CeSc<sub>2</sub>N@C<sub>80</sub> are shown in Figure 4.3. The Ce region of the spectrum is quite similar to those of Ce@C<sub>82</sub> and Ce<sub>2</sub>@C<sub>80</sub> with the two prominent features for the 3d<sub>3/2</sub> and 3d<sub>5/2</sub> levels. The binding energy of these two peaks (886.0 eV for 3d<sub>5/2</sub> and 904.6 eV for 3d<sub>3/2</sub>) indicates the absence of Ce<sup>4+</sup> in CeSc<sub>2</sub>N@C<sub>80</sub>, since Ce<sup>4+</sup> has a characteristic 3d peak at a binding energy of approximately 914 eV arising from a transition from the initial state 3d<sup>10</sup>4f<sup>0</sup> to the final state 3d<sup>9</sup>4f<sup>0</sup>.<sup>117b</sup> Furthermore, the location and shape of the Ce (3d) peaks in the XPS spectrum of CeSc<sub>2</sub>N@C<sub>80</sub> are quite similar to those of cerium trihalides,<sup>132</sup> suggesting that the Ce atom encaged in C<sub>80</sub> is in the form of a Ce<sup>3+</sup> ion. The carbon and nitrogen binding energies are also consistent with those found for Sc<sub>3</sub>N@C<sub>80</sub> and are illustrated in the Experimental section.

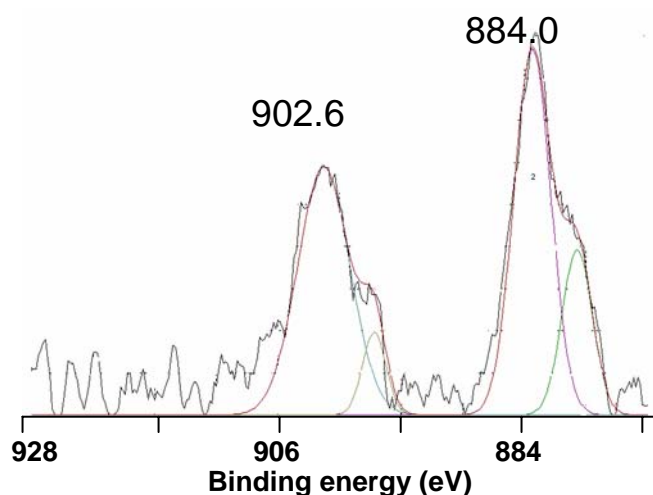


**Figure 4.3.** XPS spectrum of CeSc<sub>2</sub>N@C<sub>80</sub> on a gold foil in the core level region of Ce (3d). The colored lines are fitting curves of the spectral peaks.

#### 4.2.1.3 NMR Studies of CeSc<sub>2</sub>N@C<sub>80</sub>

The ambient temperature <sup>45</sup>Sc and <sup>13</sup>C NMR spectra are shown in Figures 4.2b, respectively, and related data are given in Table 4.1. The <sup>13</sup>C NMR spectrum of CeSc<sub>2</sub>N@C<sub>80</sub> consists of two sharp signals in a 3/1 intensity ratio and is similar to those of Sc<sub>3</sub>N@C<sub>80</sub> (I<sub>h</sub> isomer),<sup>5</sup> Lu<sub>3</sub>N@C<sub>80</sub> (I<sub>h</sub> isomer)<sup>87</sup> and Ce<sub>2</sub>@C<sub>80</sub>.<sup>133</sup> It is surprising that at ambient temperature the C<sub>80</sub> carbon atoms remain isotropically motionally averaged yielding only two unique resonances even with the CeSc<sub>2</sub>N acentric top inside. These data and the <sup>45</sup>Sc NMR data below suggest a relatively small energy barrier for rotation of the CeSc<sub>2</sub>N cluster inside the carbon cage. The buried f electron spin of the Ce<sup>3+</sup> (4f<sup>1</sup>5d<sup>0</sup>) ion produces only relatively minor effects on the <sup>13</sup>C NMR spectrum. For example, the only chemical shift difference between CeSc<sub>2</sub>N@C<sub>80</sub> and Sc<sub>3</sub>N@C<sub>80</sub> is a subtle upfield shift of approximately 1.5 ppm for both of the <sup>13</sup>C signals of CeSc<sub>2</sub>N@C<sub>80</sub>. In contrast, a somewhat larger <sup>13</sup>C NMR shift range was reported for Ce<sub>2</sub>@C<sub>80</sub> which utilizes the same icosahedral cage C<sub>80</sub><sup>6-</sup>, but contains two encapsulated Ce<sup>3+</sup> ions.<sup>133</sup>

**Table 4.1** Comparison of Chemical Shifts in  $^{13}\text{C}$  NMR Spectra of Several Endohedral Metallofullerenes.

Metallofullerene	$^{13}\text{C}$ NMR Chemical shifts (ppm)	
	$\text{Sc}_3\text{N}@C_{80}(\text{I}_h)^5$	144.57
$\text{Lu}_3\text{N}@C_{80}(\text{I}_h)^{87}$	144.0	137.4
$\text{CeSc}_2\text{N}@C_{80}$	142.85	135.90
$\text{Ce}_2@C_{80}^{133}$	148.6	124.7

The dynamic behavior of the Sc atoms encapsulated in carbon cages is conveniently monitored by  $^{45}\text{Sc}$  NMR. In similar fashion to the data reported for the  $\text{Sc}_2@C_{84}$  isomer (III)<sup>134</sup> and  $\text{Sc}_3\text{N}@C_{80}(\text{I}_h)$ ,<sup>5</sup> the  $^{45}\text{Sc}$  NMR spectrum for  $\text{CeSc}_2\text{N}@C_{80}$  (Figure 4.2b) exhibits a single, symmetric peak at room temperature. Furthermore, when the temperature is raised from 313K to 383K, the  $^{45}\text{Sc}$  NMR linewidth decreases from  $\sim 2700$  Hz to  $\sim 1370$  Hz (Figure 4.4). These results suggest that the internal motion provides the same average electronic environment for the two Sc atoms in the  $\text{CeSc}_2\text{N}$  cluster. With the assumption that the correlation time can be expressed by  $\zeta_c = \zeta_0 \exp(E_a/kT)$ , where  $\zeta_0$  is a constant and  $E_a$  represents a rotation energy barrier, the linewidths at different temperatures can be plotted to yield activation energy,  $E_a = 79 \pm 6$  meV for the rotation energy barrier of  $\text{CeSc}_2\text{N}@C_{80}$  in 1, 2-dichlorobenzene. This energy barrier is the same as that of  $\text{Sc}_3\text{N}@C_{80} \text{I}_h$  isomer ( $75 \pm 8$  meV in 1, 2-dichlorobenzene, see Chapter 5) within the experimental error. However, it should be noted that this energy barrier is modulated by not only the internal motion of the endohedral cluster, but also the overall rotational motion of the carbon cage.

The  $^{45}\text{Sc}$  NMR chemical shift ( $\delta$ ) of  $\text{CeSc}_2\text{N}@C_{80}$  exhibits a Curie temperature dependent upfield chemical shift that probably originates from the buried f electron spin remaining on the  $\text{Ce}^{3+}$  ( $4f^1 5d^0$ ) ion. As illustrated in Figure 4.4, a temperature increase from 313K to 383K, yields a upfield shift in the resonance frequency of the  $^{45}\text{Sc}$  signal from approximately 257.3 to 235.7 ppm (relative to external  $\text{ScCl}_3$ ). As shown in the equation below, the chemical shifts of

paramagnetic molecules in solution are generally composed of three contributions from diamagnetic ( $\delta_{\text{dia}}$ ), Fermi contact ( $\delta_{\text{fc}}$ ) and pseudocontact ( $\delta_{\text{pc}}$ ) shifts.<sup>135</sup>

$$\delta = \delta_{\text{dia}} + \delta_{\text{fc}} + \delta_{\text{pc}} \quad (4.1)$$

The paramagnetic term  $\delta_{\text{fc}}$  is proportional to  $T^{-1}$ , while  $\delta_{\text{pc}}$  is proportional to  $T^{-2}$  ( $T$  = absolute temperature). Since the diamagnetic model molecule,  $[\text{CeSc}_2\text{N@C}_{80}]^+$  was not available, the chemical shift of  $\text{Sc}_3\text{N@C}_{80}$  was employed as the value of  $\delta_{\text{dia}}$  in this case. The line-fitting plots of  $\delta$  vs  $T^{-1}$  (see Figure 4.13 in Experimental section) showed the extrapolated values at  $T^{-1} = 0$ , 134.6 ppm, is quite different from the observed scandium chemical shift of 196.4 ppm for  $\text{Sc}_3\text{N@C}_{80}$ ,<sup>5</sup> while the value extrapolated by the line-fitting plot with  $T^{-2}$  (see Figure 4.14 in Experimental section) at  $T^{-2} = 0$ , 189.9 ppm is in reasonable agreement with the observed scandium shift of  $\text{Sc}_3\text{N@C}_{80}$ . Assuming our diamagnetic reference is appropriate, these results suggest that the pseudocontact ( $\delta_{\text{pc}}$ ) term dominates the chemical shift in a similar fashion to the situation reported for  $\text{Ce@C}_{82}$ .<sup>136</sup> A dominant Fermi contact interaction is also less likely, because it would only be possible via spin polarization transfer from Ce to the Sc nucleus through the Ce-N and N-Sc bonds.

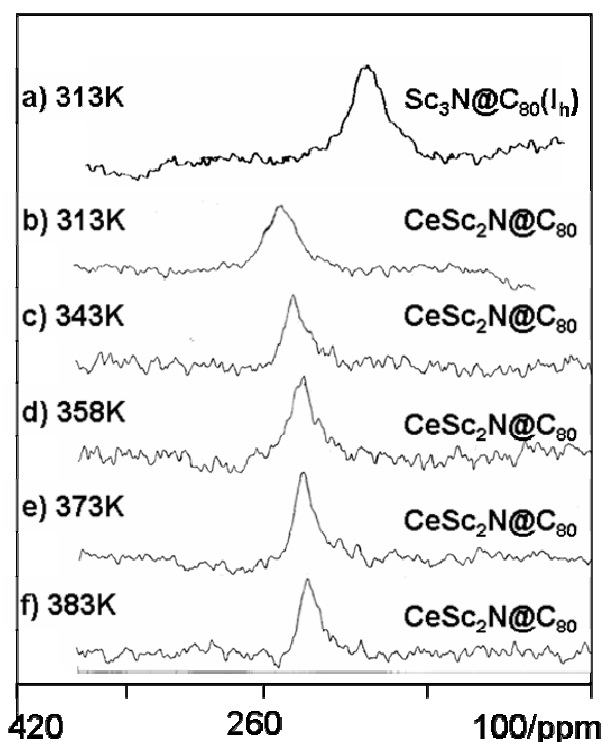


**Figure 4.4.** 97.2 MHz  $^{45}\text{Sc}$  solution NMR spectra of  $\text{CeSc}_2\text{N@C}_{80}$  in 1,2-dichlorobenzene (b-f) at various temperatures and  $\text{Sc}_3\text{N@C}_{80}$  ( $I_h$ ) in 1,2-dichlorobenzene (a) at 313K.

#### 4.2.1.4 The Structure of CeSc<sub>2</sub>N@C<sub>80</sub> as Determined by Single Crystal X-ray Diffraction

As previously shown,<sup>5, 7, 128, 137, 138, 139</sup> co-crystallization of endohedral fullerenes with M<sup>II</sup>(OEP) (M = Ni, Co; OEP is the dianion of octaethylporphyrin) is a useful method to obtain diffraction quality crystals since most endohedral metallofullerenes themselves do not readily crystallize in an ordered fashion. Suitable crystals were formed by diffusion of a benzene solution of Ni<sup>II</sup>(OEP) into a solution of CeSc<sub>2</sub>N@C<sub>80</sub> in benzene over a two-week period. Black crystals with the composition CeSc<sub>2</sub>N@C<sub>80</sub>•Ni<sup>II</sup>(OEP)•2C<sub>6</sub>H<sub>6</sub> were obtained and characterized by X-ray diffraction. Figure 4.5 shows a drawing of the endohedral and its relationship to the porphyrin. Both of these molecules reside in general positions and have no crystallographically imposed symmetry. In addition there is a molecule of benzene in a general position and two others at half occupancy, each located on a two-fold axis.

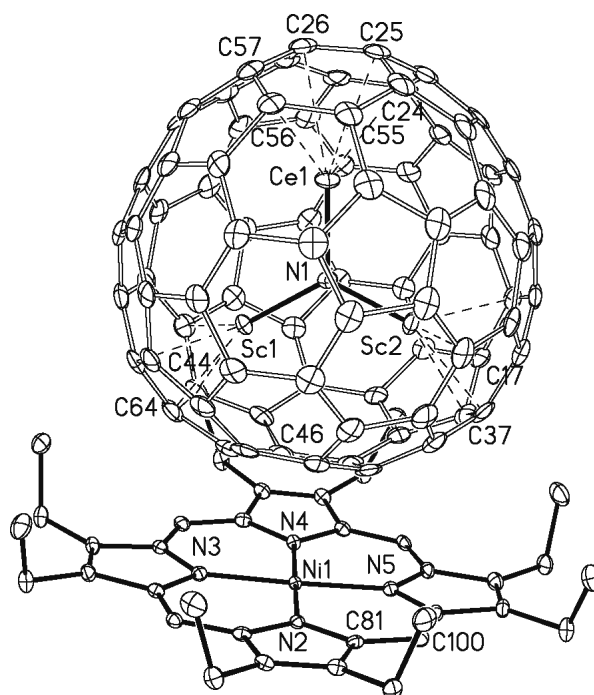


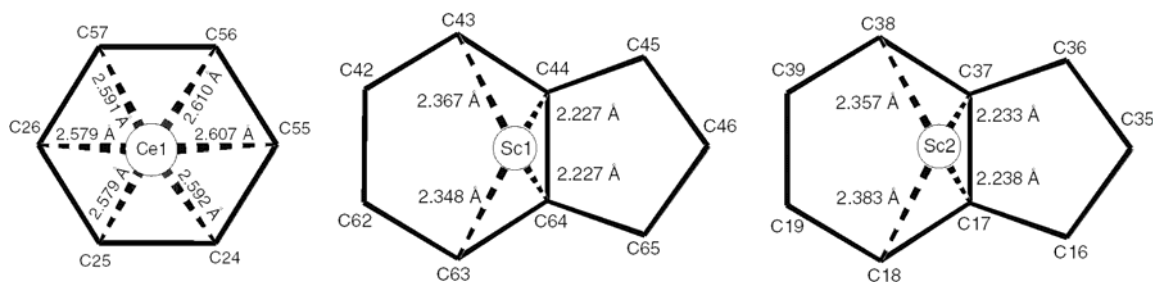
**Figure 4.5** A perspective view of the relative orientations of CeSc<sub>2</sub>N@C<sub>80</sub> and Ni<sup>II</sup>(OEP) within crystalline CeSc<sub>2</sub>N@C<sub>80</sub>•Ni<sup>II</sup>(OEP)•2C<sub>6</sub>H<sub>6</sub>. Thermal ellipsoids are shown at the 50 % level.

Endohedral metallofullerenes that are co-crystallized with metalloporphyrins can show some degree of disorder in either the cage orientation, in the location of the metal ions inside the cage, or both.<sup>5, 7, 128, 137, 138, 139, 140</sup> However, in CeSc<sub>2</sub>N@C<sub>80</sub>•Ni<sup>II</sup>(OEP)•2C<sub>6</sub>H<sub>6</sub>, the fullerene

cage and the CeSc<sub>2</sub>N unit are both *fully ordered*. The C<sub>80</sub> unit has the I<sub>h</sub> isomeric structure, which is generally the more abundant of the two cage isomers (I<sub>h</sub> and D<sub>5h</sub>) so far observed in C<sub>80</sub>-containing endohedrals. Inside the cage, the two scandium ions are situated in close proximity to the metalloporphyrin, while the cerium ion is located on the far side of the cage. The Sc2-N-Sc1 angle is 116.87(12)° and Sc2-N-Ce and Sc1-N-Ce angles are 121.67(11) and 121.45(11)°, respectively. The CeSc<sub>2</sub>N unit is strictly planar, since the sum of these three angles about the central nitrogen is 359.99°. Previous studies have shown that the trimetallic nitride cluster is planar in the cases of Sc<sub>3</sub>N@C<sub>80</sub>, ErSc<sub>2</sub>N@C<sub>80</sub>, Sc<sub>3</sub>N@C<sub>78</sub>, Sc<sub>3</sub>N@C<sub>68</sub>, and Lu<sub>3</sub>N@C<sub>80</sub>, although the cage sizes and geometries vary significantly in these TNT endohedral fullerenes. In contrast, due to the large size of Gd(III), the Gd<sub>3</sub>N unit in Gd<sub>3</sub>N@C<sub>80</sub>, is pyramidal with the nitrogen atom displaced by 0.522(8) Å from the plane of the three gadolinium ions.<sup>97</sup>

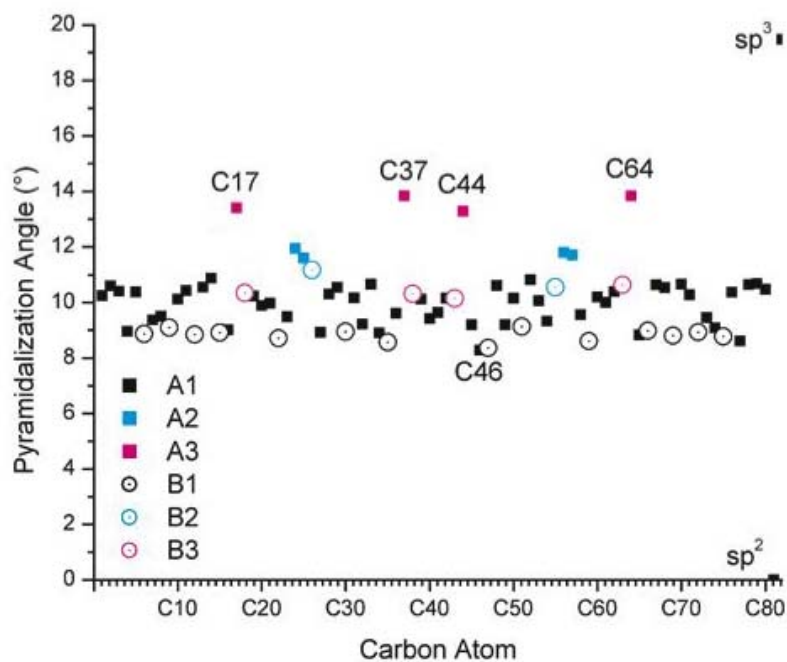
As expected on the basis of ionic radii, the Ce-N distance, 2.184(2) Å, in CeSc<sub>2</sub>N@C<sub>80</sub> is considerably longer than the Sc1-N and Sc2-N distances, 1.942(2) and 1.933(2) Å, respectively. For comparison the Sc-N distances are longer in related endohedrals: 1.9931(14), 2.0323(16), and 2.0526(14) Å in the I<sub>h</sub> isomer of Sc<sub>3</sub>N@C<sub>80</sub>, 1.988(7), 1.983(15), and 2.125(5) in Sc<sub>3</sub>N@C<sub>78</sub>,<sup>7</sup> and 1.961(4), 1.974(4), and 2.022(3) in Sc<sub>3</sub>N@C<sub>68</sub>.<sup>139</sup> Interestingly, the cage size is reduced in the latter two endohedrals yet the Sc-N distances are still longer than those in CeSc<sub>2</sub>N@C<sub>80</sub> where the large cerium ion compresses the two Sc-N bonds. Also it is worth noting that in ErSc<sub>2</sub>N@C<sub>80</sub> the Sc-N distance, 1.968(6) Å, is longer than the Sc-N distances in CeSc<sub>2</sub>N@C<sub>80</sub>, while the Er-N distance, 2.089(9) Å, is shorter than the Ce-N distance. The large size of the cerium ion also pushes N1 0.36 Å away from the center of the C<sub>80</sub> cage and toward the two scandium ions.

Figure 4.6 shows the locations of the metal ions relative to the cage. The figure consists of projections of the metal ions onto the least squares planes of the carbon atoms as viewed from the inside of the cage. The cerium ion is positioned above the center of a hexagon. In contrast the scandium ions are located near 6:5 ring junctions with a displacement toward the hexagon. The metal ion placement differs from that seen in ErSc<sub>2</sub>N@C<sub>80</sub> where all the metal ions lie over carbon atoms at the intersection of two hexagons and one pentagon.



**Figure 4.6** Drawings that show the positions of the metal ions with respect to the adjacent walls of the  $C_{80}$  cage in  $CeSc_2N@C_{80}\cdot Ni^{II}(OEP)\cdot 2C_6H_6$ . The metal ions are projected onto the least-squares planes of the sets of carbon atoms shown as viewed from the inside of the cage.

Consideration of the pyramidalization of the carbon atoms in the  $C_{80}$  cage as measured by  $\theta_p$  ( $\theta_p$  for graphite =  $0^\circ$ ;  $\theta_p$  for  $C_{60}$  =  $11.6^\circ$ ) reveals that the adjacent metal ions inside and outside the cage exert a measurable effect on the cage structure of  $CeSc_2N@C_{80}$ . Figure 5.7 shows a plot of  $\theta_p$  for all of the cage carbon atoms in  $CeSc_2N@C_{80}\cdot Ni^{II}(OEP)\cdot 2C_6H_6$ . In the  $I_h$   $C_{80}$  cage, there are two types of carbon atoms: sixty (shown as squares in Figure 5.7) are part of the pentagons, while twenty others (shown as circles) do not reside in pentagons but are located at the confluence of three hexagons. The carbon atoms that are part of pentagons have an average  $\theta_p$  of  $9.92(6)^\circ$  while those at the confluence of three hexagons have an average  $\theta_p$  of  $8.82(2)^\circ$ . In calculating these averages we have omitted carbon atoms near the metal centers since these metal ions perturb the cage geometry. Thus, the four carbon atoms (C17, C37, C44, and C64) nearest to scandium atoms with Sc-C distances in the range 2.34-2.39 Å have the highest pyramidalization and appear as deep pink squares in Figure 5.7. The six carbon atoms that surround the cerium ion also have elevated values: these are shown in blue. Also the four carbon atoms (deep pink circles) that are 2.34- 2.39 Å from one of the scandium ions exhibit elevated values of  $\theta_p$ . Thus, the pattern clearly emerges that the carbon atoms near internal metal ions show enhanced pyramidalization. In contrast, the carbon atom (C46) nearest the external nickel ion in the porphyrin shows a reduced  $\theta_p$  value of 8.3 when compared to other carbon atoms like it that are part of pentagons. This observation is consistent with the situation seen in another well-ordered endohedral structure, that of the  $D_{5h}$  isomer of  $Sc_3N@C_{80}\cdot Ni(OEP)\cdot 2benzene$  where again the carbon atoms nearest the nickel ion are slightly flattened.



**Figure 4.7** The pyramidalization angles,  $\theta_p$ , for the carbon atoms in  $\text{CeSc}_2\text{N}@C_{80}$ . The sixty carbon atoms that are part of pentagons are shown as squares while the twenty others that do not reside in pentagons are shown as circles. Carbon atoms nearest internal metal atoms are colored (deep pink for the atoms near a scandium ion, blue for atoms near a cerium atom) and the remaining carbon atoms are represented by black symbols. A1 and B1, carbon atoms with no close contact with metal atoms inside the cage; A2, carbon atoms in pentagons near Ce; A3, carbon atoms in pentagons near Sc; B2 carbon atoms not in pentagons near Ce; B3 carbon atoms not in pentagons near Sc.

#### 4.2.2 $\text{Sc}_3\text{N}@C_{80}$ $D_{5h}$ isomer

In the HPLC trace and NI-DCI mass spectrum of the extract of  $\text{Ce}_x\text{Sc}_{3-x}\text{N}@C_{80}$  ( $x = 0-1$ ), the existence of both of  $I_h$  and  $D_{5h}$  isomers of  $\text{Sc}_3\text{N}@C_{80}$  was observed. Similar to  $\text{CeSc}_2\text{N}@C_{80}$ , the  $D_{5h}$  isomer was isolated through the new purification protocol and the two-stage HPLC separation. Its purity was confirmed by HPLC trace and NI-DCI mass spectrum. The  $D_{5h}$  isomer was characterized by UV-Vis spectrum and X-ray single crystal diffraction study.

Figure 4.8 shows a drawing of the four molecules present in the asymmetric unit of the compound. None of these has any crystallographically imposed symmetry. As usual, all eight ethyl groups of the porphyrin surround the fullerene. The closest contact between the porphyrin

and the endohedral is the 2.812(3) Å separation between Ni and C46. Remarkably, both the carbon cage and its contents are fully ordered. The cluster encapsulated is strictly planar and the sum of three Sc-N-Sc angles is 359.94 °. However, the geometry of the Sc<sub>3</sub>N portion is rather irregular with a variety of Sc-N distances (Sc1-N, 2.014(2), Sc2-N, 2.031(2); Sc3-N, 2.041(2) Å) and Sc-N-Sc angles (Sc1-N-Sc2, 121.12(11); Sc1-N-Sc3, 107.21(10); Sc2-N-Sc3, 131.61(11) °).

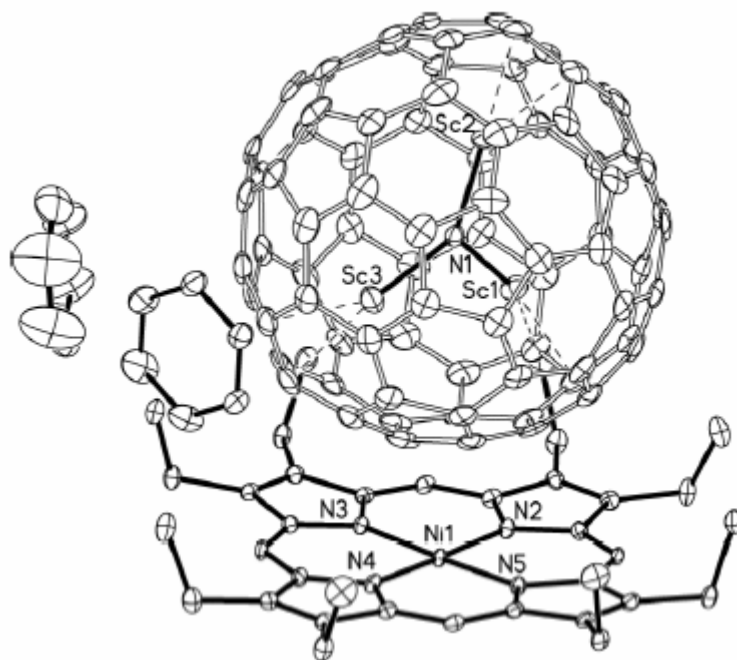


**Figure 4.8** A perspective view of the relative orientations of Sc<sub>3</sub>N@C<sub>80</sub> and Ni<sup>II</sup>(OEP) within crystalline Sc<sub>3</sub>N@C<sub>80</sub>•Ni<sup>II</sup>(OEP)•2C<sub>6</sub>H<sub>6</sub>.

Interestingly, The C-C bond distances in the carbon cage of D<sub>5h</sub> Sc<sub>3</sub>N@C<sub>80</sub> show greater variations than was observed in the corresponding I<sub>h</sub> isomer.<sup>5</sup> In I<sub>h</sub> Sc<sub>3</sub>N@C<sub>80</sub> there are only two types of C-C bonds while the D<sub>5h</sub> isomer has seven types of C-C bonds. The average distance of the longest bond is 1.462 Å and the shortest C-C bond is 1.396 Å, while there are only two types of C-C bonds (1.421 and 1.437 Å) in the I<sub>h</sub> isomer. The pyramidalization angles, θ<sub>p</sub> for the individual fullerene carbons of D<sub>5h</sub> Sc<sub>3</sub>N@C<sub>80</sub> also show some interesting variations.

The combination of short bond length and high degree of pyramidalization for the central carbon atoms of the pyracylene sites at the center of the carbon cage suggest that these may be the sites of greatest reactivity in the D<sub>5h</sub> isomer of Sc<sub>3</sub>N@C<sub>80</sub>. The two carbon atoms at the

center of pyracylene sites are generally the positions of highest chemical reactivity on empty cage fullerenes, but the  $I_h$  isomer of  $Sc_3N@C_{80}$  lacks such sites. The lack of this structural feature offers some insight into the low degree of chemical reactivity of the  $I_h$  isomer of  $Sc_3N@C_{80}$ .

## 4.3 Experimental

### 4.3.1 Materials and purification

Graphite rods (99.9995%C, 6.15 mm x 152 mm) and graphite powder (99.9995%C) were obtained from Alfa Aesar. The graphite rods were drilled longitudinally to provide a 4 mm hole, which was packed with  $Sc_2O_3$ ,  $CeO_2$ ,  $Fe_xN$  and graphite powder (2-15  $\mu m$ ); the metal oxide, Iron nitride and graphite powder were mixed with a mortar and pestle and the graphite rod was packed with the resultant mixture using a cotton tip applicator, followed by the blunt end of the 4 mm drill bit. Scandium (III) oxide ( $Sc_2O_3$ , 99.999%) and cerium (IV) oxide ( $CeO_2$ , 99.995%) were purchased from Stanford Materials Corporation. Iron nitride (99.9%,  $Fe_xN$ ,  $x = 2-4$ ) was obtained from Cerac Specialty Inorganic Chemicals. Merrifield's resin (chloromethylated styrene-1% divinylbenzene copolymer, 3.5-4.5 meq of Cl/g) and sodium cyclopentadienylide (2.0 M solution in tetrahydrofuran) were obtained from Sigma-Aldrich.

Solvents for extraction and chromatography were HPLC grade unless otherwise specified. HPLC separations were performed with an Acuflo Series III pump and Applied Biosystems 757 Absorbance Detector (detection wavelength set at 390 nm). Data was recorded on a Hitachi D-2500 Chromato-Integrator.  $CS_2$  (anhydrous, 99.99%) was used as received from Sigma-Aldrich and acetone- $d_6$  was used as received from Cambridge Isotope Laboratory.

### 4.3.2 Analytical methods

Mass spectra of endohedral metallofullerenes were obtained with a Fisons VG Quattro mass spectrometer using a negative ionization desorption chemical-ionization probe (NI-DCI). UV-Vis spectra were measured using quartz cuvettes and a Cary 50 UV-Visible

spectrophotometer (Varian, USA). The XPS spectrum was recorded on a Perkin-Elmer physical electronics model 5400 spectrometer.

$^{13}\text{C}$  NMR spectra were obtained with a JEOL Eclipse+ 500 spectrometer using a 5 mm NMR sample tube.  $^{45}\text{Sc}$  NMR spectra were recorded with either a JEOL Eclipse+ 500 spectrometer or Varian Unity 400 spectrometer using a 5 mm NMR sample tube.

#### 4.3.3 Production of $\text{CeSc}_2\text{N}@C_{80}$

Graphite rods (0.25 in. diameter, 6 in. length) were core-drilled and subsequently packed with a mixture of graphite powder,  $\text{Sc}_2\text{O}_3$ ,  $\text{CeO}_2$  and  $\text{Fe}_x\text{N}$ . The weight ratio of the components in the mixture is  $\text{C}:\text{Sc}_2\text{O}_3:\text{CeO}_2:\text{Fe}_x\text{N}=1.0:0.33:0.41:0.40$ .  $\text{Fe}_x\text{N}$  serves as a catalyst. These rods were then vaporized in a Krätschmer-Huffman generator under dynamic flow of He and  $\text{N}_2$  (flow rate ratio of  $\text{N}_2$ : He = 3:100) with total pressure of *Ca.* 300 torr to obtain soot containing  $\text{CeSc}_2\text{N}@C_{80}$ . The resulting soot was then extracted with refluxing toluene for 20 hours to obtain the initial endohedral extract. A portion of the negative ion desorption chemical ionization (NI-DCI) mass spectrum of the initial extract (Figure 4.9) confirms the existence of  $\text{CeSc}_2\text{N}@C_{80}$ .

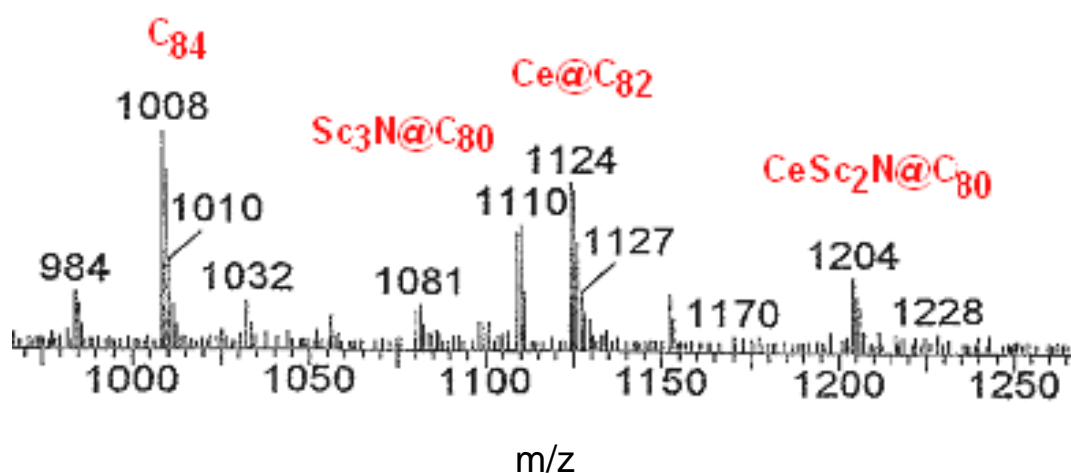


**Figure 4.9** A portion of NI-DCI MS spectrum of the extracts. The abundant peaks of  $\text{C}_{60}$  and  $\text{C}_{70}$  empty cages are not shown.

\* The production of the soot was completed by Tianming Zuo.

#### 4.3.4 Synthesis of Cyclopentadiene-Functionalized Resin

A suspension of chloromethylated styrene-divinylbenzene copolymer (1 g) in toluene (200 mL) was cooled to  $-20\text{ }^{\circ}\text{C}$ . sodium cyclopentadienylide (16 mL of a 2.0 M solution in tetrahydrofuran, 32 mmol, 8 equiv.) was added dropwise to the stirred suspension. Then the mixture was stirred for 2 h at  $20\text{ }^{\circ}\text{C}$  and filtered. The beads were washed with toluene (600 mL) to give the dark brown cyclopentadiene-functionalized Merrifield resin (Figure 4.10).

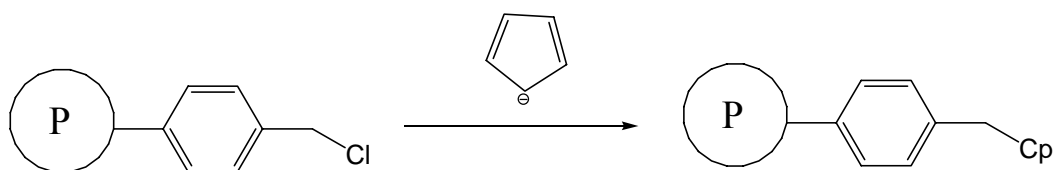


**Figure 4.10** Synthesis of Cyclopentadiene (Cp)-Functionalized Merrifield Resin.

#### 4.3.4 Separation of $\text{CeSc}_2\text{N@C}_{80}$

The extract was applied to a glass column (28 cm x 22 mm, h x d) packed with approximately 20 g of cyclopentadiene-functionalized Merrifield resin in toluene. Toluene was flushed through by gravity feed (around 20 mL/h). The HPLC traces of the extract were shown in Figure 4.11.

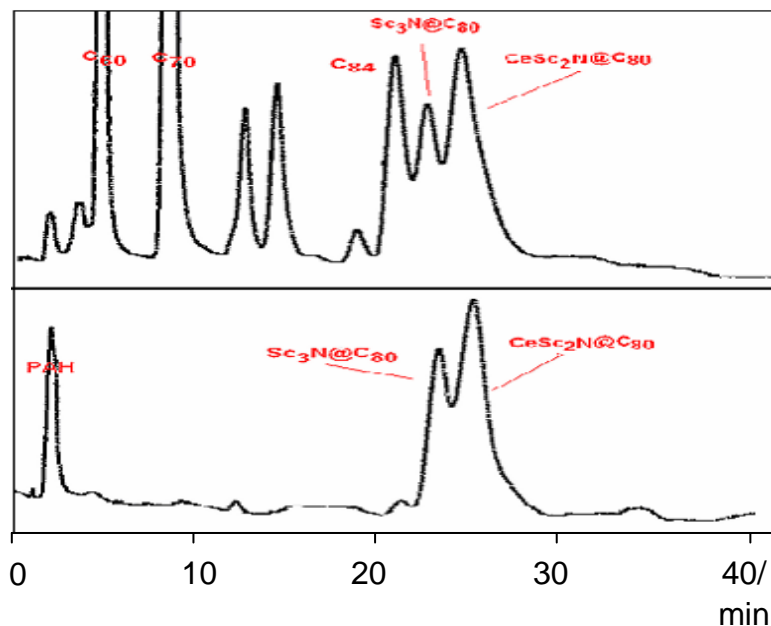


**Figure 4.11** Upper part: HPLC chromatogram of the extract (5PBB column, 4.6mm x 25 cm, toluene as eluent at a flow rate of 2 ml/min). Lower part: HPLC chromatogram of the sample after going through CPDE-MPR column.

The eluent was further separated using a 2-stage HPLC approach. First, the pentabromobenzyloxypropyl silica, 5PBB, column (250 x 4.6 mm, Alltech Associates) was employed with toluene as the mobile phase. The peak of  $\text{CeSc}_2\text{N}@C_{80}$  from this 5PBB column was collected and further separated with a 2-(1-pyrenyl)ethyl silica, 5PYE column (25cm x 10mm, Nacalai Tesque) using toluene as a mobile phase to obtain the purified  $\text{CeSc}_2\text{N}@C_{80}$  sample. From 5 packed graphite rods, approximately 3.0 mg of purified  $\text{CeSc}_2\text{N}@C_{80}$  was obtained.

### 4.3.5 Characterization of $\text{CeSc}_2\text{N}@C_{80}$

#### 4.3.5.1 XPS spectrum

A  $\text{CeSc}_2\text{N}@C_{80}$  film was prepared on a gold foil. To clean the gold surface, a small piece of gold foil was dipped in acetone and dried in  $\text{N}_2$  gas. Several drops of a concentrated solution of  $\text{CeSc}_2\text{N}@C_{80}$  in carbon disulfide were transferred to the cleaned gold foil and the evaporation of the solvent left a uniform film of  $\text{CeSc}_2\text{N}@C_{80}$ . The gold foil with the film on was heated in

vacuum line for 20 minutes. The XPS spectrum confirmed the existence of Sc and Ce (Figure 4.12). The C core level region indicates the  $\text{CeSc}_2\text{N}@C_{80}$  was not oxidized during the heating process. Otherwise, the C peak will not be symmetric.

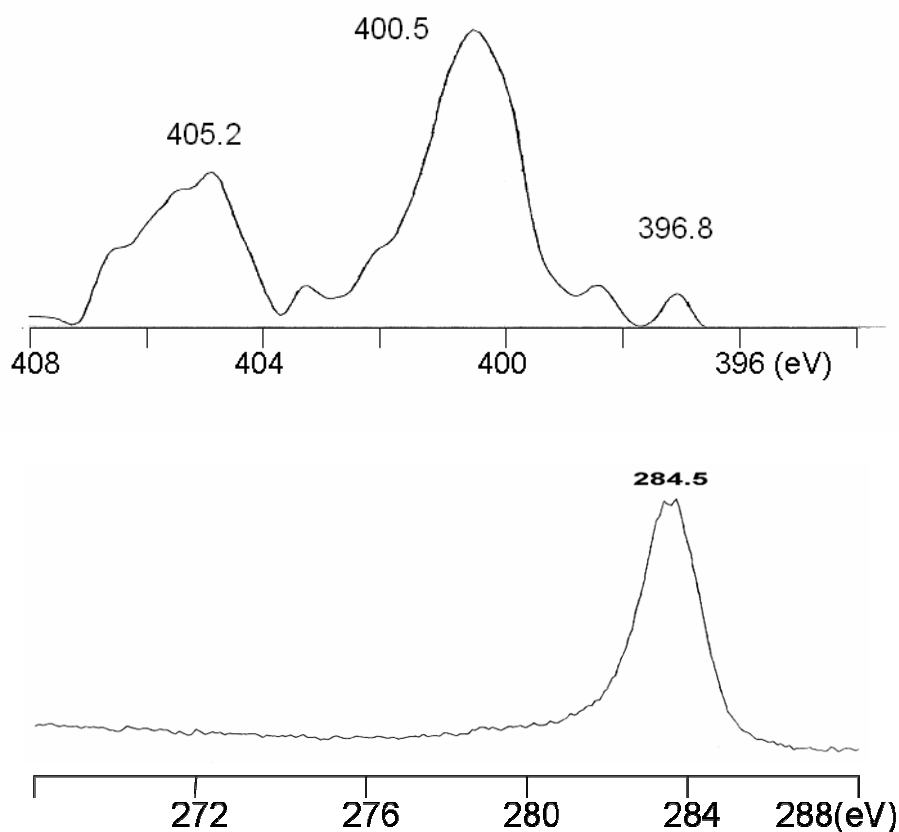


**Figure 4.12** XPS spectrum of  $\text{CeSc}_2\text{N}@C_{80}$  on a gold foil in the core level regions of Sc and N (Upper) and C (Lower).

#### 4.3.5.2 $^{13}\text{C}$ and $^{45}\text{Sc}$ NMR spectra

The 125 MHz  $^{13}\text{C}$  NMR spectrum of  $\text{CeSc}_2\text{N}@C_{80}$  in  $\text{CS}_2/\text{acetone-d}_6$  (v/v 9:1) was recorded on a JEOL 500 MHz instrument. Chromium(III) acetylacetonate (10 mg) was added as a relaxation agent. The 121.5 MHz  $^{45}\text{Sc}$  NMR spectrum of  $\text{CeSc}_2\text{N}@C_{80}$  in 1,2-dichlorobenzene at room temperature was recorded on the JEOL Eclipse+ 500 MHz instrument, and the 97.2 MHz  $^{45}\text{Sc}$  NMR spectra at various temperatures were recorded on a Unity 400 MHz instrument. The 121.5 MHz  $^{45}\text{Sc}$  NMR spectra of  $\text{Sc}_3\text{N}@C_{80}$  ( $I_h$ ) in 1,2-dichlorobenzene at various temperatures were recorded on the JEOL Eclipse+ 500 as a comparison.

Two graphs that exhibit the relationship between the chemical shift of Sc signals in  $^{45}\text{Sc}$  NMR spectra and the temperature are shown below (Figure 4.13 and 4.14).

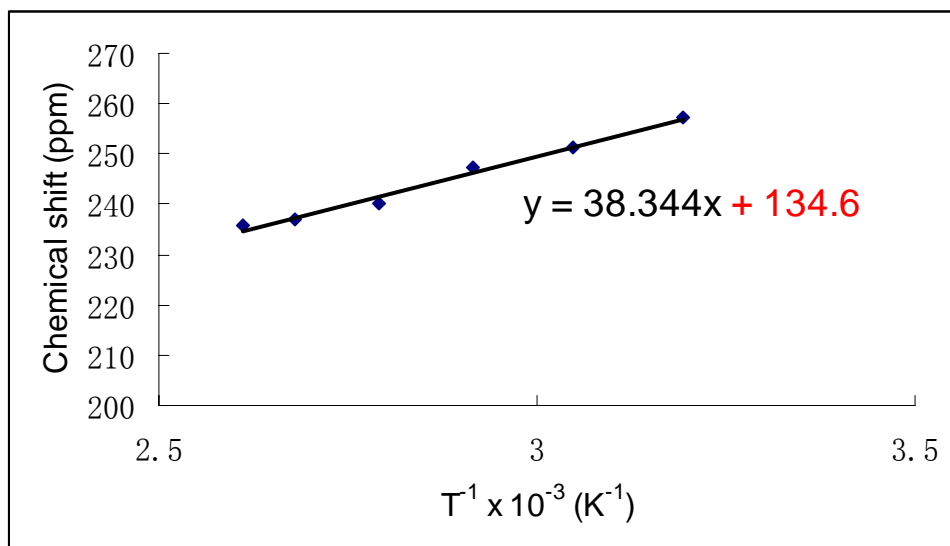


**Figure 4.13** Line-fitting plot for  $^{45}\text{Sc}$  NMR chemical shift vs  $T^{-1}$ . ( $r^2 = 0.9876$ ). The extrapolated value at  $T^{-1}=0$  is 134.6 ppm.

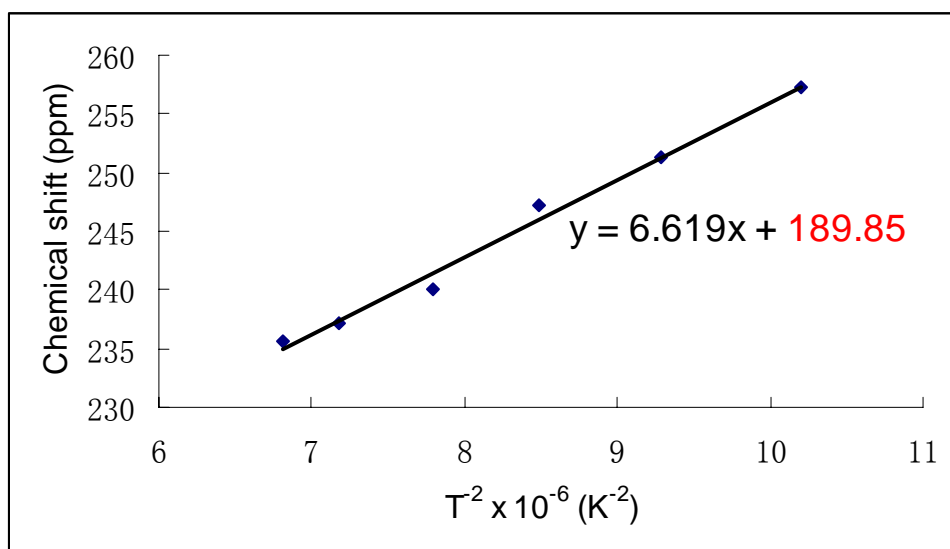


**Figure 4.14** Line-fitting plot for  $^{45}\text{Sc}$  NMR chemical shift vs  $T^{-2}$ . ( $r^2 = 0.9894$ ). The extrapolated value at  $T^{-2}=0$  is 189.85 ppm.

#### 4.3.5.3 Crystal study of $\text{CeSc}_2\text{N@C}_{80}\cdot\text{Ni}^{\text{II}}(\text{OEP})\cdot 2\text{C}_6\text{H}_6$

Crystals of  $\text{CeSc}_2\text{N@C}_{80}\cdot\text{Ni}^{\text{II}}(\text{OEP})\cdot 2\text{C}_6\text{H}_6$  were obtained by layering a solution of ca. 0.7 mg of  $\text{CeSc}_2\text{N@C}_{80}$  in 0.5 mL benzene over a solution of  $\text{Ni}^{\text{II}}(\text{OEP})$  in benzene. After the two solutions diffused together over a 14-day period, black crystals formed.

The crystals were removed from the glass tube in which they were grown together with a small amount of mother liquor and immediately coated with a hydrocarbon oil on the microscope slide. A suitable crystal was mounted on a glass fiber with silicone grease and placed on the goniometer head in the cold dinitrogen stream from a CRYO Industries low-temperature apparatus at 90(2) K. The diffractometer was Bruker SMART Apex with an Apex II CCD and utilized MoK $\alpha$  radiation. No decay was observed in 50 duplicate frames at the end of data collection. Crystal data are given below. The structure was solved by direct methods and refined using all data (based on  $F^2$ ) with the software of SHELXTL 5.1. A semiempirical method utilizing equivalents was employed to correct for absorption. Hydrogen atoms were added geometrically and refined with a riding model.

#### 4.3.6 $\text{Sc}_3\text{N@C}_{80}$ $\text{D}_{5h}$ isomer

##### 4.3.6.1 Isolation of $\text{Sc}_3\text{N@C}_{80}$ $\text{D}_{5h}$ isomer

The extract was applied to a glass column (28 cm x 22 mm, h x d) packed with approximately 20 g of cyclopentadiene-functionalized Merrifield resin in toluene. Toluene was flushed through by gravity feed (around 6 ml/h). The eluent was further separated using a 2-stage HPLC approach. First, the 5PBB column (25cm x 4.6mm, Alltech Associates) was employed with toluene as the mobile phase. The mixture of  $\text{CeSc}_2\text{N@C}_{80}$  and  $\text{Sc}_3\text{N@C}_{80}$  was collected (HPLC trace of the collected mixture was shown in Figure 4.15) and  $\text{Sc}_3\text{N@C}_{80}$   $\text{D}_{5h}$  isomer was further separated with a 5PYE, column (25cm x 10mm, Nacalai) using toluene as a mobile phase to obtain the purified  $\text{Sc}_3\text{N@C}_{80}$   $\text{D}_{5h}$  isomer sample (Figure 4.15). The purity of the  $\text{D}_{5h}$  isomer was confirmed by the HPLC trace (Figure 4.15) and LD-TOF mass spectrum (Figure 4.16).

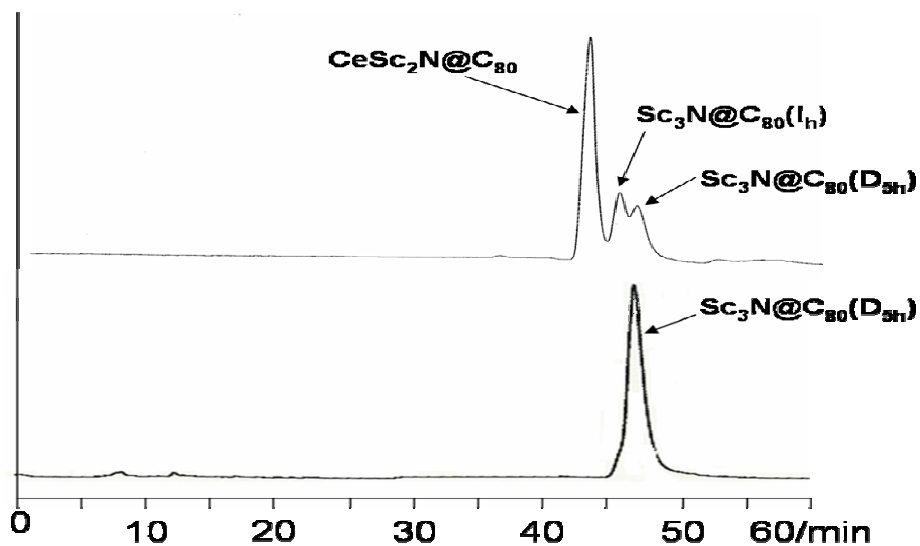


**Figure 4.15** HPLC traces of the Ce-Sc TNT endohedral metallofullerene mixture (top) and the isolated  $D_{5h}$  isomer of  $Sc_3N@C_{80}$  (bottom). 5PYE column (25cm x 10mm, Nacalai), toluene as mobile phase with a flow rate of 2.0 ml/min, detection at 390nm.

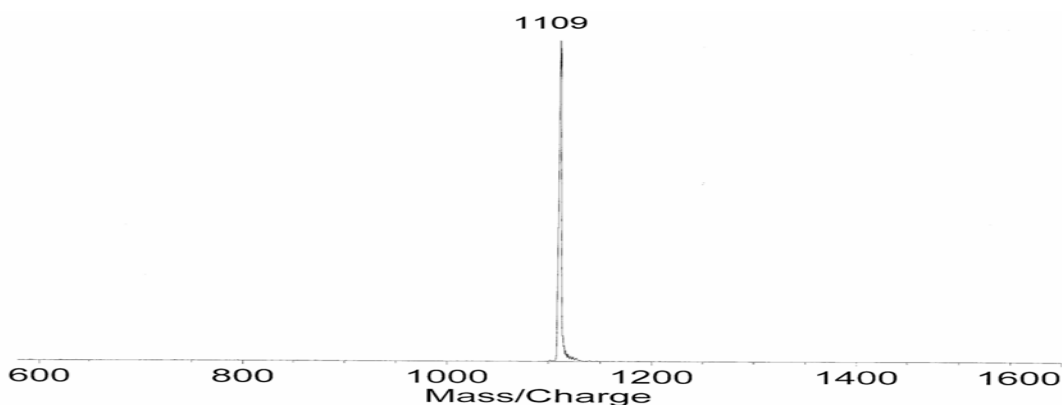


**Figure 4.16** LD-TOF mass spectrum of isolated  $D_{5h}$  isomer of  $Sc_3N@C_{80}$  (positive mode).

#### 4.3.6.2 Characterization of $Sc_3N@C_{80} D_{5h}$ isomer

The purified  $Sc_3N@C_{80} D_{5h}$  sample was characterized by UV-Vis and compared to  $Sc_3N@C_{80} I_h$  isomer (Figure 4.17). The spectrum is consistent with the published result.

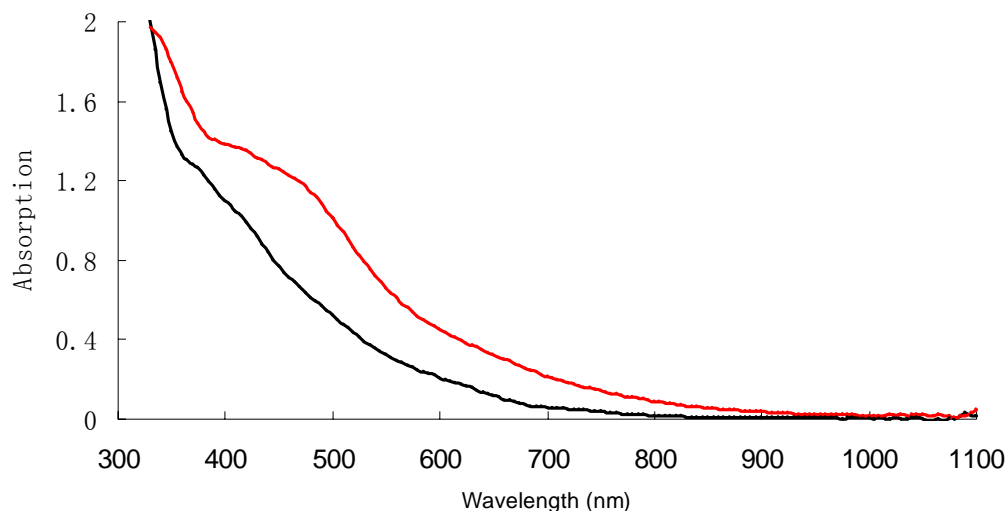


**Figure 4.17** UV-Vis spectra of Sc<sub>3</sub>N@C<sub>80</sub> Ih isomer (black) and D<sub>5h</sub> isomer (red).

Crystals of Sc<sub>3</sub>N@C<sub>80</sub>•Ni<sup>II</sup>(OEP)•2C<sub>6</sub>H<sub>6</sub> were obtained by layering a solution of ca. 0.5 mg of Sc<sub>3</sub>N@C<sub>80</sub> D<sub>5h</sub> isomer in 0.5 ml benzene over a solution of Ni<sup>II</sup>(OEP) in benzene. After the two solutions diffused together over a 14 days period, black crystals formed.

Crystal data for C<sub>128</sub>H<sub>56</sub>N<sub>5</sub>NiSc<sub>3</sub>: black parallelepiped, triclinic, space group *P1bar*,  $a = 14.505(3) \text{ \AA}$ ,  $b = 14.878(3) \text{ \AA}$ ,  $c = 19.855(4) \text{ \AA}$ ,  $\alpha = 85.052(3)^\circ$ ,  $\beta = 86.758(3)^\circ$ ,  $\gamma = 61.016(3)^\circ$ ,  $V = 3733.6(12) \text{ \AA}^3$ ,  $Z = 2$ ,  $D_c = 1.652 \text{ Mg/m}^3$ ,  $T = 90(2) \text{ K}$ ;  $R1 = 0.112$ ,  $wR2 = 0.124$  for all data; conventional  $R1 = 0.052$  computed for 13289 observed data ( $I > 2 \sigma(I)$ ) with 0 restraints and 1235 parameters.

# CHAPTER 5 - Cluster and Cage Motion of TNT Endohedral Metallofullerenes

## 5.1 Introduction

Early fullerene studies have demonstrated different motions for various cages. A wealth of information concerning the dynamics of fullerene cages has been acquired by analyzing the results of NMR experiments at lower temperatures. As for example, a study of  $C_{60}$ <sup>141,142</sup> at varying temperatures from 113 K to 193 K shows a transformation from the static lineshape to the isotropic, freely rotating  $C_{60}$ . Other studies concerning  $T_1$  measurements at different temperatures have been useful in confirming a phase transition between face-centered-cubic (FCC) and simple cubic (SC) phases.<sup>143</sup> Solid-state NMR has also proved valuable in characterizing molecules intercalated in  $C_{60}$ .<sup>144</sup> In endohedral fullerenes, there are motional dynamics both for the cage and the atoms/cluster inside the cage (Figure 5.1).

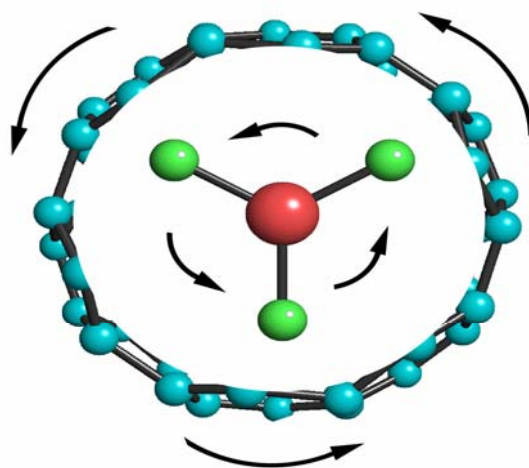


**Figure 5.1** A simple representation of metallic nitride cluster and carbon cage motions.

Since the successful isolation of a quantitative amount of endohedral metallofullerenes, various experiments have been used to shed light on the molecular and electronic structures of these molecules.<sup>145,146,147,148,149</sup> Among these experiments, NMR spectroscopy not only shows the direct evidence of the metal encapsulation inside the carbon cage, but also provides

information about the electronic and dynamic behavior of metal atoms inside fullerene cages. For instance, Miyake et al.<sup>134</sup> first used  $^{45}\text{Sc}$  NMR spectroscopy to show the internal motion of the scandium ions in two  $\text{Sc}_2@C_{84}$  isomers.  $^{139}\text{La}$  NMR study of  $\text{La}_2@C_{80}$  by Akasaka et al.<sup>13</sup> confirmed two encapsulated La atoms inside the  $C_{80}$  cage and circular motion inside even at room temperature. However, little is known concerning the dynamic of the clusters in TNT endohedral metallofullerenes until recently, Martindale and coworkers<sup>150</sup> measured  $^{13}\text{C}$  and  $^{45}\text{Sc}$  NMR lineshapes and spin-lattice relaxation times to probe the orientational dynamics of the endohedral metallofullerene  $\text{Sc}_3\text{N}@C_{80}$  in the solid state.

In this chapter, a series of  $^{45}\text{Sc}$  NMR experiments were conducted in solvents to characterize the cluster motion in TNT endohedral metallofullerenes. The resulting information is crucial in implementing applications of the TNT molecules from quantum computing to molecular gyroscopes, imaging contrast agents and opto-electronic devices.

## 5.2 Results and Discussions

### 5.2.1 Theory

In general, the quadrupolar relaxation mechanism is the dominant relaxation pathway for  $I > 1/2$  nuclei.<sup>151</sup> This process is highly dependent on the nature of the molecules under investigation. For small molecules with rapid molecular motion, the correlation time ( $\tau_c$ ) is much shorter than the reciprocal of the Larmor frequency of the nucleus ( $\omega_0$ ), which demonstrates  $\omega_0\tau_c \ll 1$ . In this “extreme narrowing” limit, the longitudinal ( $T_1$ ) and transverse ( $T_2$ ) relaxation times which characterize this relaxation process become equal and will remain equal as  $\tau_c$  becomes smaller. The general expression is given by:

$$\frac{1}{T_1} = \frac{1}{T_2} = \pi\Delta\nu_{\frac{1}{2}} = \frac{3\pi^2}{10} \frac{(2I+3)}{I^2(2I-1)} \chi^2 \left(1 + \frac{\eta^2}{3}\right) \tau_c \quad (1)$$

In the above equation,  $I$  is the spin number and  $\chi$  is the quadrupole coupling constant, a parameter that provides a measure of the coupling between the nuclear quadrupole and the electric field gradient at the nucleus.  $\eta$  is an asymmetry parameter and in most cases, the asymmetry correction  $(1 + \eta^2/3)$  is customarily ignored.

When the correlation time  $\tau_c$  for quadrupolar nuclei is longer than the reciprocal of its Larmor frequency ( $\omega_0\tau_c \gg 1$ ), relaxation is multiexponential. However, it has been predicted that in this molecular motion, the central ( $m = 1/2 \rightarrow -1/2$ ) transition of a half-integer quadrupolar nucleus (i.e.  $I = 3/2, 5/2$  and  $7/2$ ) can give rise to a relatively narrow signal, while the remaining transitions will broaden dramatically.<sup>152</sup> For  $I = 7/2$  nuclei, such as  $^{45}\text{Sc}$ , the linewidth of the signal for the central transition is:

$$\frac{1}{\pi T_2} = \Delta\nu_{\frac{1}{2}} = (2.5 \times 10^{-3}) \left( \frac{\chi^2}{\nu_0^2 \tau_c} \right) \quad (2)$$

It is worth noting that the linewidth in the “extreme narrowing” limit is directly proportional to the relaxation time (shown in equation 1) while the linewidth under the condition of  $\omega_0\tau_c \gg 1$  decreases with increasing  $\tau_c$  and depends on the resonance frequency of the nucleus (shown in

equation 2). In addition, the signal due to the central transition shifts to a lower frequency, which was termed the “second-order dynamic frequency shift”.<sup>153</sup> The magnitude of this shift, which is zero in the “extreme narrowing” limit ( $\omega_0\tau_c \ll 1$ ), decreases with increasing field and for  $I = 7/2$  nuclei is:

$$\Delta\delta_d = -(2.5 \times 10^{-3}) \left( \frac{\chi^2}{\nu_0^2} \right) \quad (3)$$

Thus in principle, from the observed second-order dynamic frequency shift, the quadrupole coupling constant can be calculated based on equation 3 shown above. Then provided the measured linewidth and calculated quadrupole coupling constant,  $\tau_c$  can be obtained from equation 1. With the assumption that the correlation time can be expressed by  $\tau_c = \tau_0 \exp(Ea/kT)$  ( $\tau_0$  is a constant), the free rotation time can be estimated and compared to the calculated value by  $\tau_{FR} = (3/5)(I/kT)^{1/2}$ .

### 5.2.2 <sup>45</sup>Sc NMR study of Sc<sub>3</sub>N@C<sub>80</sub> (I<sub>h</sub>)

The <sup>45</sup>Sc NMR spectrum for Sc<sub>3</sub>N@C<sub>80</sub> exhibits a single symmetric peak at temperatures above room temperature and the linewidth of the peak is not dependent on the viscosity of the solvent. For instance, at 303K the <sup>45</sup>Sc NMR linewidths for Sc<sub>3</sub>N@C<sub>80</sub> in the solvents carbon disulfide and o-dichlorobenzene are approximately 4300 and 4700 Hz, respectively. As a result of similar linewidths within the experimental error range, the Sc atom reorientation motion is suggested to be independent of the solution viscosity. These results also indicate that the internal motion provides the same average electronic environment for the three Sc atoms at this temperature. As shown in Figure 5.2 and Table 5.1, when temperature varies from 303 K to 393 K, the peak becomes sharper and chemical shift remains the same within the experimental error range. Assuming the correlation time can be expressed by:

$$\tau_c = \tau_0 \exp(Ea/kT) \quad (4)$$

where  $\tau_0$  is a constant and  $Ea$  represents an activation energy, and the linewidth is directly proportional to the correlation time, the linewidth data in table 1 can be fitted to yield the

activation energy,  $E_a = 0.075$  eV in the solvent o-dichlorobenzene. This barrier is lower than that for  $\text{Sc}_2@C_{84}$  isomer III,  $E_a = 0.088$  eV in o-dichlorobenzene. The relatively low Sc atom reorientation barrier (presumably dominated by motion internal to the cage) is consistent with the calculations (Hartree-Fock level) of the electrostatic map for the  $C_{80}^{6-}$  cage and corresponding low internal barriers reported by Nagase et al.<sup>12,126a</sup>

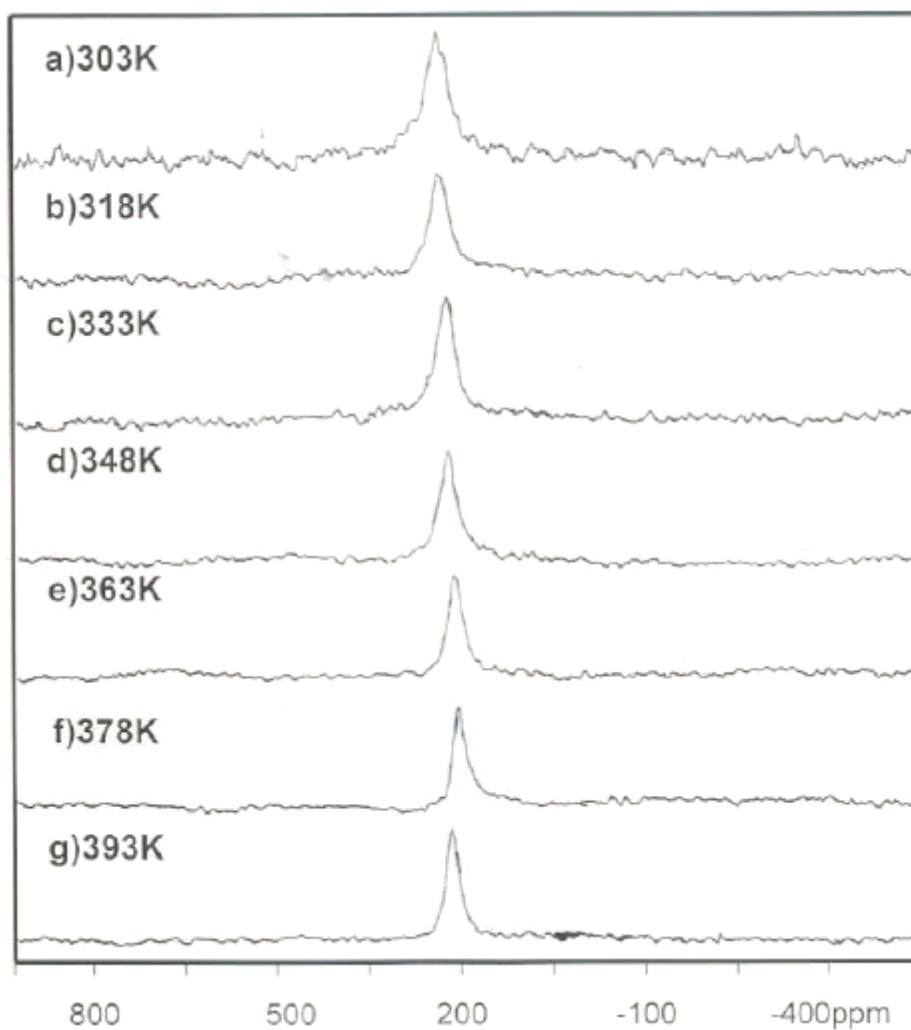


**Figure 5.2** 121.5 MHz  $^{45}\text{Sc}$  NMR spectra of  $\text{Sc}_3\text{N}@C_{80}$  ( $I_h$ ) in o-dichlorobenzene at various temperatures (303-393 K).

**Table 5.1** The linewidth and chemical shift of Sc signal of Sc<sub>3</sub>N@C<sub>80</sub> (I<sub>h</sub>) in o-dichlorobenzene at various temperatures.

Temperature (K)	1/T(K <sup>-1</sup> )	ln(Linewidth)	Chemical shift/ppm
303.15	0.003298697	8.3800	196.6
318.15	0.003143171	8.2409	196.9
333.15	0.003001651	8.1774	194.4
348.15	0.002872325	8.0365	194.1
363.15	0.002753683	7.8938	196.2
378.15	0.002644453	7.8109	194.4
393.15	0.002543558	7.7400	194.7

As shown in Figure 5.3, at temperatures below 283 K, the <sup>45</sup>Sc NMR linewidth for Sc<sub>3</sub>N@C<sub>80</sub> in o-dichlorobenzene rapidly increases and a measurable shift in the resonance frequency of the <sup>45</sup>Sc signal was observed from approximately 192.6 to 174.3 ppm (relative to external ScCl<sub>3</sub>). As shown previously for half-integer spin nuclei (i.e. Sc, I = 7/2), the central m = +1/2 to -1/2 transition for quadrupole nuclei in the limit of slow isotropic motion ( $\tau_c\omega_0 \gg 1$ ) exhibits a dynamic second-order frequency shift. From equation 3, where  $k = 2.5 \times 10^{-3}$  for Sc nuclear, a value of 10.4 MHz for the quadrupole coupling constant,  $\chi$  was calculated for Sc<sub>3</sub>N@C<sub>80</sub>. This quadrupole coupling is consistent with the range of  $\chi$  values (5-15 MHz) reported for a number of other Sc<sup>3+</sup> organic ligand and protein complexes,<sup>154,155</sup> but is significantly lower than the value reported for Sc<sub>3</sub>N@C<sub>80</sub> by Martindale et al.<sup>150</sup>

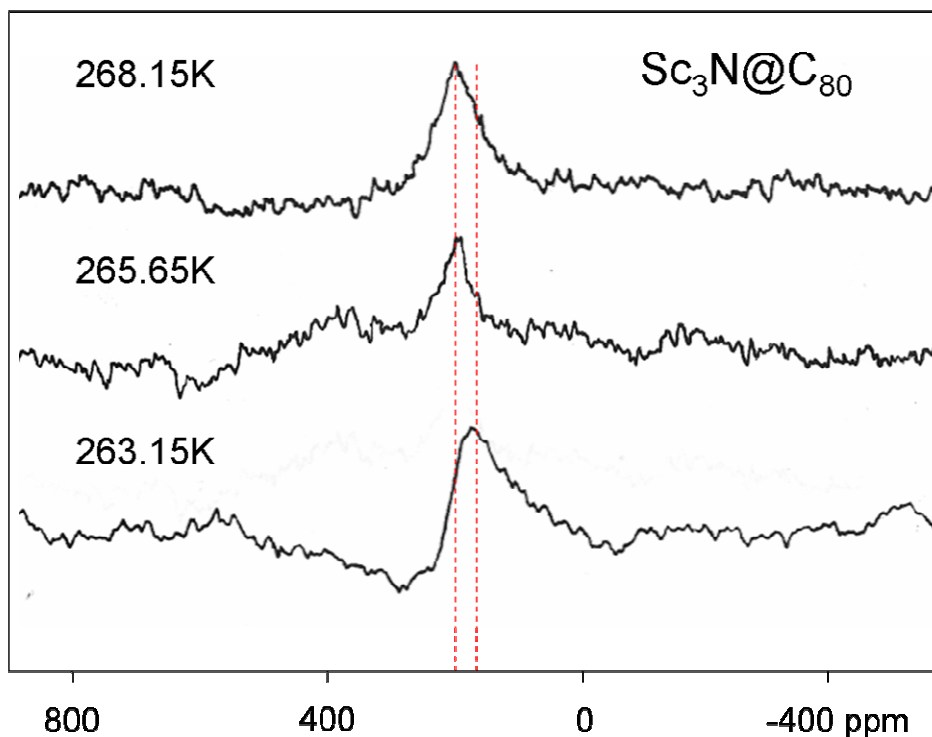


**Figure 5.3** 121.5 MHz  $^{45}\text{Sc}$  NMR spectra of  $\text{Sc}_3\text{N}@C_{80}$  ( $I_h$ ) in o-dichlorobenzene at different temperatures (263.15 – 268.15 K).

In addition, assuming  $\omega_0\tau_c \ll 1$  for  $\text{Sc}_3\text{N}@C_{80}$ , the correlation time at each temperature varying from 303 K to 393 K can be calculated from equation 1 provided that the value of the quadrupolar coupling constant is 10.4 MHz. Usually the correlation time can be expressed by the Debye-Stokes-Einstein formula, i.e.,

$$\tau_c = 4\pi R^3 \eta / kT \quad (5)$$

where  $R$  and  $\eta$  denote the hydrodynamic radius and the viscosity coefficient of the solvent, respectively. As shown in Figure 5.4, the graph of  $\tau_c$  vs  $\eta/T$  is linear. The free rotation time,  $\tau_{FR}$  is regarded as the limit approached by the actual  $\tau_\theta$  as the viscosity approaches zero or temperature goes to infinite. The free rotation time can be extrapolated from the fitted line and is 100 picoseconds.

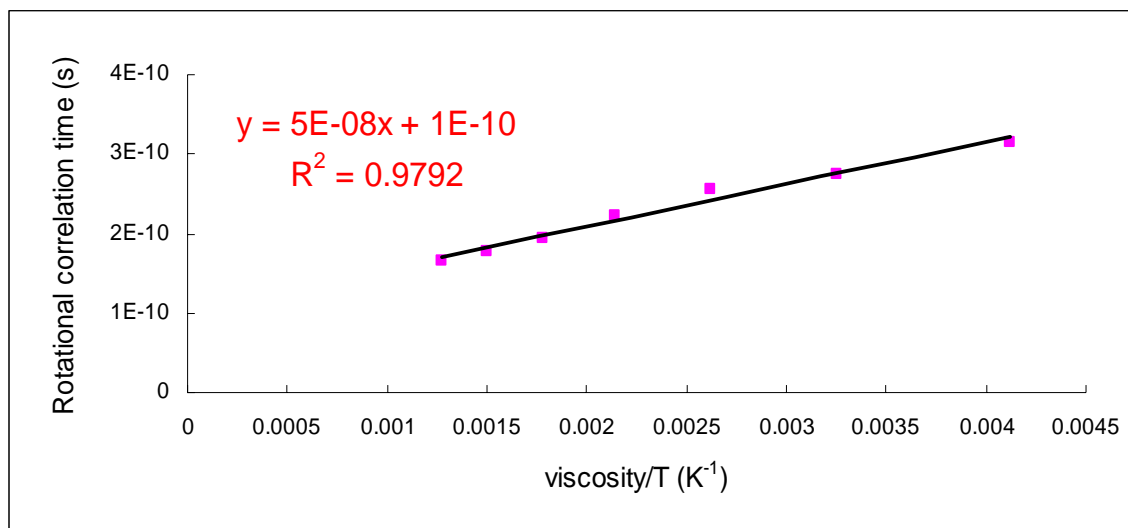


**Figure 5.4** The line-plotting of rotational correlation time vs  $\eta/T$  for  $^{45}\text{Sc}$  NMR signal of  $\text{Sc}_3\text{N}@C_{80}$  ( $I_h$ ).

### 5.2.3 $^{45}\text{Sc}$ NMR study of $\text{Sc}_3\text{N}@C_{68}$

The  $^{45}\text{Sc}$  NMR study of  $\text{Sc}_3\text{N}@C_{68}$  is of particular interest since we believe that the cluster does not rotate inside the cage due to the small size of  $C_{68}$  cage.

In similar fashion to the data reported for the  $\text{Sc}_3\text{N}@C_{80}$   $I_h$  isomer, the  $^{45}\text{Sc}$  NMR spectrum for  $\text{Sc}_3\text{N}@C_{68}$  shows a single symmetric peak at 308 K. Interestingly, the linewidth has shown some dependence on the viscosity of the solvent. As for example, at 308 K the  $^{45}\text{Sc}$  NMR linewidth for  $\text{Sc}_3\text{N}@C_{68}$  in more viscous solvent o-dichlorobenzene is considerably higher than that in less viscous solvent carbon disulfide (7000 vs 5800 Hz, respectively). When temperature varies from 318 K to 393 K, the  $^{45}\text{Sc}$  NMR peak for  $\text{Sc}_3\text{N}@C_{68}$  in o-dichlorobenzene becomes sharper while the chemical shift remains the same within the experimental error range (Figure 5.5). These data have been fitted to yield activation energy,  $E_a = 0.1186$  eV in o-dichlorobenzene. This Sc atom reorientation barrier (presumably dominated by motion internal to the cage) is significantly higher than that for  $\text{Sc}_3\text{N}@C_{80}$   $I_h$  isomer due to the smaller  $C_{68}$  cage, which hinders the rotation of the tetra-atomic cluster inside more than the relative larger  $C_{80}$  cage.

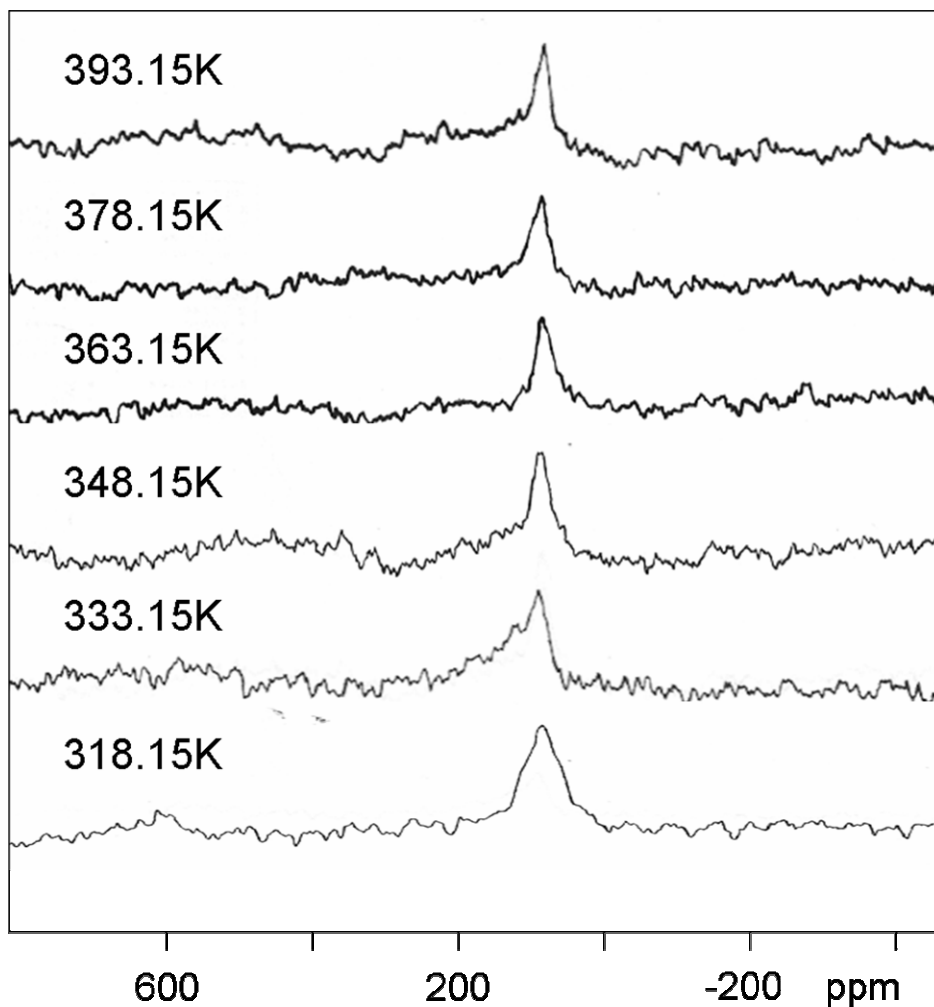


**Figure 5.5** 121.5 MHz  $^{45}\text{Sc}$  NMR spectra of  $\text{Sc}_3\text{N}@C_{68}$  in o-dichlorobenzene at various temperatures (318 – 393 K).

For  $\text{Sc}_3\text{N}@C_{68}$ , the “second-order dynamic shift” of Sc signal was also observed at temperatures below 305 K (Figure 5.6). Assuming a second order dynamic shift  $\Delta\delta_d = 16.8$  ppm, we calculate a value of 10.0 MHz for the quadrupole coupling constant  $\chi$  for  $\text{Sc}_3\text{N}@C_{68}$ . In spite of the large difference between the  $C_{68}$  and  $C_{80}$  cage, the quadrupole coupling constant for  $\text{Sc}_3\text{N}@C_{68}$  is only slightly smaller than that for  $\text{Sc}_3\text{N}@C_{80}$   $I_h$  isomer, which indicates the motion of TNT endohedral metallofullerene molecule might be dominated by the motion internal to the cage.

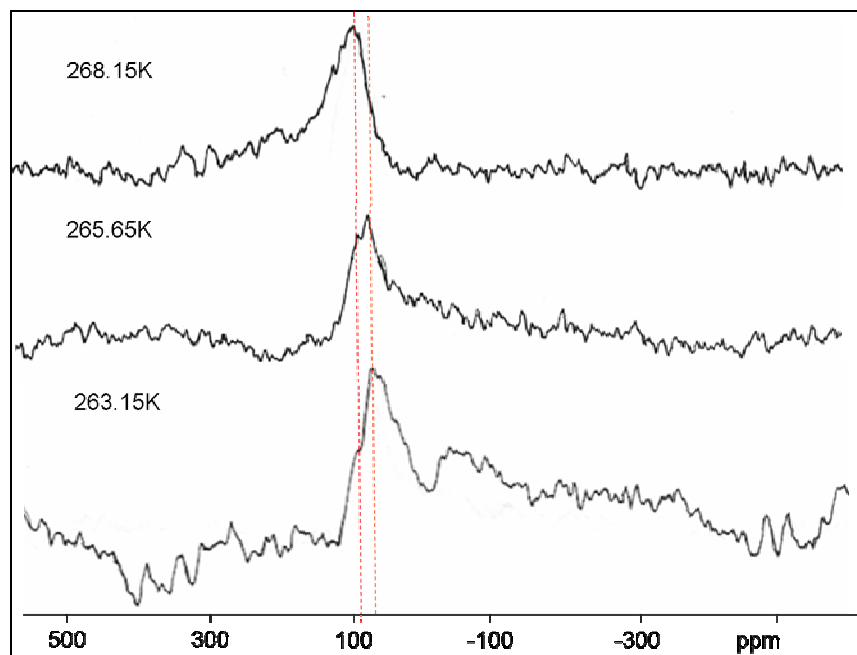


**Figure 5.6** 121.5 MHz  $^{45}\text{Sc}$  NMR spectra of  $\text{Sc}_3\text{N}@C_{68}$  in o-dichlorobenzene at various temperatures (263 – 268 K).

As shown in Figure 5.7, the graph of  $\tau_c$  vs  $\eta/T$  exhibits good linear relationship and free rotation time extrapolated from the graph is approximately 20 picoseconds, which is much smaller than that for  $\text{Sc}_3\text{N}@C_{80}$   $I_h$  isomer (approximately 100 picoseconds). The significant difference may be due to the different motion of cluster in the cages with different size ( $C_{68}$  vs  $C_{80}$ ). Interestingly, Martindale et al. measured  $^{13}\text{C}$  spin-lattice relaxation rate of  $\text{Sc}_3\text{N}@C_{80}$  in the solid state at various temperature and estimated a correlation time of 62 ps at  $T = 300\text{K}$ . This value is significantly lower than the value we calculated for  $\text{Sc}_3\text{N}@C_{80}$  (approximately 250 ps) in o-dichlorobenzene.

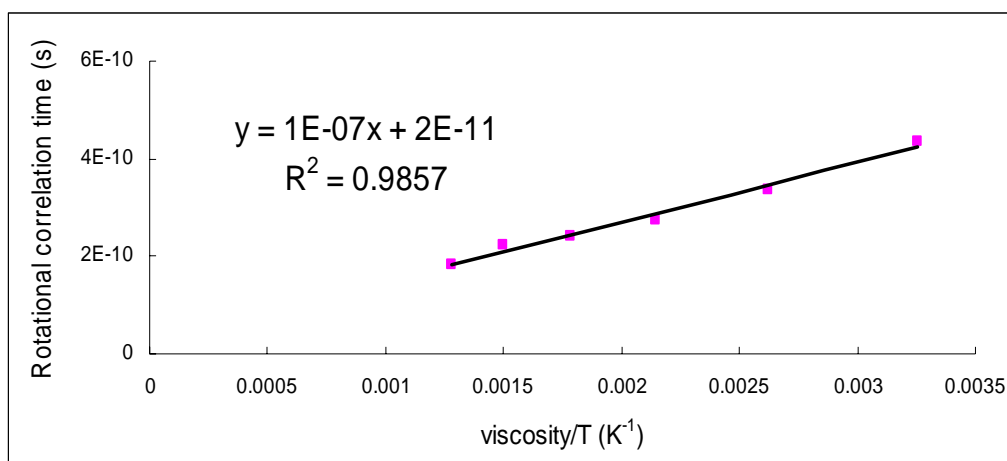


**Figure 5.7** The line-plotting of rotational correlation time vs  $\eta/T$  for  $^{45}\text{Sc}$  NMR signal of  $\text{Sc}_3\text{N}@C_{68}$ .

#### 5.2.4 $^{45}\text{Sc}$ NMR study of $\text{Sc}_3\text{N}@C_{78}$

Similar to  $\text{Sc}_3\text{N}@C_{68}$  and  $\text{Sc}_3\text{N}@C_{80}$ , the  $^{45}\text{Sc}$  NMR spectra of  $\text{Sc}_3\text{N}@C_{78}$  at high temperatures (348–393 K) show a single symmetric peak which indicates the three scandium ions are equivalent in the temperature range. As shown in Table 5.2, the chemical shifts of the peaks at various temperatures remain the same within the experimental range. Furthermore, when the temperature increases from 348 K to 393 K, the linewidth of the peak becomes sharper. The linewidth data was fitted (Figure 5.8), yielding the activation energy,  $E_a = 0.0990$  eV in *o*-dichlorobenzene. This reorientation barrier which was presumably dominated by cluster motion is higher than that of  $\text{Sc}_3\text{N}@C_{80}$  ( $I_h$  isomer), but lower than that of  $\text{Sc}_3\text{N}@C_{68}$ , which is logical because  $C_{78}$  cage is smaller than  $C_{80}$  and larger than  $C_{68}$ .

**Table 5.2** The linewidth and chemical shift of Sc signal of Sc<sub>3</sub>N@C<sub>78</sub> in o-dichlorobenzene at various temperatures.

Temp (K)	Linewidth (Hz)	ln(Linewidth)	Chemical shift (ppm)
393.15	4411.29	8.3919	216.4
383.15	4685.19	8.4522	220.1
378.15	5024.09	8.522	222.2
363.15	5752.97	8.6575	218.4
356.15	5968.7	8.6943	216.2
348.15	6371.34	8.7596	218.4

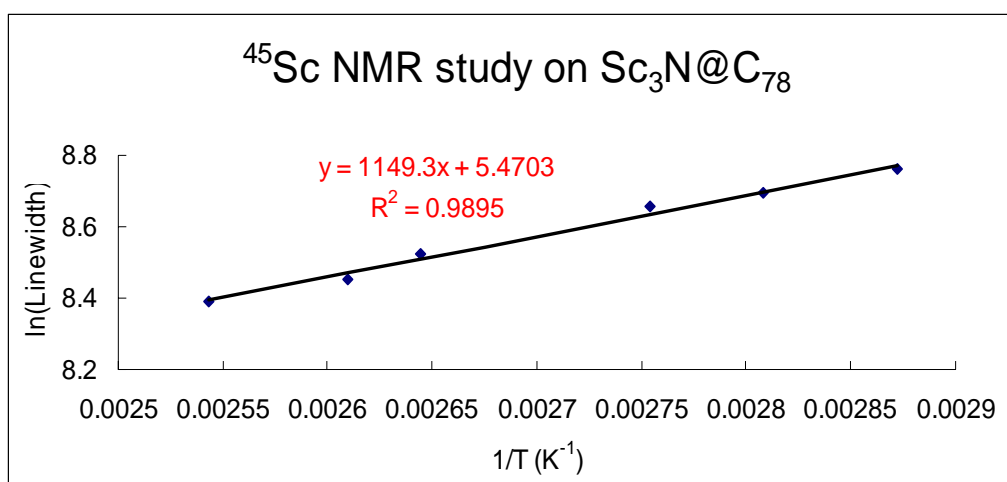


**Figure 5.8** The line-plotting of ln(linewidth) vs 1/T for Sc<sub>3</sub>N@C<sub>78</sub> in o-dichlorobenzene at various temperature (348-393 K).

However, the <sup>45</sup>Sc NMR experiments at temperatures lower than 348 K were not successful due to an unknown reason. Further study is needed to observe the second-order frequency shift for Sc<sub>3</sub>N@C<sub>78</sub> and calculate the quadrupole coupling constant.

### 5.2.5 Conclusions

The  $^{45}\text{Sc}$  solution NMR experiments have been performed on three TNT endohedral metallofullerenes,  $\text{Sc}_3\text{N}@C_{2n}$  ( $2n = 68, 78, 80$ ). This dynamic study has provided insight into the symmetry and motion of the cluster inside the carbonaceous cage. The activation barriers of  $\text{Sc}_3\text{N}@C_{68}$ ,  $\text{Sc}_3\text{N}@C_{78}$  and  $\text{Sc}_3\text{N}@C_{80}$  ( $I_h$ ) in the solvent of o-dichlorobenzene were 0.1186, 0.0990 and 0.075 eV, respectively. These Sc atom reorientation barriers (presumably dominated by motion internal to the cage) are consistent with the cage size difference among these three TNT endohedral metallofullerenes.

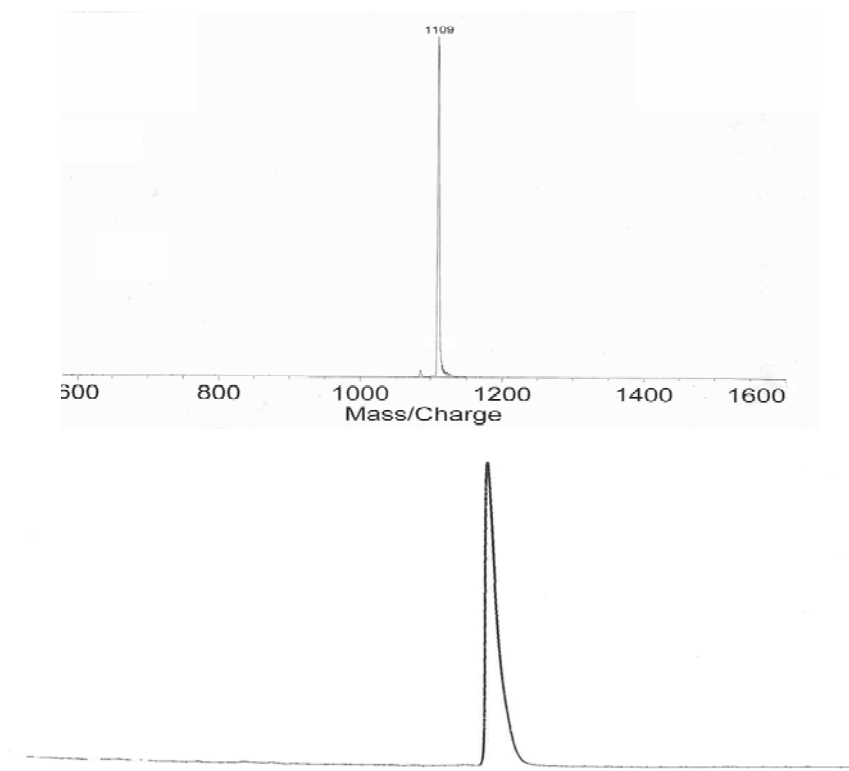
Furthermore, the second-order frequency shift phenomenon was observed for  $\text{Sc}_3\text{N}@C_{68}$  and  $\text{Sc}_3\text{N}@C_{80}$  at lower temperatures. Our experimental data shows the quadrupole coupling constants for these two fullerenes are only slightly different, which indicates the motion of the molecule might be dominated by the internal motion. However, the value we calculated for  $\text{Sc}_3\text{N}@C_{80}$  is some six times smaller than that recently reported by Martindale et al. Also, the reduced rotational correlation times for  $\text{Sc}_3\text{N}@C_{68}$  and  $\text{Sc}_3\text{N}@C_{80}$  have been estimated based on the experimental data. Further study on this project is needed.

## 5.3 Experimental

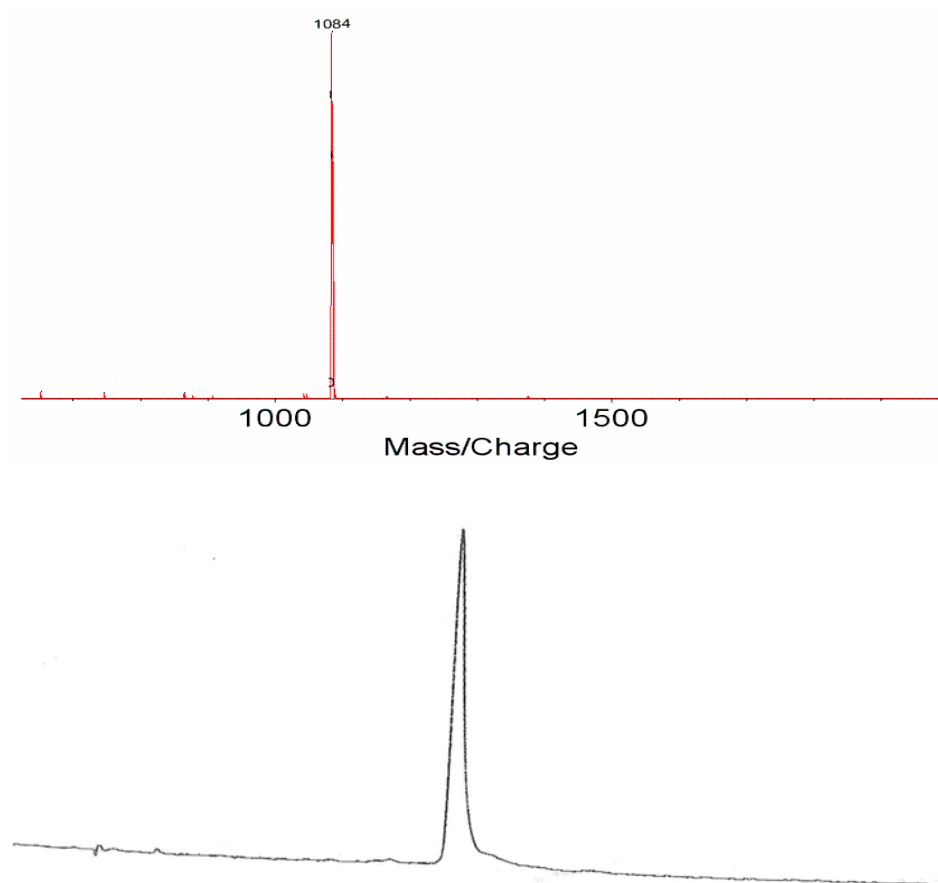
### 5.3.1 Materials and purifications

The three TNT endohedral metallofullerenes,  $\text{Sc}_3\text{N}@C_{2n}$  ( $2n = 68, 78, 80$ ) were synthesized and purified by Jonathan E. Reid. The purity was confirmed by HPLC trace and MALDI-TOF mass spectrum (see Figure 5.9, 5.10 and 5.11).  $\text{CS}_2$  (99.99%) and o-dichlorobenzene (99.9%) were purchased from Sigma-Aldrich and used as received.

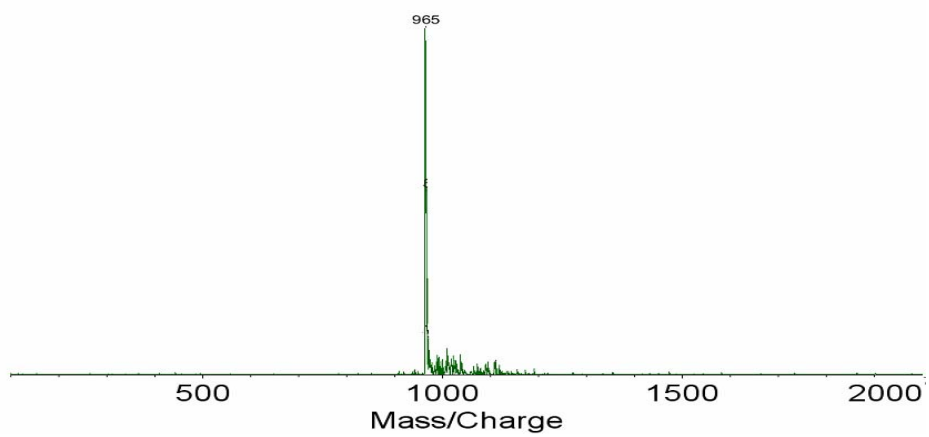
HPLC separations were performed with an Acuflo Series III pump and Applied Biosystems 757 Absorbance Detector (detection wavelength set at 390 nm). Data was recorded on a Hitachi D-2500 Chromato-Integrator.



**Figure 5.9** MALDI-TOF mass spectrum (top) and HPLC trace (bottom, 5PYE column, 10 x 250 mm, toluene, 2.0 ml/min, detection wavelength set at 390 nm) of  $\text{Sc}_3\text{N}@C_{80} I_h$  isomer.



**Figure 5.10** MALDI-TOF mass spectrum (top) and HPLC trace (bottom, 5PYE column, 10 x 250 mm, toluene, 2.0 ml/min, detection wavelength set at 390 nm) of  $\text{Sc}_3\text{N}@C_{78}$ .



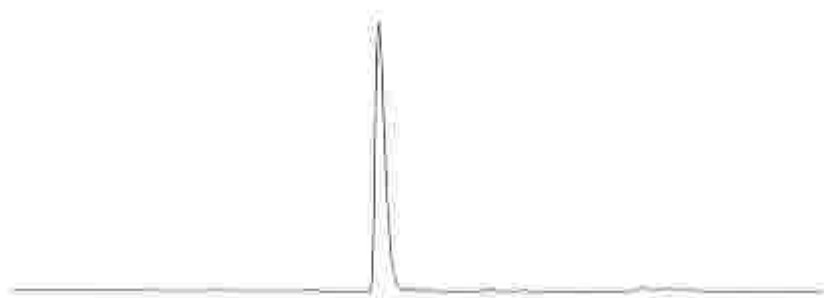


**Figure 5.11** MALDI-TOF mass spectrum (top) and HPLC trace (bottom, 5PYE column, 10 x 250 mm, toluene, 2.0 ml/min, detection wavelength set at 390 nm) of Sc<sub>3</sub>N@C<sub>68</sub>.

### 5.3.2 Analytical method

Solutions of Sc<sub>3</sub>N@C<sub>2n</sub> (2n = 68, 78, 80) were prepared in CS<sub>2</sub> and o-dichlorobenzene, degassed and placed under argon atmosphere before NMR measurements. <sup>45</sup>Sc solution NMR spectra were obtained at 121.5 MHz using JEOL 500 spectrometer. The <sup>45</sup>Sc chemical shift scale was calibrated using 1 mol/L ScCl<sub>3</sub> in aqueous solution as an external reference (0 ppm).

# CHAPTER 6 - Summary, Conclusions and Future Work

## 6.1 Summary and Conclusions

The HSVM technique has been successfully applied in the functionalization of endohedral metallofullerenes. By utilizing the HSVM technique and the new purification protocol, the water-soluble metallofullerols of trimetallic nitride endohedral metallofullerenes,  $A_3N@C_{80}(OH)_m(O)_n$  ( $A = Sc, Gd, Ho$ ) were prepared in two facile steps from the Kratschmer-Huffman raw soot in only two days. The time-saving procedure is of great importance to the further radiolabelling study due to the short half-lives of most lanthanide metals. The synthesized metallofullerols were characterized using FT-IR, XPS and MALDI-TOF mass spectrum. Furthermore, the relaxivity study on both high (9.4 T) and low (0.35 T) fields shows the Gd-based TNT metallofullerols demonstrated greater relaxivities than other reported water-soluble Gd-based endohedral metallofullerene derivatives. These results indicate the potential of  $Gd_3N@C_{80}(OH)_m(O)_n$  to be the next generation MRI contrast agents. Interestingly, it was found that  $Ho_3N@C_{80}(OH)_m(O)_n$  shows much higher  $r_2/r_1$  ratio than Gd and Sc analogues. The high  $r_2/r_1$  ratio indicates the Ho-based water-soluble endohedral metallofullerols have the potential to be a  $T_2$  contrast agent. The control experiments prove that the paramagnetism originates from the cluster encapsulated in the cage and the relaxation mechanism is the outer-sphere mechanism.

A mixed-metal trimetallic nitride template endohedral metallofullerene,  $CeSc_2N@C_{80}$  has been synthesized, isolated and characterized by DCI MS, XPS,  $^{45}Sc$  and  $^{13}C$  NMR, UV-Vis and single-crystal X-ray diffraction. In spite of an example of  $ErSc_2N@C_{80}$  which was only characterized by X-ray diffraction, the  $CeSc_2N@C_{80}$  will be the first case of mix-metal species that has been fully characterized. The remarkable similarities between  $Sc_3N@C_{80}$  and  $CeSc_2N@C_{80}$  with respect to HPLC retention times, UV-Visible spectra suggest a relatively minor influence of the internal trimetallic nitride cluster on the cage properties of these two endohedral metallofullerenes. The  $^{45}Sc$  NMR spectra at various temperatures prove the paramagnetic nature of the  $CeSc_2N@C_{80}$  molecule and show the activation energy is  $79 \pm 6$  meV for the rotation energy barrier (presumably dominated by the motion internal to the cage)

of CeSc<sub>2</sub>N@C<sub>80</sub> in 1, 2-dichlorobenzene. The XPS spectrum confirms the oxidation state of Ce is +3. In spite of its paramagnetic nature, the CeSc<sub>2</sub>N@C<sub>80</sub> exhibits a <sup>13</sup>C NMR spectrum consisting of two lines with a intensity ratio of 3:1. These results not only prove the I<sub>h</sub> symmetry of the C<sub>80</sub> cage in CeSc<sub>2</sub>N@C<sub>80</sub>, but suggest the one 4f electron on cerium was buried. The single-crystal X-ray diffraction study on CeSc<sub>2</sub>N@C<sub>80</sub>•Ni<sup>II</sup>(OEP)•2C<sub>6</sub>H<sub>6</sub> confirms the encapsulation of a planar tetra-atomic cluster inside the I<sub>h</sub> C<sub>80</sub> cage. The cerium ion within the cage is positioned below the center of a hexagon, while the scandium ions are located near 6:5 ring junctions with displacements toward the hexagons. Due to the large size of the Ce ion, the N atom is pushed 0.36 Å away from the central position toward the two scandium ions, which makes the compressed Sc-N bond lengths even shorter than those in Sc<sub>3</sub>N@C<sub>68</sub> (1.942(2) and 1.933(2) in CeSc<sub>2</sub>N@C<sub>80</sub> vs 1.961(4), 1.974(4), and 2.022(3) in Sc<sub>3</sub>N@C<sub>68</sub>).

The D<sub>5h</sub> isomer of Sc<sub>3</sub>N@C<sub>80</sub> was also isolated and characterized by a crystallographic study. The cluster is strictly planar, but it shows a larger variation of Sc-N distances and Sc-N-Sc angles than that in I<sub>h</sub> isomer of Sc<sub>3</sub>N@C<sub>80</sub>. The C-C bond distances in the carbon cage of D<sub>5h</sub> Sc<sub>3</sub>N@C<sub>80</sub> also show greater variations than those in the corresponding I<sub>h</sub> cage. In D<sub>5h</sub> Sc<sub>3</sub>N@C<sub>80</sub> there are seven types of C-C bonds while I<sub>h</sub> isomer has only two types. The average distance of the longest bond is 1.462 Å and the shortest C-C bond is 1.396 Å. The D<sub>5h</sub> isomer was found to possess the pyracylene patches while the I<sub>h</sub> isomer does not have those units. The two carbons atoms at the center of pyracylene sites are generally the positions of highest chemical reactivity on empty cage fullerenes. This may explain why the D<sub>5h</sub> isomer has greater reactivity than the I<sub>h</sub> isomer.

<sup>45</sup>Sc solution NMR was used as a tool to explore the motion of the three trimetallic nitride endohedral metallofullerenes, Sc<sub>3</sub>N@C<sub>2n</sub> (2n = 68, 78, 80). The <sup>45</sup>Sc NMR spectra of these three endohedral metallofullerenes at various temperatures and/or in different solvents have provided insight into the symmetry and motion of the cluster inside the carbonaceous cage. It was found the activation barriers of Sc<sub>3</sub>N@C<sub>68</sub>, Sc<sub>3</sub>N@C<sub>78</sub> and Sc<sub>3</sub>N@C<sub>80</sub> (I<sub>h</sub>) in the solvent of o-dichlorobenzene were 118.6, 99 and 75 meV, respectively. Furthermore, the quadrupolar coupling constants for Sc<sub>3</sub>N@C<sub>68</sub> and Sc<sub>3</sub>N@C<sub>80</sub> (I<sub>h</sub> isomer) were calculated based on the second-order frequency shift observed at the lower temperature <sup>45</sup>Sc NMR spectra.

## 6.2 Future work

The HSVM technique has shown promise for being a different way to functionalize trimetallic nitride template endohedral metallofullerenes. Some functionalizations, such as the Prato reaction and Bingel-Hirsch reaction which have been proved to work well in the solvents, can be tried under the HSVM condition.

Functionalization of mixed-metal TNT endohedral metallofullerenes is of great importance with the respect of exploring how the encapsulated cluster affects the cage reactivity. It is also very crucial to the application of mixed-metal endohedral metallofullerene derivatives as the multi-module contrast agents. Compared with other mixed-metal TNT endohedral metallofullerenes, such as  $\text{Er}_x\text{Sc}_{3-x}\text{N}@C_{80}$  and  $\text{Lu}_x\text{Ho}_{3-x}\text{N}@C_{80}$  ( $x = 1-2$ ),  $\text{CeSc}_2\text{N}@C_{80}$  has some advantages since the larger size of the cerium ions prevents the encapsulation of more than one cerium ion into the  $C_{80}$  cage, which makes the isolation and purification simpler and the yield relatively higher. Also it is of interest to figure out how the buried f electron affects the  $^{13}\text{C}$  NMR of the  $\text{CeSc}_2\text{N}@C_{80}$  derivative.

## Reference

- <sup>1</sup> Kroto, H. W.; Heath, J. R.; O'Brien, S. C.; Curl, R. F.; Smalley, R. E. C<sub>60</sub>: Buckminsterfullerene. *Nature* **1985**, *318*, 162-163.
- <sup>2</sup> Heath, J. R.; O'Brien, S. C.; Zhang, Q.; Liu, Y.; Curl, R. F.; Kroto, H. W.; Tittel, F. K.; Smalley, R. E. Lanthanum Complexes of Spheroidal Carbon Shells. *J. Am. Chem. Soc.* **1985**, *107*, 7779-7780.
- <sup>3</sup> Chai, Y.; Guo, T.; Jin, C.; Haufler, R. E.; Chibante, L. P.; Fure, J.; Wang, L.; Alford, J. M.; Smalley, R. E. Fullerenes with Metals inside. *J. Phys. Chem.* **1991**, *95*, 7564-7568.
- <sup>4</sup> Liu, S.; Sun, S. Recent Progress in the Studies of Endohedral Metallofullerenes. *J. Organomet. Chem.* **2000**, *599*, 74-86.
- <sup>5</sup> Stevenson, S.; Rice, G.; Glass, T.; Harich, K.; Cromer, F.; Jordan, M. R.; Craft, J.; Hadju, E.; Bible, R.; Olmstead, M. M.; Maltra, K.; Fisher, A. J.; Balch, A. L.; Dorn, H. C. Small-bandgap Endohedral Metallofullerenes in High Yield and Purity. *Nature*, **1999**, *401*, 55-57.
- <sup>6</sup> Stevenson, S.; Fowler, P. W.; Heine, T.; Duchamp, J. C.; Rice, G.; Glass, T.; Harich, K.; Hajdu, E.; Bible, R.; Dorn, H. C. A Stable non-Classical Metallofullerene Family. *Nature*, **2000**, *408*, 427-428.
- <sup>7</sup> Olmstead, M. M.; de Bettencourt-Dias, A.; Duchamp, J. C.; Stevenson, S.; Marciu, D.; Dorn, H. C.; Balch, A. L. Isolation and Structural Characterization of the Endohedral Fullerene Sc<sub>3</sub>N@C<sub>78</sub>. *Angew. Chem. Int. Ed. Engl* **2001**, *40*, 1223-1225.
- <sup>8</sup> Campanera, J. M.; Bo, C.; Olmstead, M. M.; Balch, A. L.; Poblet, J. M. Bonding within Endohedral Fullerenes Sc<sub>3</sub>N@C<sub>78</sub> and Sc<sub>3</sub>N@C<sub>80</sub> as Determined by Density Functional Calculations and Reexamination of the Crystal Structure of {{Sc<sub>3</sub>N@C<sub>78</sub>}Co(OEP)}1.5{C<sub>6</sub>H<sub>6</sub>}0.3(CHCl<sub>3</sub>). *J. Phys. Chem. A* **2002**, *106*, 12356-12364.
- <sup>9</sup> Kroto, H. W. The Stability of the Fullerenes C<sub>n</sub>, with n = 24, 28, 32, 36, 50, 60 and 70. *Nature*, **1987**, *329*, 529-531.
- <sup>10</sup> Schmalz, T. G.; Seitz, W. A.; Klein, D. J.; Hite, G. E. Elemental Carbon Cages. *J. Am. Chem. Soc.* **1988**, *110*, 1113-1127
- <sup>11</sup> Wang, C. R.; Kai, T.; Tomiyama, T.; Yoshida, T.; Kobayashi, Y.; Nishibori, E.; Takata, M.; Sakata, M.; Shinohara, H. C<sub>66</sub> Fullerene Encaging a Scandium Dimer. *Nature*, **2000**, *408*, 426-428.
- <sup>12</sup> Kobayashi, K.; Nagase, S. Structures and Electron State of Endohedral Dimetallofullerenes:

- 
- M<sub>2</sub>@C<sub>80</sub> (M = Sc, Y, La, Ce, Pr, Eu, Gd, Yb and Lu). *Chem. Phys. Lett.* **1996**, 262, 227-232
- <sup>13</sup> Akasaka, T.; Nagase, S.; Kobayashi, K.; Walchli, M.; Yamamoto, K.; Funasaka, H.; Kako, M.; Hoshino, T.; Erata, T. <sup>13</sup>C and <sup>139</sup>La NMR Studies of La<sub>2</sub>@C<sub>80</sub>: First Evidence for Circular Motion of Metal Atoms in Endohedral Dimetallofullerenes. *Angew. Chem. Int. Ed. Engl.* **1997**, 36, 1643-1645.
- <sup>14</sup> Hennrich, F. H.; Michel, R. H.; Fisher, A.; Richard-Schneider, S.; Gilb, S.; Kappes, M. M.; Fuchs, D.; Burk, M.; Kobayashi, K.; Nagase, S. Isolation and Characterization of C<sub>80</sub>. *Angew. Chem. Int. Ed. Engl.* **1996**, 35, 1732-1734.
- <sup>15</sup> Kobayashi, K.; Nagase, S.; Akasaka, T. A Theoretical Study of C<sub>80</sub> and La<sub>2</sub>@C<sub>80</sub>. *Chem. Phys. Lett.* **1995**, 245, 230-236.
- <sup>16</sup> Krause, K.; Kuzmany, H.; Georgi, P.; Dunsch, L.; Vietze, K.; Seifert, G. Structure and Stability of Endohedral Fullerene Sc<sub>3</sub>N@C<sub>80</sub>: A Raman, Infrared and Theoretical Analysis. *J. Chem. Phys.* **2001**, 115, 6596-6605.
- <sup>17</sup> Alvarez, L.; Pichler, T.; Georgi, P.; Schwieger, T.; Peisert, H.; Dunsch, L.; Hu, Z.; Knupfer, M.; Fink, J.; Bressler, P.; Mast, M.; Golden, M. S. Electronic Structure of Pristine and Intercalated Sc<sub>3</sub>N@C<sub>80</sub> Metallofullerene. *Phys. Rev. B* **2002**, 66, 035107/1-035107/7.
- <sup>18</sup> Duchamp, J. C.; Demortier, A.; Fletcher, K. R.; Dorn, D.; Iezzi, E. B.; Glass, T.; Dorn, H. C. An Isomer of the Endohedral Metallofullerene Sc<sub>3</sub>N@C<sub>80</sub> with D<sub>5h</sub> Symmetry. *Chem. Phys. Lett.* **2003**, 375, 655-659.
- <sup>19</sup> Yang, S.; Dunsch, L. Expanding the Number of Stable Isomeric Structures of the C<sub>80</sub> Cage: a New Fullerene Dy<sub>3</sub>N@C<sub>80</sub>. *Chem. Eur. J.* **2006**, 12, 413-419.
- <sup>20</sup> Dunsch, L.; Krause, M.; Noack, J.; Georgi, P. Endohedral Nitride Cluster Fullerenes: Formation and Spectroscopic Analysis of L<sub>3-x</sub>M<sub>x</sub>N@C<sub>2n</sub> (x = 0-3; N = 39,40). *J. Phys. Chem. Solid* **2004**, 65, 309-315.
- <sup>21</sup> Shelimov, K. B.; Clemmer, D. E.; Jarrold, M. F. Structures and Formation of Small LaC<sub>n</sub><sup>+</sup> Metallofullerenes. *J. Phys. Chem.* **1994**, 98, 12819-12821.
- <sup>22</sup> Rubin, Y. Ring Opening Reactions of Fullerenes: Designed Approaches to Endohedral Metallofullerenes. In *Fullerenes and Related Structures*. Hirsch, A., Ed. Topics in Current Chemistry; Springer-Verlag: New York, **1999**; 199, 67-91.
- <sup>23</sup> Ge, Z.; Duchamp, J. C.; Cai, T.; Gibson, H. W.; Dorn, H. C. Purification of Endohedral Trimetallic Nitride Fullerenes in a Single, Facile Step. *J. Am. Chem. Soc.* **2005**, 127, 16292-16298.
- <sup>24</sup> Haddon, R. C. Chemistry of the Fullerenes: the Manifestation of Strain in a Class of

- 
- Continuous Aromatic Molecules. *Science*, **1993**, *261*, 1545-1548.
- <sup>25</sup> Taylor, R. Surprise, Serendipity and Symmetry in Fullerene Chemistry. *Synlett.*, **2000**, 776-793.
- <sup>26</sup> Diederich, F.; Thilgen, C. Covalent Fullerene Chemistry. *Science*, **1996**, *271*, 317-323.
- <sup>27</sup> Zhu, Q.; Cox, D. E.; Fischer, J. E.; Kniaz, K.; McGhie, A. R.; Zhou, O.. Intercalation of Solid C<sub>60</sub> with Iodine. *Nature*, **1992**, *355*, 712-714.
- <sup>28</sup> Henderson, C. C.; Cahill, P. A. Synthesis, Isolation and Equilibration of 1,9- and 7,8-C<sub>70</sub>H<sub>2</sub>. *Science*, **1993**, *259*, 1885-1888.
- <sup>29</sup> Burgi, H. B.; Blanc, E.; Schwarzenbach, D.; Liu, S.; Lu, Y.; Kappes, M. M.; Ibers, J. The Structure of C<sub>60</sub>: Oritational Disorder in the Low-temperature Modification of C<sub>60</sub>. *Angew. Chem. Int. Ed. Engl.* **1992**, *31*, 640-642.
- <sup>30</sup> Akasaka, T.; Kato, T.; Kobayashi, K.; Nagase, S.; Yamamoto, K.; Funasaka, H.; Takahashi, T. Exohedral Adducts of La@C<sub>82</sub>. *Nature*, **1995**, *374*, 600-601.
- <sup>31</sup> Iezzi, E. B.; Duchamp, J. C.; Harich, K.; Glass, T. E.; Lee, H. M.; Olmstead, M. M.; Balch, A. L.; Dorn, H. C. A Symmetric Derivative of the Trimetallic Nitride Endohedral metallofullerene, Sc<sub>3</sub>N@C<sub>80</sub>. *J. Am. Chem. Soc.* **2002**, *124*, 524-525.
- <sup>32</sup> Stevenson, S.; Stephen, R. R.; Amos, T. M.; Cadorette, V. R.; Reid, J. E.; Philips, J. P. Synthesis and Purification of a Metallic Nitride Fullerene BisAdduct: Exploring the Reactivity of Gd<sub>3</sub>N@C<sub>80</sub>. *J. Am. Chem. Soc.* **2005**, *127*, 12776-12777.
- <sup>33</sup> Kato, H.; Suenaga, K.; Mikawa, M.; Okumura, M.; Miwa, N.; Yashiro, A.; Fujimura, H.; Mizuno, A.; Nishihiro, Y.; Kobayashi, K.; Shinohara, H. Syntheses and EELS Characterization of Water-soluble Multi-hydroxyl Gd@C<sub>82</sub> Fullerenols. *Chem. Phys. Lett.* **2000**, *324*, 255-259.
- <sup>34</sup> Sun, D.; Huang, H.; Yang, S. Synthesis and Characterization of a Water-soluble Endohedral Metallofullerol. *Chem. Mater.* **1999**, *11*, 1003-1006.
- <sup>35</sup> Iezzi, E. B.; Cromer, F.; Stevenson, P.; Dorn, H. C. Synthesis of the First Water-soluble Trimetallic Nitride Endohedral Metallofullerenols. *Synth. Met.* **2002**, *128*, 289-291.
- <sup>36</sup> Maggini, M.; Scorrano, G.; Prato, M. Addition of Azomethine Ylides to C<sub>60</sub>: Synthesis, Characterization, and Functionalization of Fullerene Pyrrolidines. *J. Am. Chem. Soc.* **1993**, *115*, 9798-9799.
- <sup>37</sup> Cai, T.; Ge, Z.; Iezzi, E. B.; Glass, T. E.; Harich, K.; Gibson, H. W.; Dorn, H. C. Synthesis and Characterization of the First Trimetallic Nitride Templated Pyrrolidino Endohedral Metallofullerenes. *Chem. Commun.* **2005**, *28*, 3594-3596.

- 
- <sup>38</sup> Cardona, C. M.; Kitaygorodskiy, A.; Ortiz, A.; Herranz, M. A.; Echogoyen, L. The First Fulleopyrrolidine Derivative of Sc<sub>3</sub>N@C<sub>80</sub>: Pronounced Chemical Shift Differences of the Geminal Protons on the Pyrrolidine Ring. *J. Org. Chem.* **2005**, *70*, 5092-5097.
- <sup>39</sup> Hirsch, A. Addition Reaction of Buckminsterene. *Synthesis*, **1995**, 895-904.
- <sup>40</sup> Cardona, C. M.; Kitaygorodskiy, A.; Echegoyen, L. Trimetallic Nitride Endohedral Metallofullerenes: Reactivity Dictated by the Encapsulated Metal Cluster. *J. Am. Chem. Soc.* **2005**, *127*, 10448-10553.
- <sup>41</sup> Iezzi, E. B. Exohedral Functionalization and Applications of the Trimetallic Nitride Endohedral Metallofullerenes. Dissertation of Virginia Polytechnic Institute and State University, **2003**, Blacksburg, VA.
- <sup>42</sup> Ostwald, W. *Handbush der allgemeine Chemie. B. I.* page 70, Academische Verlagsgsellschaft, Leipzig, **1919**.
- <sup>43</sup> Komatsu, K.; Muruta, Y.; Wang, G. W.; Tanaka, T.; Kato, N.; Fujiwara, K. The Solid-state Mechanochemical Reaction of Fullerene C<sub>60</sub>. *Fullerene Sci. Techn.*, **1999**, *7*(4), 609-620.
- <sup>44</sup> Rowlands, S. A.; Hall, A. K.; McCormick, P. G.; Street, R.; Hart, R. J.; Ebell, G. F.; Donecker, P. Destruction of Toxic Materials. *Nature*, **1994**, *367*, 223-226.
- <sup>45</sup> Field, L. D.; Sternbell, S.; Wilton, H. V. Mechanochemistry of Some Hydrocarbons, *Tetrahedron*, **1997**, *53*, 4051-4062.
- <sup>46</sup> Field, L. D.; Sternbell, S.; Wilton, H. V. Mechanohydrogenation. *Tetrahedron Lett.* **1998**, *39*, 115-117.
- <sup>47</sup> Fernandez-Bertran, J.; Castellanos-Serra, L.; Yee-Medeira, H.; Reguera, E. Proton Transfer in Solid State: Mechanochemical Reactions of Imidazole with Metallic Oxides. *J. Solid State Chem.* **1999**, *147*, 561-565.
- <sup>48</sup> Makhaev, V. D.; Borisov, A. P.; Petrova, L. A. Solid-State Mechanochemical Synthesis of Ferrocene. *J. Organomet. Chem.* **1999**, *590*, 222-226.
- <sup>49</sup> Balema, V. P.; Wiench, J. W.; Pruski, M.; Pecharsky, V. K. Solvent-free Mechanochemical Synthesis of Phosphonium Salts. *Chem. Commun.* **2002**, *7*, 724-725.
- <sup>50</sup> Komatsu, K.; Wang, G. W.; Murata, Y.; Tanaka, T.; Fujiwara, K.; Yamamoto, K.; Sauders, M. Mechanochemical Synthesis and Characterization of the Fullerene Dimer C<sub>120</sub>. *J. Org. Chem.* **1998**, *63*, 9358-9366.
- <sup>51</sup> Wang, G. W. Fullerene Mechanochemistry. *Encyclopedia of Nanoscience and Nanotechnology.* **2003**, Vol. 3, 557-565.
- <sup>52</sup> Toda, F. Solid State Organic Chemistry: Efficient Reactions, Remarkable Yields and

- 
- Stereoselectivity. *Acc. Chem. Res.* **1995**, *28*, 480-486.
- <sup>53</sup> Tanaka, K.; Toda, F. Solvent-free Organic Synthesis. *Chem. Rev.* **2000**, *100*, 1025-1074.
- <sup>54</sup> Dachille, F.; Roy, R. High-pressure Phase Transformation in Laboratory Mechanical Mixers and Mortars. *Nature*, **1960**, *186*, 34-35.
- <sup>55</sup> Wang, G. W.; Muruta, Y.; Komatsu, K.; Wan, T. S. M. The Solid-phase Reaction of [60] Fullerene: Novel Addition of Organozine Reagents. *Chem. Commun.* **1996**, 2059-2060.
- <sup>56</sup> Pekker, S.; Janossy, A.; Mihaly, L.; Chauvet, O.; Carrard, M.; Ferro, L. Single-Crystalline (KC<sub>60</sub>)<sub>n</sub>: a Conducting Linear Alkali Fulleride polymer. *Science*, **1994**, *265*, 1077-1079.
- <sup>57</sup> Persson, P. A.; Edlund, U.; Jacobsson, P.; Hohnels, D.; Soldatov, A.; Sundqvist, B. NMR and Raman Characterization of Pressure Polymerized C<sub>60</sub>. *Chem. Phys. Lett.* **1996**, *258*, 540-543.
- <sup>58</sup> Keshavarz, M.; Knight, K. B.; Srdanov, G.; Wudl, F. Cyanodihydrofullerenes and Dicyanodihydrofullerene: the First Polar Solid Based on C<sub>60</sub>. *J. Am. Chem. Soc.* **1995**, *117*, 11371-11372.
- <sup>59</sup> Wang, G. W.; Komatsu, K.; Muruta, Y.; Shiro, M. Synthesis and X-ray Structure of Dumb-bell-shaped C<sub>120</sub>. *Nature*, **1997**, *387*, 583-585.
- <sup>60</sup> Komatsu, K.; Fujiwara, K.; Murata, Y. The Fullerene Cross-dimer C<sub>130</sub>: Synthesis and Properties. *Chem. Commun.* **2000**, 1583-1584.
- <sup>61</sup> Tagmatarchis, N.; Forman, C. S.; Taninaka, A.; Shinohara, H. Cross-fullerene Dimers [(C<sub>60</sub>)(C<sub>70</sub>)]: Solid-state Synthesis, Characterization and Mechanism. *Synlett*, **2002**, 235-238.
- <sup>62</sup> Forman, G. S.; Tagmatarchis, N. N.; Shinohara, H. Novel Synthesis and Characterization of Five Isomers of (C<sub>70</sub>)<sub>2</sub> Fullerene Dimers. *J. Am. Chem. Soc.* **2002**, *124*, 178-179.
- <sup>63</sup> Kunitake, M.; Uemura, S.; Ito, O.; Fujiwara, K.; Murata, Y.; Komatsu, K. Structural Analysis of C<sub>60</sub> Trimers by Direct Observation with Scanning Tunneling Microscopy. *Angew. Chem. Int. Ed. Engl.* **2002**, *41*, 969-972.
- <sup>64</sup> Schlueter, J. A.; Seaman, J. M.; Taha, S.; Cohen, H.; Lykke, K. R.; Wang, H. H.; Williams, J. M. Synthesis, Purification and Characterization of the 1:1 Addition Product of C<sub>60</sub> and Anthracene. *J. Chem. Soc. Chem. Commun.* **1993**, 972-973.
- <sup>65</sup> Tsuda, M.; Ishida, T.; Nogami, T.; Kurono, S.; Ohashi, M. Isolation and Characterization of Diels-Alder Adducts of C<sub>60</sub> with Anthracene and Cyclopentadiene. *J. Chem. Soc. Chem. Commun.* **1993**, 1296-1297.
- <sup>66</sup> Murata, Y.; Kato, N.; Fujiwara, K.; Komatsu, K. Solid-state [4+2] Cycloaddition of Fullerene C<sub>60</sub> With Condensed Aromatics Using a High-speed Vibration Milling Technique. *J. Org. Chem.* **1999**, *64*, 3483-3488.

- 
- <sup>67</sup> Mack, J.; Miller, G. P. Synthesis and Characterization of a C<sub>60</sub>-pentacene Monoadduct. *Fullerene Sci. Techn.* **1997**, *5*, 607-613.
- <sup>68</sup> Murata, Y.; Kato, N.; Komatsu, K. The Reaction of Fullerene C<sub>60</sub> with Phthalazine: the Mechanochemical Solid-state Reaction Yielding a New C<sub>60</sub> dimer versus the Liquid-phase Reaction Affording an Open-cage Fullerene. *J. Org. Chem.* **2001**, *66*, 7235-7239.
- <sup>69</sup> Grosser, T.; Prato, M.; Lucchini, V.; Hirsch, A.; Wudl, F. Ring Expansion of Fullerene Core by Highly Regioselective Formation of Diazafulleroids. *Angew. Chem. Int. Ed. Engl.* **1995**, *34*, 1343-1345.
- <sup>70</sup> Wang, G. W.; Zhang, T. H.; Hao, E. H.; Jiao, L. J.; Murata, Y.; Komatsu, K. Solvent-free Reactions of Fullerenes and N-alkylglycines With and Without Aldehydes Under High-speed Vibration Milling. *Tetrahedron*, **2003**, *59*, 55-60.
- <sup>71</sup> Taylor, R.; Walton, D. R. M. The Chemistry of Fullerenes. *Nature*, **1993**, *363*, 685-687.
- <sup>72</sup> Hirsch, A. The Chemistry of Fullerenes: an Overview. *Angew. Chem. Int. Ed. Engl.* **1993**, *32*, 1138-1141.
- <sup>73</sup> Tanaka, T.; Komatsu, K. Mechanochemical Acylation and Alkylation of Fullerene C<sub>60</sub> Under the Solvent-free Reaction. *Synth. Commun.* **1999**, *29*, 4397-4403.
- <sup>74</sup> Akasaka, T.; Ando, W.; Kobaya, K.; Nagase, S. Reaction of C<sub>60</sub> with Silylene: The First Fullerene Silirane Derivative. *J. Am. Chem. Soc.* **1993**, *115*, 1605-1606.
- <sup>75</sup> Akasaka, T.; Ando, W.; Kobaya, K.; Nagase, S. Organic Chemical Derivatization of Fullerenes: Photochemical [2+3] cycloaddition of C<sub>60</sub> with disiliranes. *J. Am. Chem. Soc.* **1993**, *115*, 10366-10367.
- <sup>76</sup> Kusukawa, T.; Ando, W. Reactions of Silyllithium with C<sub>60</sub>: Isolation and X-ray Crystallographic Characterization of an Unusual Bissilylated-C<sub>60</sub> Adduct. *Angew. Chem. Int. Ed. Engl.* **1996**, *35*, 1315-1317.
- <sup>77</sup> Fujiwara, K.; Komatsu, K. Mechanochemical Synthesis of a Novel C<sub>60</sub> Dimer Connected by a Silicon Bridge and a Single Bond. *Org. Lett.* **2002**, *4*, 1039-1041.
- <sup>78</sup> Cagle, D. W.; Kennel, S. J.; Mirzadeh, S.; Alford, J. M.; Wilson, L. J. *In vivo* Studies of Fullerene-based Materials Using Endohedral Metallofullerene Radiotracers. *Proc. Natl. Acad. Sci. U.S.A* **1999**, *96*, 5182-5187.
- <sup>79</sup> Thrash, T. P.; Cagle, D. W.; Alford, J. M.; Wright, K.; Ehrhardt, G. J.; Mirzadeh, S.; Wilson, L. J. Toward fullerene-based radiopharmaceuticals: high-yield neutron activation of endohedral <sup>165</sup>Ho metallofullerenes. *Chem. Phys. Lett.* **1999**, *308*, 329-336.
- <sup>80</sup> Cagle, D. W.; Alford, J. M.; Tien, J.; Wilson, L. J. Gadolinium-Containing Fullerenes for

- 
- MRI Contrast Agent Application. In *Fullerenes: Recent Advances in the Chemistry and Physics of Fullerenes and Related Materials*. Kadish, K.; Ruoff, R.; The Electrochemical Society, Inc.: Pennington, NJ, **1997**; Vol. 4, 361-368.
- <sup>81</sup> Mikawa, M.; Kato, H.; Okumura, M.; Narazaki, M.; Kanazawa, Y.; Miwa, N.; Shinohara, H. Paramagnetic Water-Soluble Metallofullerenes Having the Highest Relaxivity for MRI Contrast Agents. *Bionconjugate Chem.* **2001**, *12*, 510-514.
- <sup>82</sup> Kato, H.; Kanazawa, Y.; Okumura, M.; Taninaka, A.; Yokawa, T.; Shinohara, H. Lanthanoid Endohedral Metallofullerenols for MRI Contrast Agents. *J. Am. Chem. Soc.* **2003**, *125*, 4391-4397.
- <sup>83</sup> Bolskar, R. D.; Benedetto, A. F.; Husebo, L. O.; Price, R. E.; Jackson, E. F.; Wallace, S.; Wilson, L. J.; Alford, J. M. First Soluble M@C<sub>60</sub> Derivatives Provide Enhanced Access to Metallofullerenes and Permit in Vivo Evaluation of Gd@C<sub>60</sub>[C(COOH)<sub>2</sub>]<sub>10</sub> as a MRI Contrast Agents. *J. Am. Chem. Soc.* **2003**, *125*, 5471-5478.
- <sup>84</sup> Sitharaman, B.; Bolskar, R. D.; Rusakova, I.; Wilson, L. J. Gd@C<sub>60</sub>[C(COOH)<sub>2</sub>]<sub>10</sub> and Gd@C<sub>60</sub>(OH)<sub>x</sub>: Nanoscale Aggregation Studies of Two Metallofullerene MRI Contrast Agents in Aqueous Solution. *Nano Lett.* **2004**, *4*, 2373-2378.
- <sup>85</sup> Tóth, E.; Bolskar, R. D.; Borel, A.; Gonzalez, G.; Helm, L.; Merbach, A. E.; Sitharaman, B.; Wilson, L. J. Water-Soluble Gadofullerenes: Toward High-Relaxivity, pH-Responsive MRI Contrast Agents. *J. Am. Chem. Soc.* **2005**, *127*, 799-805.
- <sup>86</sup> Yu, S. B.; Watson, A. D. Metal-based X-ray Contrast Media. *Chem. Rev.* **1999**, *99*, 2353-2377.
- <sup>87</sup> Iezzi, E. B.; Duchamp, J.; Fletcher, K.; Glass, T.; Dorn, H. C. Lutetium-based Trimetallic Nitride Endohedral Metallofullerenes: New Contrast Agents. *Nano Lett.* **2002**, *2*, 1187-1190.
- <sup>88</sup> Arbogast, J. W.; Darmany, A. P.; Foote, C. S.; Rubin, Y.; Diederich, F. N.; Alvarez, M. M.; Anz, S. J.; Whetten, R. L. Photophysical Properties of C<sub>60</sub>. *J. Phys. Chem.* **1991**, *95*, 11-12.
- <sup>89</sup> Pailt, D. K.; Spare, A. V.; Mittal, J. P. Photophysical Properties of the Fullerenes, C<sub>60</sub> and C<sub>70</sub>. *Chem. Phys. Lett.* **1992**, *195*, 1-6.
- <sup>90</sup> Cheng, J. X.; Fang, Y.; Huang, Q. J.; Yan, Y. J.; Li, X. Y. Blue-green Photoluminescence From Pyridine-C<sub>60</sub> Adduct. *Chem. Phys. Lett.* **2000**, *330*, 262-266.
- <sup>91</sup> Zhao, Y.; Fang, Y. Fluorescence of C<sub>60</sub> and Its Interaction with Pyridine. *J. Phys. Chem. B* **2004**, *108*, 13586-13588.
- <sup>92</sup> Sun, D.; liu, Z.; Guo, X.; Liu, S. Synthesis and Spectroscopic Studies of Endohedral Metallofullerenes Tb@C<sub>2n</sub>. *Fullerene Sci. Techn.* **1998**, *6*, 707-713.

- 
- <sup>93</sup> Nath, S.; Pal, H.; Sapre, A. V.; Bubnov, V. P.; Estrin, Y. I.; Parnyuk, T. A.; Koltover, V. K. Aggregation of Endometallofullerene Y@C<sub>82</sub> in Polar Solvents. *Fullerene, Nanotubes, and Carbon Nanostructures*. **2004**, *12*, 53-57.
- <sup>94</sup> Shu, C. Y.; Gan, L. H.; Wang, C. R.; Pei, X.; Han, H. Synthesis and characterization of a new water-soluble endohedral metallofullerene for MRI contrast agents. *Carbon*, **2005**, *44*, 496-500.
- <sup>95</sup> Wharton, T.; Wilson, L. J. Highly-Iodinated Fullerene as a Contrast Agent For X-ray Imaging. *Biorg. Med. Chem.* **2002**, *10*, 3545-3554.
- <sup>96</sup> Fatouros, P. P.; Corwin, F. D.; Chen, Z.; Broaddus, W. C.; Tatum, J. L.; Ge, Z.; Gibson, H. W.; Russ, J. L.; Leonard, A. P.; Duchamp, J. C.; Dorn, H. C. *In Vitro* and *In Vivo* Imaging Studies of a New Gadolinium Endohedral Metallofullerene MRI Contrast Agent. *Radiology* **2006**, in press.
- <sup>97</sup> Stevenson, S.; Philips, J. P.; Reid, J. E.; Olmstead, M. M.; Rath, S. P.; Balch, A. L. Pyramidalization of Gd<sub>3</sub>N Inside a C<sub>80</sub> Cage: the Synthesis and Structure of Gd<sub>3</sub>N@C<sub>80</sub>. *Chem. Commun.* **2004**, 2814-2815.
- <sup>98</sup> Krause, M.; Dunsch, L. Gadolinium Nitride Gd<sub>3</sub>N in Carbon Cages: The Influence of Cluster Size and Bond Strength. *Angew. Chem. Int. Ed.. Engl.* **2005**, *44*, 1557-1560.
- <sup>99</sup> Dunsch, L.; Krause, M.; Noack, P.; Georgi, P. Endohedral Nitride Cluster Fullerenes: Formation and Spectroscopic Analysis of L<sub>3-x</sub>M<sub>x</sub>N@C<sub>2n</sub> (x = 0-3; n = 39,40). *J. Phys. Chem. Solids*. **2004**, *65*, 309-315.
- <sup>100</sup> Zhang, P.; Pan, H.; Liu, D.; Guo, Z. X.; Zhang, F.; Zhu, D. Effective Mechanochemical Synthesis of [60]Fullerols. *Synth. Commun.* **2003**, *33*, 2469-2474.
- <sup>101</sup> Lu, X.; Li, H.; Sun, B.; Shi, Z.; Gu, Z. Selective reduction and extraction of Gd@C<sub>82</sub> and Gd<sub>2</sub>@C<sub>80</sub> from soot and the chemical reaction of their anions. *Carbon*, **2005**, *43*, 1546-1549.
- <sup>102</sup> Kocher, D.C. *Radioactive Decay Data Tables*, Springfield, National Technical Information Service, DOE/TIC 11028 (**1981**).
- <sup>103</sup> Kato, H.; Suenaga, K.; Mikawa, M.; Okumura, M.; Miwa, N.; yashiro, A.; Fujimura, H.; Mizuno, A.; Nishida, Y.; Kobayashi, K.; Shinohara, H. Syntheses and EELS Characterization of Water-Soluble Multi-hydroxyl Gd@C<sub>82</sub> Fullerenols. *Chem. Phys. Lett.* **2000**, *324*, 255-259.
- <sup>104</sup> Zhang, S.; Sun, D.; Li, X.; Pei, F.; Liu, S. Synthesis and Solvent Enhanced Relaxation Property of Water-soluble Endohedral Metallofullerenols. *Fullerene Sci. Technol.* **1997**, *5*, 1635-1643.

- 
- <sup>105</sup> Wilson, L. J. Medical Application of Metallofullerenes. *Interface* **1999**, 8, 24-28.
- <sup>106</sup> Shinohara, H. Endohedral Metallofullerenes. *Rep. Prog. Phys.* **2000**, 63, 843-892.
- <sup>107</sup> Akasaka, T.; Nagase, S. Endofullerenes: *A New Family of Carbon Clusters*, Kluwer Academic Publishers: Dordrecht, **2002**.
- <sup>108</sup> Wilson, L. J.; Cagle, D. W.; Thrash, T. P.; Kennel, S. J.; Mirzadeh, S.; Alford, J. M.; Ehrhardt, G. J. Metallofullerene Drug Design. *Coord. Chem. Rec.* **1999**, 190-192, 199-207.
- <sup>109</sup> Sun, D.; Liu, Z.; Guo, X.; Xu, W.; Liu, S. Gas Phase Derivations of Endohedral Metallofullerenes by Ion-molecular Reactions. *Fullerene Sci. Technol.* **1997**, 5, 1461-1477.
- <sup>110</sup> Kuran, P.; Krause, M.; Bartl, A.; Dunsch, L. Preparation, Isolation and Characterization of Eu@C<sub>74</sub>: the First Isolated Europium Endohedral Fullerene. *Chem. Phys. Lett.* **1998**, 292, 580-586.
- <sup>111</sup> Lebedkin, S.; Renker, B.; Heid, R.; Schober, H.; Rietschel, H. A Spectroscopic Study of M@C<sub>82</sub> Metallofullerenes: Raman, Far-infrared and Neutron Scattering Results. *Appl. Phys. A* **1998**, 66, 273-280.
- <sup>112</sup> Ding, J. Q.; Yang, S. H. Isolation and Characterization of Pr@C<sub>82</sub> and Pr<sub>2</sub>@C<sub>80</sub>. *J. Am. Chem. Soc.* **1996**, 118, 11254-11257.
- <sup>113</sup> Gu, G.; Huang, H. J.; Yang, S. H.; Yu, P.; Fu, J. S.; Wong, G. K.; Wan, X. G.; Dong, J. M.; Du, Y. W. The Third-order Non-linear Optical Response of the Endohedral Metallofullerene Dy@C<sub>82</sub>. *Chem. Phys. Lett.* **1998**, 289, 167-173.
- <sup>114</sup> Hino, S.; Umishita, K.; Iwasaki, K.; Miyazaki, T.; Miyamae, T.; Kikuchi, K.; Achiba, Y. Photoelectron Spectra of Metallofullerenes, GdC<sub>82</sub> and La<sub>2</sub>C<sub>80</sub>: Electron Transfer From the Metal to the Cage. *Chem. Phys. Lett.* **1997**, 281, 115-122.
- <sup>115</sup> Grannan, S. M.; Birmingham, J. T.; Richards, P. L.; Bethune, D. S.; De Vries, M. S.; Van Loosdrecht, P. H. M.; Dorn, H. C.; Burbank, P.; Bailey, J.; Steveson, S. Far Infrared Transmittance of Sc<sub>2</sub>@C<sub>84</sub> and Er<sub>2</sub>@C<sub>82</sub>. *Chem. Phys. Lett.* **1997**, 264, 359-365.
- <sup>116</sup> Ding, X. Y.; Aldord, J. M.; Wright, J. C. Lanthanide Fluorescence from Er<sup>3+</sup> in Er<sub>2</sub>@C<sub>82</sub>. *Chem. Phys. Lett.* **1997**, 269, 72-78.
- <sup>117</sup> (a) Ding, J. Q.; Weng, L. T.; Yang, S. H. Electronic Structure of Ce@C<sub>82</sub>: an Experimental Study. *J. Phys. Chem.* **1996**, 100, 11120-11121. (b) Ding, J. Q.; Yang, S. H. Isolation and Characterization of Ce<sub>2</sub>@C<sub>80</sub>. *Angew. Chem., Int. Ed.* **1996**, 35, 2234-2235.
- <sup>118</sup> Okazaki, T.; Lian, Y.; Gu, Z.; Suenaga, K.; Shinohara, H. Isolation and Spectroscopic Characterization of Sm-containing Metallofullerenes. *Chem. Phys. Lett.* **2000**, 320, 435-440.
- <sup>119</sup> Huang, H.; Yang, S. H. Preparation and Characterization of the Endohedral

- 
- Metallofullerene Lu@C<sub>82</sub>. *J. Phys. Chem. Solids* **2000**, *61*, 1105-1110.
- <sup>120</sup> Nagase, S.; Kobayashi, K. Theoretical Study of the Lanthanide Fullerene CeC<sub>82</sub>: Comparison with ScC<sub>82</sub>, YC<sub>82</sub> and LaC<sub>82</sub>. *Chem. Phys. Lett.* **1994**, *228*, 106-110.
- <sup>121</sup> Inakuma, M.; Kato, H.; Taninaka, A.; Shinohara, H.; Enoki, T. Magnetic Anisotropy of Cerium Metallofullerenes. *J. Phys. Chem. B* **2003**, *107*, 6965-6973.
- <sup>122</sup> Dunsch, L.; Georgi, P.; Krause, M.; Wang, C. R. New Clusters in Endohedral Fullerenes: the Metalnitrides. *Synth. Met.* **2003**, *135-136*, 761-762.
- <sup>123</sup> Feng, L.; Xu, J. X.; Shi, Z. J.; He, X.R.; Gu, Z. N. Isolation and Characterization of the Endohedral Metallofullerene Tb<sub>3</sub>N@C<sub>80</sub>. *Chem. J. Chin. Univ.* **2002**, *23*, 996-998.
- <sup>124</sup> Yang, S. F.; Dunsch, L. A Large Family of Dysprosium-based Trimetallic Nitride Endohedral Fullerenes: Dy<sub>3</sub>N@C<sub>2n</sub> (2n = 39-44). *J. Phys. Chem. B* **2005**, *109*, 12320-12328.
- <sup>125</sup> Krause, M.; Wong, J.; Dunsch, L. Expanding the World of Endohedral Fullerenes- the Tm<sub>3</sub>N@C<sub>2n</sub> (2n = 39-43). *Chem. Eur. J.* **2005**, *11*, 706-711.
- <sup>126</sup> (a) Kobayashi, K.; Nagase, S.; Akasaka, T. Endohedral Dimetallofullerenes Sc<sub>2</sub>@C<sub>84</sub> and La<sub>2</sub>@C<sub>80</sub>: Are the Metal Atoms Still Inside the Fullerene Cages? *Chem. Phys. Lett.* **1996**, *261*, 502-506. (c) Kobayashi, K.; Sano, Y.; Nagase, S. Theoretical Study of Endohedral Metallofullerenes: Sc<sub>3-n</sub>La<sub>n</sub>N@C<sub>80</sub> (n = 0-3). *J. Comput. Chem.* **2001**, *22*, 1353-1358.
- <sup>127</sup> (a) Aihara, J. Kinetic Stability of Metallofullerenes as Predicted by the Bond Resonance Energy Model. *Phys. Chem. Chem. Phys.* **2001**, *3*, 1427-1431. (b) Aihara, J. Kinetic Stability of Carbon Cages in Non-classical Metallofullerenes. *Chem. Phys. Lett.* **2001**, *343*, 465-469. (c) Aihara, J. Many Reactive Fullerenes Tend to Form Stable Metallofullerenes. *J. Phys. Chem. A* **2002**, *106*, 11371-11374.
- <sup>128</sup> Olmstead, M. M.; de Bettencourt-Dias, A.; Duchamp, J. C.; Stevenson, S.; Dorn, H. C.; Balch, A. L. Isolation and Crystallographic Characterization of ErSc<sub>2</sub>N@C<sub>80</sub>: an Endohedral Fullerene Which Crystallizes with Remarkable Internal Order. *J. Am. Chem. Soc.* **2000**, *122*, 12220-12226.
- <sup>129</sup> Krause, M.; Dunsch, L. Isolation and Characterization of Two Sc<sub>3</sub>N@C<sub>80</sub> Isomers. *Chem. Phys. Chem.* **2004**, *5*, 1445-1449.
- <sup>130</sup> Yang, S.; Dunsch, L. Expanding the Number of Stable isomeric Structures of the C<sub>80</sub> Cage: a New Fullerene Dy<sub>3</sub>N@C<sub>80</sub>. *Chem. Eur. J.* **2005**, *12*, 413-419.
- <sup>131</sup> Enghag, P. *Encyclopedia of the Elements: Technical data, History, Processing, Applications*, Wiley-VCH, Weinheim, **2004**, pp386, 418.
- <sup>132</sup> Suzuki, S.; Ishii, T.; Sagawa, T. XPS and Photoabsorption Study of 4d Electrons in

- 
- Lanthanum and Cerium Halides. *Physica Fennica* **1974**, *9*, 310-312.
- <sup>133</sup> Yamada, M.; Nakahodo, T.; Wakahara, T.; Tsuchiya, T.; Maeda, Y.; Akasaka, T.; Kako, M.; Yoza, K.; Horn, E.; Mizorogi, N.; Kobayashi, K.; Nagase, S. Position Control of Encapsulated Atoms Inside a Fullerene Cage by Exohedral Addition. *J. Am. Chem. Soc.* **2005**, *127*, 14570-14571.
- <sup>134</sup> Miyake, Y.; Suzuki, S.; Kojima, Y.; Kikuchi, K.; Kobayashi, K.; Maniwa, Y.; Fischer, K. Motion of Scandium Ions in Sc<sub>2</sub>C<sub>84</sub> observed by <sup>45</sup>Sc Solution NMR. *J. Phys. Chem.* **1996**, *100*, 9579-9581.
- <sup>135</sup> Bleaney, B. Nuclear Magnetic Resonance Shifts in Solution Due to Lanthanide Ions. *J. Magn. Reson.* **1972**, *8*, 91-100.
- <sup>136</sup> Yamada, M.; Wakahara, T.; Lian, Y.; Tsuchiya, T.; Akasaka, T.; Waelchli, M.; Mizorogi, M.; Nagase, S.; Kadish, K. M. Analysis of Lanthanide-Induced NMR Shifts of the Ce@C<sub>82</sub> Anion. *J. Am. Chem. Soc.*, **2006**, *128*, 1400-1401.
- <sup>137</sup> Haddon, R. C.; Raghavachari, K. In *Buckminsterfullerenes*; Billups, W. E.; Ciufolini, M. A. Eds. VCH: New York, **1993**; Chapter 7.
- <sup>138</sup> Reich, A.; Panthofer, M.; Modrow, H.; Wedig, U.; Jansen, M. The Structure of Ba@C<sub>74</sub>. *J. Am. Chem. Soc.* **2004**, *126*, 14428-14434.
- <sup>139</sup> Olmstead, M. M.; Lee, H. M.; Duchamp, J. C.; Stevenson, S.; Marciu, D.; Dorn, H. C.; Balch, A. L. Sc<sub>3</sub>N@C<sub>68</sub>: Folded Pentalene Coordination in an Endohedral Metallofullerene that Does Not Obey the Isolated Pentagon Rule. *Angew. Chem. Int. Ed.* **2003**, *42*, 900-903.
- <sup>140</sup> Stevenson, S.; Lee, H. M.; Olmstead, M. M.; Kozikowski, C.; Stevenson, P.; Balch, A. L. Preparation and Crystallographic Characterization of a New Endohedral, Lu<sub>3</sub>N@C<sub>80</sub>•5(o-xylene) and Comparison with Sc<sub>3</sub>N@C<sub>80</sub>•5(o-xylene). *Chem. Eur. J.* **2002**, *8*, 4528-4535.
- <sup>141</sup> Heiney, P. A.; Fischer, J. E.; McGhie, A. B.; Romanow, W. J.; Denenstein, A. M.; McCauley Jr, J. P.; Smith III, A. B.; Cox, D. E. Orientational Ordering Transition in Solid C<sub>60</sub>. *Phys. Rev. Lett.* **1991**, *66*, 2911-2914.
- <sup>142</sup> Tycko, R.; Dabbagh, G.; Fleming, R. M.; Haddon, R. C.; Makhija, A. V.; Zahurak, S. M. Molecular Dynamics and the Phase Transition in Solid C<sub>60</sub>. *Phys. Rev. Lett.* **1991**, *67*, 1886-1889.
- <sup>143</sup> Isotov, D. E.; Tarasov, V. P.; Privalov, V. I.; Skokan, E. V.; Arkhangel'skii, T. V.; Velikodnyi, Yu. A.; Sidorov, L. N. Multiaxial Reorientation of C<sub>60</sub> and Phase Transition in Fullerite: Theory and NMR Experiment. *Proceedings-Electrochemical Society*, **1999**, 99-12 (Recent

- 
- Advances in the Chemistry and Physics of Fullerenes and Related Materials), 653-664.
- <sup>144</sup> Yannoni, C. S.; Johnson, R. D.; Meijer, G.; Bethune, D. S.; Salem, J. R. Carbon-13 NMR Study of the C<sub>60</sub> Cluster in the Solid State: Molecular Motion and Carbon Chemical Shift Anisotropy. *J. Phys. Chem.*, **1991**, *95*, 9-10.
- <sup>145</sup> Wang, X.; Xue, Q.; Hashizume, T.; Shinohara, H.; Nishina, Y.; Sakurai, T. Scanning-tunneling Microscopy Study of the Solid-Phase Pure Sc<sub>2</sub>C<sub>84</sub> Metallofullerene. *Phys. Rev. B* **1993**, *48*, 15492-15495.
- <sup>146</sup> Beyers, R.; Kiang, C.; Johnson, R. D.; Salem, J. R.; de Vires, M. S.; Yannoni, C. S.; Bethune, D. S. Dorn, H. C., Burbank, P. Preparation and Structure of Crystals of the Metallofullerene Sc<sub>2</sub>@C<sub>84</sub>. *Nature*, **1994**, *370*, 196-199.
- <sup>147</sup> Suematsu, H.; Murakami, Y.; Kawata, H.; Fujii, Y.; Hamaya, N.; Shimomura, O.; Kikuchi, K.; Achiba, Y.; Ikemoto, I. Crystal Structure of Endohedral Metallofullerene La@C<sub>82</sub>. *Mater. Res. Soc. Symp. Proc.* **1994**, *349*, 213-220.
- <sup>148</sup> Takata, M.; Umeda, B.; Nishibori, E.; Sakata, M.; Saito, Y.; Ohno, M.; Shinohara, H. Confirmation by X-ray Diffraction of the Endohedral Nature of the Metallofullerene Y@C<sub>82</sub>. *Nature*, **1995**, *377*, 46-49.
- <sup>149</sup> Kato, T.; Bandow, S.; Inakuma, M.; Shinohara, H. ESR Study on Structures and Dynamics of Sc<sub>3</sub>@C<sub>82</sub>. *J. Phys. Chem.* **1995**, *99*, 856-858.
- <sup>150</sup> Gorny, K. R.; Pennington, C. H.; Martindale, J. A.; Philips, J. P.; Stevenson, S.; Heinmaa, I.; Stern, R. Molecular Orientational Dynamics of the Endohedral Fullerene Sc<sub>3</sub>N@C<sub>80</sub> as Probed by <sup>13</sup>C and <sup>45</sup>Sc NMR. Los Alamos National Lab Preprint Archive, *Condensed Matter*, **2006**, 1-6, arXiv: cond-mat/0604365
- <sup>151</sup> Boere, R. T.; Kidd, R. G. Rotational Correlation Times in Nuclear Magnetic Relaxation. *Annu. Rep. NMR Spectrosc.* **1982**, *13*, 319-385.
- <sup>152</sup> Hubbard, P. S. Nonexponential Nuclear Magnetic Relaxation by Quadrupole Interactions. *J. Chem. Phys.* **1970**, *53*, 985-987.
- <sup>153</sup> Werbelow, L. G. NMR Dynamic Frequency Shifts and the Quadrupolar Interaction. *J. Chem. Phys.* **1979**, *70*, 5381-5383.
- <sup>154</sup> Aramini, J. M.; Vogel, H. A Scandium-45 NMR Study of Ovotransferrin and Its Half-Molecules *J. Am. Chem. Soc.* **1994**, *116*, 1988-1993.
- <sup>155</sup> Germann, M. W.; Aramini, J. M.; Vogel, H. J. Quadrupolar Metal Ion NMR Study of Ovotransferrin at 17.6 T. *J. Am. Chem. Soc.* **1994**, *116*, 6971-6972.

---

## VITA

Xuele Wang was born one of three children on May 27, 1983 in Shishou, China and raised as the son of a construction worker and housewife. He graduated with honors from Shishou No 1 High School in Shishou in July 1999, and then attended Fudan University in Shanghai, China during the fall of that same year. He obtained a Bachelor of Science degree in Chemistry in the summer of 2003. Upon graduation, he departed to Blacksburg to continue an education in Chemistry at Virginia Polytechnic Institute and State University (Virginia Tech), where he worked for Professor Harry C. Dorn in the field of Fullerene Chemistry. He received a M. S. degree in the summer of 2006.